BOUND STATES OF FERMIONS IN ONE DIMENSION

by

Binbin Tian

B.S., University of Science and Technology of China, 2012,

M.S., University of Pittsburgh, 2013

Submitted to the Graduate Faculty of

the Kenneth P. Dietrich School of Arts and Sciences in partial fulfillment

of the requirements for the degree of

Doctor of Philosophy

University of Pittsburgh

2019

UNIVERSITY OF PITTSBURGH

KENNETH P. DIETRICH SCHOOL OF ARTS AND SCIENCES

This dissertation was presented

by

Binbin Tian

It was defended on

September 23, 2019

and approved by

David Pekker, Department of Physics and Astronomy

Sergey Frolov, Department of Physics and Astronomy

Vincent Liu, Department of Physics and Astronomy

Daniel Boyanovsky, Department of Physics and Astronomy

Paul Leu, Department of Physics and Astronomy

Theodore Corcovilos, Department of Physics, Duquesne University

Dissertation Director: David Pekker, Department of Physics and Astronomy

BOUND STATES OF FERMIONS IN ONE DIMENSION

Binbin Tian, PhD

University of Pittsburgh, 2019

The formation of bound states of fermions in one dimension has always been one of the key topics in condensed matter physics. Motivated by recent experimental progresses in Prof. Jeremy Levy's group, we study the interplay of both species (spin and transverse band index) and mass imbalance in a mixture of two or more species of fermions with attractive interactions in one dimension. Previous theoretical and experimental efforts have shown the existence of a Fulde-Ferrell-Larkin-Ovchinnikov (FFLO) phase for the case of two species with equal mass, in addition to the fully paired and fully polarized phases. For the unequal mass case, there are signatures of trion phases as well. We use DMRG to explore the rich possibilities of quantum phases and their transport signatures for the cases of two and more species of Fermions as we vary the interaction strengths and mass imbalances. With this we can gain insights into ongoing experiments with sketched nanowires in LAO/STO and ultracold atoms confined to one-dimensional tubes.

We also study the formation of bound states in a single component Fermi chain with attractive interactions. The phase diagram, computed from DMRG (density matrix renormalization group), shows not only a superfluid of paired fermions (pair phase) and a liquid of fermion triplets (trion phase), but also a phase with two gapless modes. We show that the latter phase is described by a 2-component Tomonaga-Luttinger liquid (TLL) theory, consisting of one charged and one emergent neutral mode. We argue based on our numerical data, that the single, pair, and trion phases are descendants of the 2-component TLL theory. We speculate on the nature of the phase transitions amongst these phases.

TABLE OF CONTENTS

LIST OF TABLES

LIST OF FIGURES

LIST OF EQUATIONS

1.0 INTRODUCTION

This thesis is devoted to the numerical studies of the formation of bound states of fermions in one dimension. Motivated by recent experimental progresses made by Prof. Jeremy Levy's group, we first study the bound states of fermions composed of different species (band/spin). We construct a one dimesional minimal lattice model (Hubbard like) to simulate the LAO/STO nanowires and use numerical methods of Density Matrix Renormalization Group (DMRG) to obtain the ground state. By tuning the hopping parameters as well as the interactions strength between different species we are able to get qualitative agreement with the experimental data.

Tomonaga-Luttinger liquid (TLL) theory captures the physics of many 1-D quantum systems such as spin chains, spin ladders, nanotubes[3], nanowires[4], and cold atoms confined to 1-D tubes[5–9]. In higher dimensional systems, TLL is a tool that is often used, e.g. in edge theory[10] and coupled-wire constructions[11–13].

Recently, there has been significant interest in the study of 1D systems that cannot be described by the standard TLL theory[14–20]. In describing 1D interacting fermions, TLL theory naturally arises through bosonization that maps fermionic modes to bosonic modes. Nearby phases (i.e., descendants) such as charge density order appear as instabilities of the parent TLL theory[21–28].

The other key topic in this thesis in the bound states in single-component one-dimensional fermionic systems. We perform DMRG numerics on a lattice model with finite-range interactions, and find liquids of singles, pairs, trions, etc. in addition to an extended phase with two gapless modes (2M phase). We unify these findings by constructing an effective theory with an emergent mode that characterizes the 2M phase, the descendants of this theory describe the liquid phases of single fermions as well as multi-fermion bound states (of $2, 3, 4, \ldots$

fermions).

The rest of this thesis are organized as follows:

Chapter 2 gives an introduction of the DMRG method which is used throughout the thesis for numerical simulations. Specifically we first introduce the concept of Matrix Product State (MPS) and Matrix Product Operator (MPO) and their graphic notations. We show how to calculate the overlap between two MPS as well as how to apply an MPO onto an MPS. Then we discuss the details of DMRG algorithm, specifically how to "sweep" local sites to obtain the minimum energy state. Next, we discuss how to analyze the properties of the ground state, by measuring the ground state energy, entanglement entropy and various correlation functions. At the end of this chapter we provide a sample DMRG code and a sample output file as a guide to run the TenPy2 package, which we use in our numerical simulations.

Chapter 3 presents a brief overview of the Tomanaga-Luttinger liquid (TLL) theory. Specifically we discuss the peculiarity of one dimension and show how bosonization works. We also provide a short section on the spectral equivalence of boson and fermion in 1D. Next, we discuss the effects of interaction on TLL composed of spinless fermions. In the end we discuss the properties of various correlation functions in TLL.

Chapter 4 discuss the first main focus of this thesis. We begin this chapter by the experimental motivation and the model Hamiltonian we construct to simulate the LAO/STO nanwires. We aslo discuss the meaning of SU(N) symmetry of our model Hamiltonian. Next, we present some results in the low filling limit, which we obtain using finite lattice calculations. In this section we calculated the binding energies and masses of pairs and trions, showing that trions are quite stable. Next, we discuss the details of Jordan-Wigner transition and the numerical setup for our DMRG calculations. Afterwards, we separate our results into two parts: 2 species and 3 species. In each part we first discuss the expected phases and present the phase diagrams for different interactions. Next, we show the connections of our results with LAO/STO experiments. We discuss the validity of our model and perform transport calculations which is consistent with the experimental observation.

Chapter 5 discuss the other key result in this thesis. In this chapter we study the formation of bound states in single-component 1D fermionic systems. We first present the model Hamiltonian and the parameters we choose in the numerical calculations. We then discuss

numerical setup and how to run the DMRG code. Next, we present the numerical results, specifically the phase diagram and the Fourier spectra along two cuts of the phase diagram. To analyze the results we present a 2-mode theory where single mode phases are descents of the 2-mode theory. In section 5.6 we discuss in detail the match of numerical results with the predictions from the 2-mode theory. Afterwards we disucss the phase transitions in the phase diagram. In the end we provide numerical results of the quaternion phase, which serves as a general extension of our model. We also discuss how our results are beyond explanation of theories by previous studies.

Chapter 6 discuss a unique way to generate synthetic magnetic field for utracold atoms. We show the validaity of our proposal by analyzing the uniformness of the magnetic fields as well as the existence of the Landau levels in the system.

The works in this thesis have resulted in the following publications[29–32].

2.0 DENSITY MATRIX RENORMALIZATION GROUP (DMRG)

Most of the studies in this thesis are numerical simulations of one dimensional lattice systems. In this chapter we describe the standard algorithms of Density Matrix Renormalization Group (DMRG) we use for calculating the ground state proeprties of one dimensioanl lattice systems. The discussion in this chapter follows Ref.[33].

2.1 Introduction

Invented by Steve White in 1992[34], DMRG has been one of the most powerful numerical algorithms for calcuating the properties of one-dimensional quantum lattice systems, such as the Heisenberg and Hubbard models. Since its invention, the algorithms has been under constant development, expanding its application to more physical systems and higher dimensions[33].

Interestingly, the Matrix Product States (MPS) were discovered unrelated to DMRG as a class of quantum states for analytical studies. The most relavant prehistory is arguably given by the exact expression of the one-dimensional AKLT state in this form[23;35]. The connection between MPS and DMRG was made in two steps: the first step was made by Ostlund and Rommer[36] where they realized that the block growth step of the infinite-system DMRG can be expressed in MPS form. The second step was the recognition that finite-system DMRG leads to quantum states and MPS form, over which it varitionally optimizes[37]. It was not until 2004 that Cirac, Verstrate, Vidal and coworkers took the connections between DMRG and MPS seriously and explored the power of MPS systematically. MPS provides a convienet way to describe DMRG and opens the way to powerful extensions of DMRG.

We begin this chapter by first introducing the representation schemes we use for desribing quantum states – Matrix Product State (MPS). To do this we use graphic notations to provide a more clear picture of the procedures. We also discuss the convience of using canonical forms in our calculations. Then we present the details of how we achieve approximations by compressing the MPS representations.

Next, we discuss the Matrix Product Operators (MPO), specifically how we turn our Hamiltonian into MPO form. Then we present the standard procedures of applying MPO onto MPS.

Then we discuss the procedures we use throughout this thesis to get approximate MPS representation of the ground states of one dimensional lattice systems. We also present the details of obtaining entanglement entropy and correlation functions. Finally, We provide some sample code for our DMRG calculations.

2.2 Matrix Product State (MPS)

Consider a one-dimensional lattice of L sites, each site has local Hilbert space of dimension d described by σ_i ($i = 1 \dots L$). The dimension of the Hilbert space for the entire system is then given by d^L which grows exponentially with system size L. In general, any quantum state on the lattice can be written as: where $c_{\sigma_1 \dots \sigma_L}$ is a tensor of complex numbers with dimension

$$|\psi\rangle = \sum_{\sigma_1 \dots \sigma_L} c_{\sigma_1 \dots \sigma_L} |\sigma_1, \dots, \sigma_L\rangle, \tag{2.1}$$

d^L and $|\sigma_1, \dots, \sigma_L\rangle = |\sigma_1\rangle \otimes \cdots \otimes |\sigma_L\rangle$ is a product state. Based on the dimensionality we immediately see that the representations here is complete.

So far we have simply written down the most general form of any quantum state. Can we find a notation that gives a more local representation of the state? Indeed, by performing Singular Value Decomposition (SVD) we can achieve this.

In the first step we can reshape the coefficients $c_{\sigma_1 \ldots \sigma_L}$ into a matrix Ψ of dimensions $d \times d^{L-1}$: We can perform an SVD on Ψ: where U has orthonormal columns ($UU^\dagger = I$), $V^\dagger$

$$\Psi_{\sigma_1,(\sigma_2 \ldots \sigma_L)} = c_{\sigma_1 \ldots \sigma_L}. \tag{2.2}$$

$$c_{\sigma_1 \ldots \sigma_L} = \Psi_{\sigma_1,(\sigma_2 \ldots \sigma_L)} = \sum_{a_1}^{r_1} U_{\sigma_1,a_1} \left[S_{a_1,a_1} (V^\dagger)_{a_1,(\sigma_2 \ldots \sigma_L)} \right] = \sum_{a_1}^{r_1} U_{\sigma_1,a_1} c_{a_1 \sigma_2 \ldots \sigma_L}, \tag{2.3}$$

has orthonormal rows ($VV^\dagger = I$) and S is diagonal ($S_{aa} = s_a$) with singular values s_a. The number r of non-zero singular values is the Schmidt rank and we assume descending order such that $s_1 \geq s_2 \cdots \geq s_r$.

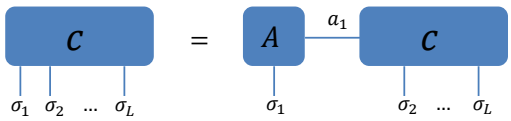

The above figure shows the gaphic notation of Eq. (2.3). For convience we define $A^{\sigma_1}_{a_1} = U_{\sigma_1,a_1}$ and we obtain $c_{\sigma_1 \ldots \sigma_L} = A^{\sigma_1}_{a_1} \Psi_{a_1,(\sigma_2 \ldots \sigma_L)}$. Here we have reshaped the coefficents into two blocks: one block on site 1 and the other block representing the rest of the lattice. These two blocks share the same index a_1 (that ranges from 1 to $r_1 \leq d$), shown in the figure as a connecting line between the two blocks.

We can repeat the same procedure for site 2: first we reshape $c_{\sigma_1 \ldots \sigma_L}$ into a matrix $\Psi_{(a_1 \sigma_2),(\sigma_3 \ldots \sigma_L)}$ of dimensions $(r_1 d \times d^{L-2})$ such that $c_{\sigma_1 \ldots \sigma_L} = A^{\sigma_1}_{a_1} \Psi_{(a_1 \sigma_2),(\sigma_3 \ldots \sigma_L)}$. Then we perform SVD on Ψ: where we use a set of a matrices A^{σ_2} of dimensions $r_1 \times r_2$ ($r_2 \leq d^2$) to represent U: $A^{\sigma_2}_{a_1,a_2} = U_{(a_1 \sigma_2),a_2}$. The graphic representation is shown below.

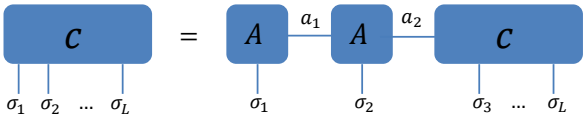

$$c_{\sigma_1 \ldots \sigma_L} = \sum_{a_1}^{r_1} \sum_{a_2}^{r_2} A_{a_1}^{\sigma_1} U_{(a_1 \sigma_2), a_2} \left[S_{a_2, a_2} (V^\dagger)_{a_2, (\sigma_3 \ldots \sigma_L)} \right] = \sum_{a_1}^{r_1} \sum_{a_2}^{r_2} A_{a_1}^{\sigma_1} A_{a_1, a_2}^{\sigma_2} \Psi_{(a_2, \sigma_3), (\sigma_4 \ldots \sigma_L)}, \quad (2.4)$$

We can continue the procedure and arrive at: More consicely we can write the quantum

$$c_{\sigma_1 \ldots \sigma_L} = \sum_{a_1, \ldots, a_{L-1}} A_{a_1}^{\sigma_1} A_{a_1, a_2}^{\sigma_2} \ldots A_{a_{L-2}, a_{L-1}}^{\sigma_{L-1}} A_{a_{L-1}}^{\sigma_L}. \quad (2.5)$$

state in the form of a matrix product state:

$$|\psi\rangle = \sum_{\sigma_1, \ldots, \sigma_L} A^{\sigma_1} \ldots A^{\sigma_L} |\sigma_1, \ldots, \sigma_L\rangle, \quad (2.6)$$

2.2.1 canonical form

Note here that because $UU^\dagger = I$ holds for every SVD, we can readily get Based on this

$$\sum_{\sigma_l} A^{\sigma_l \dagger} A^{\sigma_l} = I. \quad (2.7)$$

relation we define A is left-normalized, MPS that consists only of left-normalized matrices is *left canonical*.

In general we can split the lattice into parts A and B, where A is composed of sites 1 though l and B sites $l+1$ to L. We can introduce states as following: such that the MPS

$$|a_l\rangle_A = \sum_{\sigma_1,\ldots,\sigma_l} (A^{\sigma_1}\ldots A^{\sigma_l})|\sigma_1,\ldots,\sigma_l\rangle \tag{2.8}$$

$$|a_l\rangle_B = \sum_{\sigma_{l+1},\ldots,\sigma_L} (A^{\sigma_{l+1}}\ldots A^{\sigma_L})|\sigma_{l+1},\ldots,\sigma_L\rangle \tag{2.9}$$

can be written as

$$|\psi\rangle = \sum_{a_l} |a_l\rangle_A |a_l\rangle_B. \tag{2.10}$$

The forms we have obtained looks close to a Schmidt decomposition of $|\psi\rangle$, however it is not. For the Schmidt decomposition we need both $|a_l\rangle_A$ and $|a_l\rangle_B$ to form orthonormal basis. Because of the left-normality of A matrices, we immediately find that $|a_l\rangle_A$ form an orthonormal basis while $|a_l\rangle_B$ does not.

To deal with this we can instead start from the right (site L) and perfroming SVD to the left. By doing this we obtain the right-normalized matrices B such that where MPS

$$\sum_{\sigma_l} B^{\sigma_l} B^{\sigma_l\dagger} = I, \tag{2.11}$$

composed of purely B matrices are called *right-canonical*.

To achieve the Schmidt decomposition we need the mixed-caonical form of the MPS. Specifically we write: which contains the singular values on the bond $(l, l+1)$ and graphically represented below. By redefining $|a_l\rangle_B$ in terms of B matrices, we arrive at which is the Schmidt decomposition on site l.

$$c_{\sigma_1 \ldots \sigma_L} = A^{\sigma_1} \ldots A^{\sigma_l} S B^{\sigma_{l+1}} \ldots B^{\sigma_L}, \tag{2.12}$$

$$|\psi\rangle = \sum_{a_l} s_a |a_l\rangle_A |a_l\rangle_B, \tag{2.13}$$

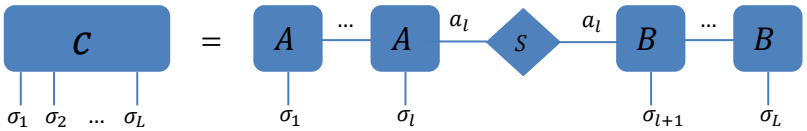

This form will be important in the DMRG algorithm when we optimize the elements of a particular tensor in order to find the variational ground state.

2.2.2 truncation

In the MPS representation we readily see that we have achieved a "local" representation: each site is descriped by a matrix with dimensions: $(1 \times d), (d \times d^2), \ldots, (d^{L/2-1} \times d^{L/2}), (d^{L/2} \times d^{L/2-1}), \ldots, (d \times 1)$. Here the dimensions of the matrix is still exponential with system size L, and we need to find a way to bound their size to some χ (bond dimension). Refer to the mixed canonical representation in Eq. (2.13), we can keep the χ largest singular values. By doing this we have reduced the computational complexity from $O(d^L)$ (exponential) to $O(L\chi^2)$ (linear), which greatly reduces the computational cost[1]. We can repeat the truncation $L-1$ times (at each bond) and it has been shown that the error is at worst: where $\epsilon_i(\chi) = \sum_{j>\chi} s_j^2$ is the truncation error (sum of the discarded squared singular values)

[1]We will describe the details of choosing χ in a later section of this chapter

$$||\psi\rangle - |\psi_{\text{trunc}}\rangle|^2 \leq 2\sum_{i=1}^{L-1}\epsilon_i(\chi), \tag{2.14}$$

at bond i. The accuracy of DMRG is then related to the singular value spectra of the reduced density operators. There is an area law which states that entanglement entropy grows as the area instead of volume[38] [2]. In one dimension this means entanglement entropy does not grow with system size and we can achieve a high precision ground state for systems with short-range interactions using DMRG.

2.2.3 overlap and efficient contraction of MPS

Having introduced the notation of MPS, we now discuss how to calculate the overlap of two MPS state $|\psi\rangle$ and $|\phi\rangle$, described by matrices M and $\tilde{M}$, respectively:

$$|\psi\rangle = M^{\sigma_1}\dots M^{\sigma_L}|\sigma_1\dots\sigma_L\rangle \tag{2.15}$$

$$|\phi\rangle = \tilde{M}^{\sigma_1}\dots \tilde{M}^{\sigma_L}|\sigma_1\dots\sigma_L\rangle \tag{2.16}$$

To calculate the overlap $\langle\phi|\psi\rangle$ we need to take the adjoint of $|\phi\rangle$: the pictorial representation is shown below.

In Eq. (2.17) we see that we need to perform contractions both over the matrix indices (implicit) and also over the physcial indices σ_i. If we were to contract the matrix indices first and then physical indices, we will need to perform over d^L times of matrix multiplication,

[2] the area law states predict that for ground states of short-ranged Hamiltonians with a gap to excitations entanglement entropy is not extensive, but proportional to the surface. For critical states (like TLL) entanglement grows logarithmically with system size. This allows us to make progress by studying finite size scaling as we describe later.

$$\langle\phi|\psi\rangle = \sum_{\sigma_1,\ldots,\sigma_L} \tilde{M}^{\sigma_1\dagger}\ldots\tilde{M}^{\sigma_L\dagger}M^{\sigma_1}\ldots M^{\sigma_L}, \tag{2.17}$$

which is exponentially with system size L[3].

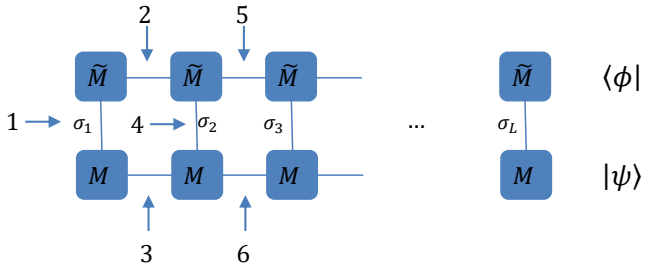

Figure 1: Schematic picture of contraction between two MPS. The number with arrows denotes the order of the contraction.

However, we can get around with this by regrouping the sum as: Here in the first step

$$\langle\phi|\psi\rangle = \sum_{\sigma_L} \tilde{M}^{\sigma_L\dagger}\left(\ldots\left(\sum_{\sigma_2}\tilde{M}^{\sigma_2\dagger}\left(\sum_{\sigma_1}\tilde{M}^{\sigma_1\dagger}M^{\sigma_1}\right)M^{\sigma_2}\right)\ldots\right)M^{\sigma_L}. \tag{2.18}$$

we multiply $\tilde{M}^{\sigma_1\dagger}$ and M^{σ_1} to form a matrix and sum over the first physical index σ_1. Then we perform a three-matrix multiplication over the second physical index (shown in Fig. 1 as step 2 and 3). The individual complexity of the matrix multiplication is $O(\chi^3)$ and we need in total $O(L\chi^3 d)$ complexity, which is a lot better than the exponential cost if we perfrom the contraction of matrix indices and then physical indices.

[3]each spin combination requires a separate matrix multiplication

2.3 Matrix Product Operators

Having introduced the concept of MPS, a natural extension lead to the definition of Matrix Product Operator (MPO) such that the coefficients $\langle\sigma|\hat{O}|\sigma\rangle$ are given by where $W^{\sigma\sigma'}$ are

$$\langle\sigma|\hat{O}|\sigma\rangle = W^{\sigma_1\sigma_1'}\dots W^{\sigma_L\sigma_L'}, \tag{2.19}$$

matrices just like the M matrices we have encountered before, except that now we have two physical indices sticking out instead of one. The graphical representation is shown below.

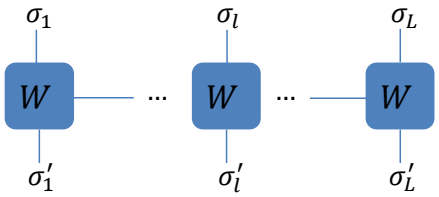

As shown in the figure above, the matrix representation of an operator $\hat{O}$ is given by:

$$\hat{O} = \sum_{\sigma,\sigma'} W^{\sigma_1\sigma_1'}\dots W^{\sigma_L\sigma_L'}|\sigma\rangle\langle\sigma'|. \tag{2.20}$$

In principle, any operators can be written in the form of MPO: where we have reshaped

$$\begin{aligned}\hat{O} &= \sum_{\sigma_1,\dots,\sigma_L;\sigma_1',\dots,\sigma_L'} c_{(\sigma_1\dots\sigma_L),(\sigma_1'\dots\sigma_L')}|\sigma_1,\dots,\sigma_L\rangle\langle\sigma_1',\dots,\sigma_L'| \\ &= \sum_{\sigma_1,\dots,\sigma_L;\sigma_1',\dots,\sigma_L'} c_{(\sigma_1\sigma_1')\dots(\sigma_L\sigma_L')}|\sigma_1,\dots,\sigma_L\rangle\langle\sigma_1',\dots,\sigma_L'|\end{aligned} \tag{2.21}$$

the form of c and we can decompose further as we did with MPS and obtain the form of an MPO.

2.3.1 applying an MPO to an MPS

The application of an MPO (Eq.(2.20)) to an MPS (Eq.(2.6)) runs as: The graphical repre-

$$
\begin{aligned}
\hat{O}|\psi\rangle &= \sum_{\sigma,\sigma'} \Big(W^{\sigma_1,\sigma_1'}(W^{\sigma_2,\sigma_2'}\dots\Big)\Big(M^{\sigma_1'}M_2^{\sigma'}\dots\Big)|\sigma_1,\dots,\sigma_L\rangle \\
&= \sum_{\sigma,\sigma'}\sum_{a,b}\Big(W_{1,b_1}^{\sigma_1,\sigma_1'}W_{b_1,b2}^{\sigma_2,\sigma_2'}\dots\Big)\Big(M_{1,a_1}^{\sigma_1'}M_{a_1,a_2}^{\sigma_2'}\dots\Big)|\sigma\rangle \\
&= \sum_{sigma,\sigma'}\sum_{a,b}\Big(W_{1,b_1}^{\sigma_1,\sigma_1'}M_{1,a_1}^{\sigma_1'}\Big)\Big(W_{b1_b2}^{\sigma_2,\sigma_2'}M_{a_1,a_2}^{\sigma_2'}\Big)\dots|\sigma\rangle \\
&= \sum_{\sigma}\sum_{a,b}N_{(1,1),(b_1,a_1)}^{\sigma_1}N_{(b_1,a_1),(b_2,a_2)}^{\sigma_2}\dots|\sigma\rangle \\
&= \sum_{\sigma}N^{\sigma_1}N^{\sigma_2}\dots|\sigma\rangle
\end{aligned}
\tag{2.22}
$$

sentation is shown below:

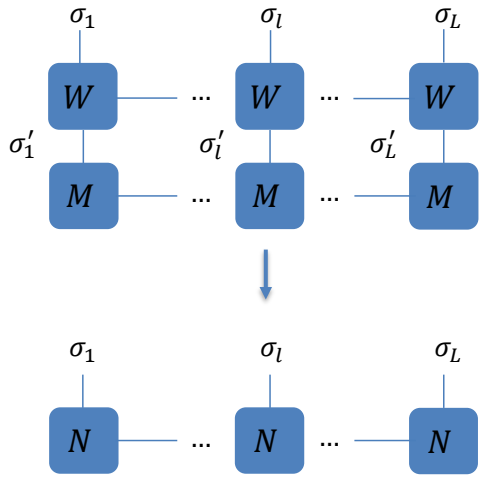

We see that applying an MPO to an MPS results a new MPS. The result above can be

summarized as $|\phi\rangle = \hat{O}|\psi\rangle$ where $|\phi\rangle$ is an MPS with matrices N^{σ_i}:

$$N^{\sigma_i}_{(b_{i-1},a_{i-1}),(b_i,a_i)} = \sum_{\sigma_i'} W^{\sigma_i\sigma_i'}_{b_{i-1}b_i} M^{\sigma_i'}_{a_{i-1}a_i}. \tag{2.23}$$

Using the formula above, the operational complexity is of order $Ld^2\chi_W^2\chi^2$, where χ_W is the bond dimension of the MPO.

2.3.2 MPO representation of Hamiltonian

For our numerical calculations, we build MPO from the Hamiltonian and apply variational approach to calculate the ground state. To build an MPO, we need a localized description of the operators in the Hamiltonian. From the graphical representation of an MPO shown above, we see that an MPO generally takes the form of 4-tensor (except the left- and right-most tensors).

For onsite (one-body) terms the 4-tensors can be written as: where multiplying W_i would

$$W_i^{\sigma_i,\sigma_i'(1)} = \begin{pmatrix} I^{\sigma_i,\sigma_i'} & 0 \\ X_i^{\sigma_i,\sigma_i'} & I^{\sigma_i,\sigma_i'} \end{pmatrix} \tag{2.24}$$

give the sum of onsite terms $X_1 + X_2 + X_3 + \ldots$.

For two-body terms the 4-tensors can be written as: where multiplying W_i would give the term X_iY_{i+1}. All matrices in the above has local dimensions $d \times d$. Generally a Hamiltonian contains both the one-body and two-body terms, and we can combine the above equations into: which gives terms $X_i + Y_iZ_{i+1}$.

As discussed before, the left- and right-most sites have different dimensions and we can write their MPO as: The complete Hamiltonian can then be constructed by multiplying

$$W_i^{(2)} = \begin{pmatrix} I & 0 & 0 \\ Y_i & 0 & 0 \\ 0 & X_i & I \end{pmatrix} \tag{2.25}$$

$$W_i^{(1,2)} = \begin{pmatrix} I & 0 & 0 \\ Z_i & 0 & 0 \\ X_i & Y_i & I \end{pmatrix} \tag{2.26}$$

$$W_1 = \begin{pmatrix} X_1 & Y_1 & I \end{pmatrix}, W_L = \begin{pmatrix} X_1 \\ Y_1 \\ I \end{pmatrix} \tag{2.27}$$

these W_i tensors.

Generally, we can achieve longer-ranged Hamiltonian by increasing the matrix size. As an example, a model with nearest and next-nearest neighbours such as: can be constructed

$$H = J_1 \sum_i S_i^z S_{i+1}^z + J_2 \sum_i S_i^z S_{i+2}^z \tag{2.28}$$

by the following MPO:

$$W_i = \begin{pmatrix} I & 0 & 0 & 0 \\ S^z & 0 & 0 & 0 \\ 0 & I & 0 & 0 \\ 0 & J_1 S^z & J_2 S^z & I \end{pmatrix} \tag{2.29}$$

2.4 Ground state calculation with MPS

DMRG is a variational optimization scheme and its goal is to minimize the energy of state $|\psi\rangle$ with respect to Hamiltonian:

$$E = \frac{\langle\psi|H|\psi\rangle}{\langle\psi|\psi\rangle}, \tag{2.30}$$

The minimization of E is the same as extremizing the expression: $\langle\psi|H|\psi\rangle - \lambda\langle\psi|\psi\rangle$, where λ is the Langragian multiplier.

In the general case with matrices of bond dimension χ, the amount of parameters is of order $O(Ld\chi^2)$. The standard procedure of differentiation with respect to each of the parameters would require enormerous complexity for a moderate-sized spin chain and bond dimension.

The key idea of DMRG is to perfrom the optimization by sweeping over localized sites. In the language of MPS, this means to optimize each MPS tensor at a time. As shown in the graphical representation below, the missing tensor is due to the nature of optimization (taking derivatives of the rank-3 tensor $M^{\sigma_i}_{a_i-1,a_i}$). Thanks to the mixed-canonical form of an MPS, we can contract the indices at all other sites (for the term $\lambda\langle\psi|\psi\rangle$).

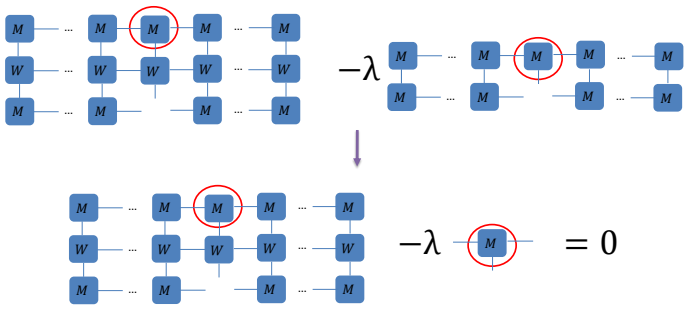

Figure 2: Optimization procedure in graphic representation. We obtain the lower figure using the properties of the mixed canonical form of MPS.

As shown in the figure above, if we reshape the 3 open legs and the 3 legs connecting with the red circle into a single leg, the optimization becomes an eigenvalue problem: where

$$M\nu - \lambda\nu = 0, \tag{2.31}$$

the "matrix" M is built from the MPO and current MPS tensors. The dimension of this eigenvalue problem is $d\chi^2 \times d\chi^2$, from counting the dimensions of the 3 open legs in Fig. 2. Recall that the original problem requires solving the ground state of a $d^L \times d^L$ Hamiltonian, which is exponential in system size. We have obtained a much more efficient method for calcualting the approximate ground state using DMRG.

2.4.1 implementation of the DMRG procedure

In the previous subsection we described how to "locally" optimize the matrices. Recall our original goal is to find the ground state that is optimized globally. To get the globally optimized state we need to perform an iterative procedure, consisting of several "sweeps". The general updating procedure is as follows:

- Start from the initial guess for $|\psi\rangle$, and make sure it is in the right-canonical form (B matrices).

- Calculate the expressions in Fig. 2 iteratively for all sites from $L-1$ to 1 iteratively.
- *Right sweep*: Starting from site $l = 1$ to $L-1$, sweep the lattice sites as follows: solve the eigenproblem for M^{σ_l}, taking its current value as a starting point. Once the solution is obtained, left-canonicalize M^{σ_l} into A^{σ_l} by perforing SVD. The remaining matrices are multiplied to $M^{\sigma_{l+1}}$ to the right and will be the starting guess for the next site. Keep moving one site at each step until site $L-1$ [4].
- *Left sweep*: Starting from site $l = L$ to site 2, sweep the lattice sites to the left. Similar procedure as right sweep, except using SVD to get the right-normalized form and multiply to the left for further calculation. Keep moving one by one until site 2.
- Repeat right and left sweeps until convergence is reached (energy is converged).

If we use matrices A, B, M to represent left-normalized, right-normalized and current site matrices, the algorithm would give rise to the following procedures in a full sweep for a system with four lattice sites:

$$
\begin{aligned}
& M_0B_0B_0B_0 \\
\xrightarrow{diag}\ & M_1B_0B_0B_0 \xrightarrow{SVD} A_1M_0B_0B_0 \\
\xrightarrow{diag}\ & A_1M_1B_0B_0 \xrightarrow{SVD} A_1A_1M_0B_0 \\
\xrightarrow{diag}\ & A_1A_1M_1B_0 \xrightarrow{SVD} A_1A_1A_1M_0 \\
\xrightarrow{diag}\ & A_1A_1A_1M_1 \xrightarrow{SVD} A_1A_1M_1B_1 \\
\xrightarrow{diag}\ & A_1A_1M_2B_1 \xrightarrow{SVD} A_1M_1B_2B_1 \\
\xrightarrow{diag}\ & A_1M_2B_2B_1 \xrightarrow{SVD} M_1B_2B_2B_1
\end{aligned}
\tag{2.32}
$$

In this procedure the energy can only go down: we optimize the energy at each step by varying the parameters. There are two possible issues here: one is the starting state we choose, which may lead to large iteration steps and bad performance if the starting state is "bad"; the other is how can we guarrantee that we have reached the global minimum instead

[4] Using mixed canonical form make the contraction of left and right sites convenient.

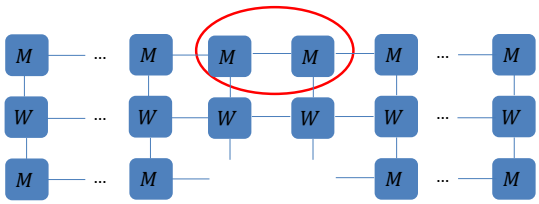

Figure 3: Optimization procedure for two-site updating in graphic representation.

of a local minimum.

To deal with the first issue, we can start the initial state with various χ and generally increase it until results converge (the result is guaranteed to be exact in the $\chi \to \infty$ limit). To deal with the problem of getting stuck at local minimum, we can instead perform optimization on two sites at a time, which offers a slightly enlarged ansatz space with a subsequent truncation which makes the algorithm more robust against getting stuck in a local minimum. The optimization procedure is described as follows.

The DMRG procedure for the two sites is very similar to that for a single site. Fig. 3 shows the graphic representation. Here instead of three open legs we now have 4 open legs for optimization, which increases the complexity by d^2. For spin-$\frac{1}{2}$ system, this will increase the parameter sizes to four times of the original parameter space.

In our numerical calculations, we use iDMRG(infinite-DMRG), which is a general extension of the finite DMRG discussed before, and can be used to build highly controlled translationally invariant (modulo, say, a unit cell of length 2) thermodynamic limit states, more details can be found in Ref.[33].

2.5 Properties of the ground state

Having presented the DMRG procedures for obtaining the ground state, we now discuss how to analyze the properties of ground state. We first discuss the correlation length and ground state energy calculation, then we present the calculation of entanglement entropy

and correlation functions.

2.5.1 correlation length

Correlation length ξ is one of the most important quantities we get from the DMRG calculations, as we will present later in this section, it is closely related to the calculation of the ground state energy, central charge as well as determining whether certain correlation functions decay algebraically or exponentially. As we run DMRG on a specific bond dimension χ, the correlation length naturally depends on χ and we denote such dependence as $\xi(\chi)$.

In practice, conservation laws resulting from global symmetries can be taken into account explicitly in the construction of MPS. This reduces the number of degrees of freedom such that approximations with higher matrix dimensions can be calculated using the same amount of computation time and memory. In the DMRG calculation we separate quantities into various charge sectors and for each charge sector q we can compute $\xi_q(\chi)$, which is the length scale for correlators of form $\langle A^\dagger(0)B(r)\rangle$ where A, B are charge-q operators. If the charge-q sector is gapless, then $\xi_q(\chi)$ goes to infinity as χ increases. If the sector is gapped, then $\xi_q(\chi)$ saturates to its physical value $\xi_q(\infty)$.

The typical dependence of ξ on bond dimension χ for a gapless system is a power law: $\xi \approx \chi^\kappa$. In the code the most used correlation length is the neutral sector ($q = 0$), which is always gapless in our calculation and hence $\xi = -1/(\log s_2)$, where s_2 is the second largest eigenvalue of the normalized reduced density matrix of the system (bipartite density matrix).

Any finite-bond dimension MPS will only approximate the true correlator by a superposition of exponentials, and this works well on short distances, even for power laws[33]. Eventually, the slowest exponential decay will survive, making the correlation into a pure exponential decay with $\xi = -1/(\log s_2)$.

2.5.2 ground state energy

The DMRG procedure we discussed before contains a final step: check convergence. In the convergence check, the first thing to check is the energy: we set a low threshold for δE, which

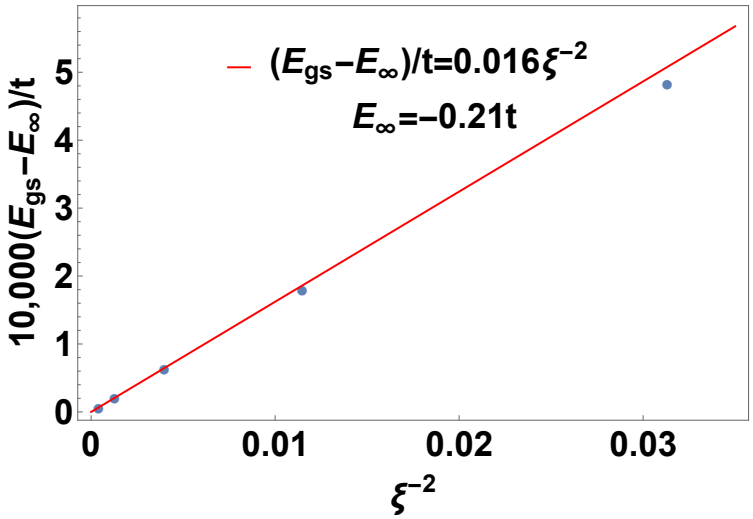

Figure 4: Energy as a function of correlation length. Blue dots are different data points calculated from a set of bond dimensions $\chi = 40, 80, 160, 240, 300$ and red line is the fitting. See chapter 4 for details of the model that we analyze.

is the energy difference after several sweeps. If the energy change is smaller than δE, then we declare that we have reached the ground state[5] and mark the current energy as $E_0(\chi)$.

Recall that the DMRG is running at a finite bond dimension χ, we would expect different values of E_0 for different χ. In practice, we focus on the dependence of energy v.s. correlation length ξ[39]: In practice, we run our DMRG simulations at different bond dimensions and

$$E(\xi) = E_\infty + \frac{A}{\xi^2} + const. \tag{2.33}$$

obtain correlation length $\xi(\chi)$ as well as ground state energy $E(\chi)$. Then we fit the relation between energy and correlation length according to Eq. (2.33) to extract the real ground state energy E_∞. Fig. 4 shows an example of this extrapolation $\chi \to \infty$.

[5]We will present the details of other checks later in this section.

2.5.3 entanglement entropy

Another important quantities that we calculate to analyze the ground state property is the entanglement entropy S. Specifically we measure the bipartite entanglement entropy: for a bipartite system AB the entanglement entropy is defined as: where $\rho_{A/B}$ are the reduced

$$S = -Tr_{\rho_A} \log \rho_A = -Tr_{\rho_B} \log \rho_B, \tag{2.34}$$

density matrix of subsystem A/B.

The entanglement entropy is infinite for a true ground state ($\xi \to \infty$), but is cut off by finite bond dimension χ. In the code we are using infinite system DMRG with a unit cell and we calculate the entanglement entropy by averaging over the bonds within the unit cell. The sample code for calculating entanglement entropy is shown below:

```
1       def entanglement_entropy(self, n = 1):
2               """ Calculate the entanglement entropy for all the bonds, and
                    return a np.ndarray.
3               S = []
4               if n==1:
5                       for i_bond in range(0, len(self.s)):
6                               s=self.s[i_bond][self.s[i_bond]>10**(-16)]**2
7                               S.append(-np.inner(np.log(s),s))
8               return np.array(S)
```

As shown in the code above, the entanglement entropy for a specific bond is defined as $S = -\sum_i s_i^2 \log s_i^2$ where s_i are the eigenvalues for each bond.

2.5.4 correlation functions

Finally in the DMRG calculations we calculate various correlation functions. More specifically, we focus on the two-point correlation functions separated by distance r. As mentioned before we can tell whether certain correlation decay algebraically or exponentially up to

the correlation length to determine whether the mode that associated with the correlation function is gapless or gapped. In Chpater 4 and 5 we present details of correlation functions we measure and how we use them to identify phases, respectively.

2.6 DMRG sample code

In this section we present a sample code for our DMRG calculation. The code here is for certain calculations related to Chapter 4. We will break the sample code into parts where we explain the purpose of each part. The code is a slight modification from our collaborator Prof. Roger Mong and the libaray we use is TenPy.

```
import sys
import numpy as np
from copy import deepcopy
import itertools
from fractions import Fraction as F

from models import dual_ising
from mps.mps import iMPS
from algorithms import simulation
from algorithms.linalg import np_conserved as npc
from tools.string import joinstr, to_mathematica_lists
import cluster.omp as omp
import os
```

In this part we load the libraries and packages we need for our DMRG calculations. The model used here is *dual_ising* model which enables calculations of two types of particles and we perfrom calculations on fixed filling fraction of particles based on *np_conserved* package. The Hamiltonian is: we will discuss in detail about this model in Chapter 4.

```
def pipe_output(outfile, verbose=0):
   #sys.stdout = default_stdout
   #sys.stderr = default_stderr
   if verbose:
      print "Piping to \"%s\"." % (outfile,)
   # open our log file
   so = se = open(outfile, 'w', 0)
   # re-open stdout without buffering
   sys.stdout = os.fdopen(sys.stdout.fileno(), 'w', 0)
   # redirect stdout and stderr to the log file opened above
```

$$
\begin{aligned}
H = &- \sum_i t_1 \left(c^\dagger_{i,1} c_{i+1,1} + \text{h.c.} \right) - \sum_{i\sigma} (\mu_1 - 2t_1) n_{i,1} \\
&- \sum_i t_2 \left(c^\dagger_{i,2} c_{i+1,2} + \text{h.c.} \right) - \sum_{i\sigma} (\mu_2 - 2t_2) n_{i,2} \\
&+ \sum_i U_{1,2} n_{i,1} n_{i,2},
\end{aligned} \tag{2.35}
$$

```
11    os.dup2(so.fileno(), sys.stdout.fileno())
12    os.dup2(se.fileno(), sys.stderr.fileno())
13    print "Running with {} threads".format(omp.get_max_threads())
```

This is the function for output logfiles for our calculations. We need this part to see the result of our code at each step, I will show a sample logfile at the end of this chapter.

```
1  def gcd(a, b):
2          """Greatest common divisor. Return 0 if both a,b are zero, otherwise
               always return a non-negative number."""
3          a = abs(a)
4          b = abs(b)
5          while b > 0:
6                  a, b = b, a % b    # after this, a > b
7          return a
8
9  def lcm(a, b):
10         if a == 0 and b == 0: return 0
11         return a * b / gcd(a, b)
```

These are the functions we use to calculate greatest common divisor and lowest common multiplier. We need this function to determin the size of the unit cell in our calculation. As an example, if our filling fraction here for two types of particles are 1/2 and 2/5 respectively, we would need a unit cell of size 10.

```
1  def model_GaudinYang2(V1, V2, nu1, nu2, t1, t2):
2          r"""
3          H =  \sum_{a,s} t_s (c_a - c_{a+1})^\dag (c_a - c_{a+1})
4                  - \sum_{a,s} \mu_s c_a^\dag c_a
5                  + U \sum_a n_{1,a} n_{2,a}
```

```
        + (1/2) \sum_{a,s,s'} V_{s,s'} n_{s,a} n_{s',a}
    where we set \mu = 0, V = 0.

    Under the Jordan-Wigner transformation:
        c^\dag <--> S^- * string
        c^\dag c <--> 1/2 - S^z.
    """
    V1, V2, t1, t2 = float(V1), float(V2), float(t1), float(t2)
    hop_list = [ ('pIX','pXI',-t1/2), ('pIY','pYI',-t1/2),
        ('pZI','pZI',V2/2), ('pIZ','pIZ',V2/2), ('pIZ','pII',0),
        ('pII','pZI',0), ('pZZ','pII',V1/4), ('pII','pZZ',V1/4),
        ('pIZ','pZI',V1/2), ('pXX','pII',-t2/4), ('pII','pXX',-t2/4),
        ('pYY','pII',-t2/4), ('pII','pYY',-t2/4) ]
    configL = lcm(nu1.denominator, nu2.denominator)
    if configL == 1: configL = 2
    config = [ np.ediff1d(np.rint(np.linspace(0, nu * configL, num = configL
        + 1, endpoint = True)).astype(int)) for nu in [nu1, nu2] ]
    Mpar = {
        'L': 1,
        'verbose': 1,
        'gxx': 0,
        'gyy': 0,
        'gzz': 0,
        'hSz': 0,
        'hTz': 0,
        'constant offset': 0,
        'extra_hoppings': [hop_list],
        'conserve_Sz': False,
        'conserve_diff_Sz': False,
        'dtype': float,
        'parstring': 'xxzt{},{}_,V{},{}_nu{}o{},{}o{}'.format(t1, t2, V1,
            V2, nu1.numerator, nu1.denominator, nu2.numerator,
            nu2.denominator),
        'root config 1': config[0],
        'root config 2': config[1],
    }
    return Mpar
```

In this part we define the model we use for our calculation, which is GaudinYang in this case. We perform Jordan-Wigner transformation to go from a lattice model to a spin model [6], and we have mapped the parameters accordingly. The *parstring* serves as the name for our logfile as well as output file where it includes the parameters and filling fractions for both particle types.

[6] the details of Jordan-Wigner transformation can be found in Chapter 4.

```
default_sim_par = {
        'VERBOSE': True,
        'STARTING_ENV_FROM_PSI': 1,
        'N_STEPS': 20,
        'MAX_ERROR_E': 1e-10,
        'MAX_ERROR_S': 1e-6,
        'MIN_STEPS': 40,
        'MAX_STEPS': 200,
        'LANCZOS_PAR' : {'N_min': 2, 'N_max': 20, 'e_tol': 5*10**(-15),
           'tol_to_trunc': 1/5.},
#       'mixer': (1e-3, 1.5, 5, 'id'),
}

def run_dmrg(sim, dmrg_par, model_par=None, chi=None, min_steps=None,
    save_sim=False):
        if sim is None:
                print 'Initializing "{}"...'.format(model_par['parstring'])
                M = dual_ising_dp2.dual_ising_model(model_par)

                ##      Compute the initial state from the root configurations
                state_ordering = ['up', 'dn']       # 0 is spin up, 1 is spin dn
                initial_state = np.array([
                    M.states[0][state_ordering[s1]+state_ordering[s2]] for s1,s2
                    in itertools.izip(model_par['root config 1'], model_par['root
                    config 2']) ])
                print joinstr(["Initial configs: ", str(model_par['root config
                    1']) + '\n' + str(model_par['root config 2'])])
                psi = iMPS.product_imps(M.d, initial_state, dtype=float,
                    conserve=M, bc='periodic')

                sim = simulation.simulation(psi, M)
                sim.model_par = model_par

        else:
                if model_par is not None:
                        print 'Updating simulation
                            "{}"...'.format(model_par['parstring'])
                        sim.update_model(model_par)
                else:
                        print 'Running simulation
                            "{}"...'.format(model_par['parstring'])
                try:
                        del sim.canon_psi
                except:
                        pass

        sim_par = deepcopy(dmrg_par)
```

```
        if chi is not None: sim_par['CHI_LIST'] = {0:chi}
        if min_steps is not None: sim_par.update['MIN_STEPS'] = min_steps
        sim.dmrg_par = sim_par
        print 'DMRG parameters:\n' + '\n'.join([ " {} : {}".format(k,v) for k,v
            in sim.dmrg_par.items() ])
        sim.ground_state()

        try:
                sim.append
        except AttributeError:
                sim.append = {}
        if 'xi' in sim.append: del sim.append['xi']

        sim.append['GS Energy'] = sim.sim_stats[-1]['Es'][-1]
        sim.canon_psi = sim.psi.copy()
        sim.canon_psi.canonical_form()
        if save_sim:
                filename = outroot + model_par['parstring'] +
                    '_chi{}'.format(max(sim_par['CHI_LIST'].values()))
                uncanon_psi = sim.psi
                sim.psi = sim.canon_psi
                print 'Presaving simulation to "{}"...'.format(filename)
                sim.save(filename)
        sim.append['xi'] = sim.canon_psi.correlation_length()
        print "xi = {}".format(sim.append['xi'])

        sim.append['Sbond'] = np.average(sim.canon_psi.entanglement_entropy())
        print "Sbond = {}".format(sim.append['Sbond'])

        print "Egs = {}".format(sim.append['GS Energy'])

        if save_sim:
                print 'Saving simulation to "{}"...'.format(filename)
                sim.save(filename)
                sim.psi = uncanon_psi
        print
        return sim
```

This part is the DMRG paramters and *run_dmrg* is the function we use for calculating the ground state. We observe here that in this calculation we calculated ground state energy *'GS Energy'*, correlation length *'xi'* and entanglement entropy *'Sbond'*.

```
def load_sim(model_par, chi, verbose=1):
        filename = outroot + model_par['parstring'] + '_chi' + str(chi)
        print 'Loading "{}"...'.format(filename)
        try:
```

```
                sim = simulation.simulation.load(filename,
                    dual_ising_dp2.dual_ising_model, force_mod_verbose=0)
        except IOError, e:
                if verbose >= 1: print " IOError!", e
                return None
        return sim


def measure_correlator(sim):
        if hasattr(sim, 'canon_psi'):
                psi = sim.canon_psi
        else:
                psi = sim.psi
        M = sim.M
        xi = sim.append['xi']
        dist = int(5 * xi)

        site_n1 = 0.5 - psi.site_expectation_value(M.Sz)
        site_n2 = 0.5 - psi.site_expectation_value(M.Tz)
        print "Occupation number <n1> = {}, <n2> = {}".format(site_n1, site_n2)
        corr_c1d_c1 = psi.correlation_function(M.SmZ, M.SpI, 200, OpStr=M.pZZ)
        corr_c2d_c2 = psi.correlation_function(M.ISm, M.ZSp, 200, OpStr=M.pZZ)
        print corr_c1d_c1[:10]
        print corr_c2d_c2[:10]
        print sim.append['Sbond']
```

This part shows how we can load previous calculations and analyze the properties of the ground state by measure the correlation functions. Specifically, the sample code shown here calculates the occupation number for both particles, single correlator for both particles $\langle c_1^\dagger(r)c_1(0)$ and $\langle c_2^\dagger(r)c_2(0)$.

```
np.set_printoptions(linewidth=2000, precision=5, threshold=4000)
outroot = 'testmpo/sim/'            # this determines where everything is
    saved/loaded.
outroot2 = 'testmpo/log/'    # this is where all the log files are
nn = 3

nn1 = int(sys.argv[1])
nn2 = int(sys.argv[2])
t1 = float(sys.argv[3])
t2 = float(sys.argv[4])
V1 = float(sys.argv[5])
V2 = float(sys.argv[6])

##############################################################################
```

```
14 if 1:                        # run simulation and save for positive U
15         for n1 in [nn1]:
16                 for n2 in [nn2]:
17                         model_par = model_GaudinYang2(V1, V2, F(n1,nn), F(n2,nn),
                               t1, t2)
18                         for ii in range(1):
19                                 sim = load_sim(model_par, [40, 80, 160, 300][ii])
20                                 if sim is None:
21                                         sim_par = deepcopy(default_sim_par)
22                                         CHI_LIST = dict([(0,14), (20,20), (40,28),
                                               (80,40), (120,80), (300,160),
                                               (500,300)][:ii+4])
23                                         logfile = outroot2 + model_par['parstring']
                                               + '_chi{}.out'.format([40, 80, 160,
                                               300][ii])
24                                         print logfile
25                                         pipe_output(logfile)
26                                         sim_par.update({'CHI_LIST':CHI_LIST,
                                               'MIN_STEPS':1.5*max(CHI_LIST.keys())})
27                                         sim = run_dmrg(None, sim_par,
                                               model_par=model_par, save_sim=True)
28                                         measure_correlator(sim)
29                                 else:
30                                         continue
31
32
33 ############################################################
34
35 if 0:                                  #measure correlator
36         datalist=[]
37         for V1 in [1]:
38                 for V2 in [1]:
39                         model_par = model_GaudinYang2(V1, V2, F(n1,nn), F(n2,nn),
                               t=0.0)
40                         for chi in [40, 80]:
41                                 sim = load_sim(model_par,chi)
42                                 if sim is None: continue
43                                 if hasattr(sim, 'canon_psi'):
44                                         psi = sim.canon_psi
45                                 else:
46                                         psi = sim.psi
47                                 M = sim.M
48                                 xi = sim.append['xi']
49                                 site_n1 = 0.5 - psi.site_expectation_value(M.Sz)
50                                 site_n2 = 0.5 - psi.site_expectation_value(M.Tz)
51                                 dist = int(5 * xi)
52                                 corr_c1d_c1 = psi.correlation_function(M.SmZ,
```

```
                                    M.SpI, 200, OpStr=M.pZZ)
53                                corr_pairing = psi.correlation_function(M.SpSp,
                                    M.SmSm, dist+20, OpStr=M.pII)
54                                datalist.append([n1,n2,site_n1,site_n2,sim.append['xi'],
55                                sim.append['Sbond'],
56                                sim.append['GS Energy'],
57                                corr_c1d_c1,corr_c2d_c2,corr_pairing,corr_pairing2])
58  #       print to_mathematica_lists(datalist)
59          file = open("nnnPair.txt", "w")
60          file.write(to_mathematica_lists(datalist))
61          file.close()
```

This part shows how we set up the parameters and run our simulations at various bond dimensions. The first part is the calculation procedure where we perform DMRG calcualtions at various bond dimensions, keep log files at each step and save the result as sim files. The second part is the measurement part where we can load the sim file we have calculated before and calculate the properties of the ground state at each bond dimension: correlation length, particle number, single correlators such as $c_1^\dagger(r)c_1(0)$ and pair correlators such as $\langle c_1^\dagger(r)c_2^\dagger(r)c_2(0)c_1(0)\rangle$. In the end we can output the results into a .txt file which we can analyze using Mathematica.

2.6.1 sample output file

In this subsection we show a sample output file, which we will discuss the steps of our DMRG and the convergence criteria. This logfile is for two species both at filling fraction 1 and the interaction between them is $U = -3$ and hopping parameter $t = 1$.

```
1   Running with 8 threads
2   Initializing "t1.0,1.0_U-3.0_nu1o1,1o1"...
3   dual ising model
4           verbose: 1
5           L = 1
6           dtype = <type 'float'>
7           constant offset = 1.25
8           hSz = -0.5
9           hTz = -0.5
10          gzz = -3.0
11          extra_hoppings = [[('pXI', 'pXI', -0.5), ('pYI', 'pYI', -0.5), ('pIX',
                'pIX', -0.5), ('pIY', 'pIY', -0.5)]]
```

```
        Checking for Sz conservation...
        Checking for complex numbers...
        conserving Sz, (num_q = 2)
        mpo chi: [6]
Init model with num_q = 2
Initial configs: [1 1]
                 [1 1]
DMRG parameters:
  CHI_LIST : {0: 14, 40: 28, 20: 20, 80: 40}
  LANCZOS_PAR : {'N_max': 20, 'e_tol': 5.000000000000001e-15, 'tol_to_trunc':
      0.2, 'N_min': 2}
  MAX_ERROR_S : 1e-08
  VERBOSE : True
  MIN_STEPS : 120.0
  MAX_ERROR_E : 1e-12
  STARTING_ENV_FROM_PSI : 1
  N_STEPS : 20
  MAX_STEPS : 2000
```

In this part the log file outputs the parameters we use for this DMRG simulation, such as hopping parameter t, bond dimensions χ and convergence parameters: $MAX\_ERROR\_S = 1e-08$ and $MAX\_ERROR\_E = 1e-12$ which means the simulation is converged only if the differences between current and previous calculated energies and entanglement entropies are smaller than these two numbers.

```
Finding ground state...
Using 0_new engine.
Initializing environment from scratch.
Updating environment .
Beginning optimization...
this sim has 72000 s before everything is shelved
Changing to chi max = 14
Peak memory used (mb) 41.828125 Time elapsed 0.3
 ----> step =  20   chi = [1, 1] Normerr = 0.0 ESys = 1.0000000000000000 Sbond =
     0.0000000000
 Etrunc = 0.0000e+00 Ptrunc = 0.0000e+00 D_ESys = 0.0000e+00 D_S = 0.0000e+00

Changing to chi max = 20
Peak memory used (mb) 41.828125 Time elapsed 0.6
 ----> step =  40   chi = [1, 1] Normerr = 0.0 ESys = 1.0000000000000000 Sbond =
     0.0000000000
 Etrunc = 0.0000e+00 Ptrunc = 0.0000e+00 D_ESys = 0.0000e+00 D_S = 0.0000e+00

Changing to chi max = 28
Peak memory used (mb) 41.828125 Time elapsed 0.8
```

```
 ----> step =  60   chi = [1, 1] Normerr = 0.0 ESys = 1.0000000000000000 Sbond =
    0.0000000000
 Etrunc = 0.0000e+00 Ptrunc = 0.0000e+00 D_ESys = 0.0000e+00 D_S = 0.0000e+00

Peak memory used (mb) 41.828125 Time elapsed 1.1
 ----> step =  80   chi = [1, 1] Normerr = 0.0 ESys = 1.0000000000000000 Sbond =
    0.0000000000
 Etrunc = 0.0000e+00 Ptrunc = 0.0000e+00 D_ESys = 0.0000e+00 D_S = 0.0000e+00

Changing to chi max = 40
Peak memory used (mb) 42.0 Time elapsed 1.3
 ----> step = 100   chi = [1, 1] Normerr = 0.0 ESys = 1.0000000000000000 Sbond =
    0.0000000000
 Etrunc = 0.0000e+00 Ptrunc = 0.0000e+00 D_ESys = 0.0000e+00 D_S = 0.0000e+00

Peak memory used (mb) 42.0 Time elapsed 1.6
 ----> step = 120   chi = [1, 1] Normerr = 0.0 ESys = 1.0000000000000000 Sbond =
    0.0000000000
 Etrunc = 0.0000e+00 Ptrunc = 0.0000e+00 D_ESys = 0.0000e+00 D_S = 0.0000e+00

Peak memory used (mb) 42.0 Time elapsed 1.9
 ----> step = 140   chi = [1, 1] Normerr = 0.0 ESys = 1.0000000000000000 Sbond =
    0.0000000000
 Etrunc = 0.0000e+00 Ptrunc = 0.0000e+00 D_ESys = 0.0000e+00 D_S = 0.0000e+00

Time per [ steps * L * (chi/64)^3 ]: 1737.9265625
Time per [ steps * L * (chi/16)^3 * d^3 * D]: 4.52595563616
Peak memory used (mb) 42.0
DMRG time: 1.85642194748s, memory: 42.0Mb
Presaving simulation to "MI/t1.0,1.0_U-3.0_nu1o1,1o1_chi40"...
xi = 0.0
Sbond = 0.0
Saving simulation to "MI/t1.0,1.0_U-3.0_nu1o1,1o1_chi40"...
```

This part shows the log outputs of DMRG at each step in unit of 20 steps. At each step it outputs the energy and entanglement entropy. It also changes bound dimension at certain steps. In the end when the code converges it outputs the time and memory used and saving the result to a sim file.

2.7 summary

In this chapter we have presented the DMRG algorithm as well as instructions on how we run TenPy2 DMRG code. We used MPS representation and graphical notation to discuss the DMRG algorithms. We showed that any quantum state can be written in the MPS form and any operators can be written in MPO form. After this we discussed about how to get the ground state using the MPS language and the procedure for obtaining the ground state via sweeps. Next, we discussed how to analyze the properties of the ground state, i.e., the correlation length, ground state energy, entanglement entropy and correlation functions. Finally we showed our sample code for DMRG calculation as well as a sample log file with which we discussed the convergence criteria for our DMRG simulations.

3.0 TOMANAGA-LUTTINGER LIQUID THEORY

In this chapter we provide a brief overview of Tomanaga-Luttinger liquid (TLL) theory. We first discuss how Fermi liquid theory fails in one dimension. Then we introduce the concept of TLL and the exact mapping between fermions and bosons in one dimension, as well as the bosonization scheme. We also discuss the effects of interactions and spatial decay of various correlators in the TLL. The discussions in this chapter follows Ref[40].

3.1 Fermi liquid theory and the the peculiarity one dimension

We first discuss the effects of interactions in higher dimensions. The excitations for a free electron gas is adding particles with well-defined momentum k and energy $\epsilon(k)$. These excitations have infinite lifetime since they are eigenstates of the Hamiltonian. The probability of finding a state with frequency ω and momentum k, i.e. the spectral function $A(k,\omega) = -\frac{1}{\pi} ImG(k,\omega)$ ($G(k,\omega)$ is the retarded Green's function), for the free electron is $A(k,\omega) = \delta(\omega - \xi(k))$, where $\xi(k)$ is the energy relative to the chemical potential $\xi(k) = \epsilon(k) - \mu$.

The remarkable result of Fermi liquid theory is that when interactions are turned on, the properties of the system remain essentially similar, except that the elementary particles (qusiparticles) have now been dressed by density fluctuations around them. The quasiparticle excitations are not completely free and they have a lifetime τ, which leads to a Lorentzian in the spectral function instead of the delta function as in the free electron case.

In one dimension, however, interactions have drastic effects. Unlike higher dimensions where low-energy scattering at the Fermi surface can have arbitrary momentum transfer, in

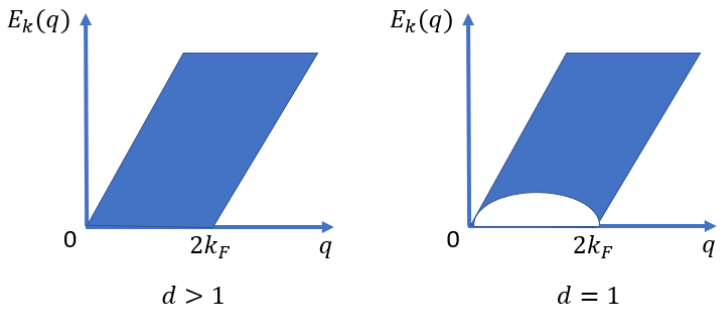

Figure 5: Particle-hole spectrum for higher dimensions (left) and for one dimension (right). In one dimension, particle-hole excitations have both a well-defined momentum and energy for small momentum q.

1D only forward and back scattering is possible. As a result, the particle-hole excitations in one dimension have both a well-defined momentum and energy (for small momentum q), as shown in Fig. 5. The theory to describe the 1D interacting electron gas is known as the Tomanaga-Luttinger Liquid (TLL) theory.

3.2 Bosonization

The history of TLL theory goes back to the work of Tomanaga in 1950[41] where he suggested that excitations in one-dimensional systems could be described by a "quantized field of sound waves". Luttinger developed this theory into a model that he incorrectly solved in 1963[42]. Later, Mattis and Lieb fixed the mistake in 1965[43] and Haldane invented the term "Tomanaga-Luttinger liquid" and discovered a nice physical interpretation of the meaning of bosonization in one dimension, which we discuss in the following.

As we have seen in Fig. 5, the particle-hole excitations have a nearly linear spectrum, with well-defined momentum and energy. To make the relation perfect consider the Tomanaga-Luttinger model where the spectrum is purely linear. The Hamiltonian is as follows: where $r = R/L$ stands for right/left-moving fermions and $\epsilon_R = 1, \epsilon_L = -1$. The particle-hole excitations for the right-moving partciles are given by: which are independent of k and are well-defined with a well-defined momentum k and a well-defined energy $E = v_F q$. The density fluctuations are a superposition of particle-hole excitations: Note here the density

$$H = \sum_{k;r=R,L} v_F(\epsilon_r k - k_F) c^\dagger_{r,k} c_{r,k}, \tag{3.1}$$

$$E_{R,k}(q) = v_F(k+q) - v_f k = v_F q, \tag{3.2}$$

$$\rho^\dagger(q) = \sum_k c^\dagger_{k+q} c_k. \tag{3.3}$$

operator is of bosonic nature as it is made of a product of two fermion operators.

One can readily check the commutation relations of the density operators[40]: where $r =$

$$\left[\rho^\dagger_r(p), \rho^\dagger_{r'}(-p')\right] = \delta_{r,r'}\delta_{p,p'}\frac{rp\mathcal{L}}{2\pi}, \tag{3.4}$$

$+1$ for $r = R$ and $r = -1$ for $r = L$ and $\mathcal{L}$ is the length. The above relation shows that the density operators have similar commutation relations to boson operators. In addition, if we choose $|0\rangle$ as the non-interacting ground state of Eq. (3.1), we have In this regard we can identify the density operators as the destuction operators for bosons. One can readily define the boson creation operators as: where Θ is the step function and bosons are defined except for $p = 0$. One can check the commutation relation between b_p and the Hamiltonian H: $[b_{p_0}, H] = v_F p_0 b_{p_0}$, which leads to: which shows that the kinetic energy is quadratic in terms of boson operators. Note that the interaction term is typically a product of four

$$\rho_L^\dagger(p>0)|0\rangle = 0$$
$$\rho_R^\dagger(p<0)|0\rangle = 0. \tag{3.5}$$

$$b_p^\dagger = \left(\frac{2\pi}{\mathcal{L}|p|}\right)^{1/2} \sum_r \Theta(rp)\rho_r^\dagger(p), \tag{3.6}$$

$$H \simeq \sum_{p\neq 0} v_F|p| b_p^\dagger b_p, \tag{3.7}$$

fermion operators and thus also quadratic in the boson operators, which allows solving the interacting problem in a remarkably simple way.

It is convenient to introduce two bosonic fields $\phi(x)$ and $\theta(x)$ defined by: where upper

$$\phi(x), \theta(x) = \mp(N_R \pm N_L)\frac{\pi x}{\mathcal{L}} \mp \frac{i\pi}{\mathcal{L}} \sum_{p\neq 0} \frac{1}{p} e^{-ipx}(\rho_R^\dagger(p) \pm \rho_L^\dagger(p)), \tag{3.8}$$

signs are for $\phi(x)$ and N_R, N_L are the numbers of fermions in the right-/left-moving sectors. Using these fields the exact expressions for the Hamiltonian and the single-particle operator are: where U_r commutes with the boson operators and $U_r^\dagger$ adds one fermion of species r.

Based on Eq. (3.6) one can rewrite the two bosonic fields $\phi(x)$ and $\theta(x)$ as: The fields $\phi(x)$ and $\theta(x)$ satisfy simple commutation rules and Define the conjugate momentum $\Pi(x) =$

$$H = \sum_{p\neq 0} v_F|p|b_p^\dagger b_p + \frac{\pi v_F}{\mathcal{L}}\sum_r N_r^2$$
$$\psi_r(x) = U_r \lim_{\alpha\to 0}\frac{1}{\sqrt{2\pi\alpha}} e^{ir(k_F-\pi/\mathcal{L})x} e^{-i[r\phi(x)-\theta(x)]} \tag{3.9}$$

$$\phi(x) = -(N_R+N_L)\frac{\pi x}{L} - \frac{i\pi}{L}\sum_p \left(\frac{L|p|}{2\pi}\right)^{1/2}\frac{1}{p}e^{-ipx}(b_p^\dagger + b_{-p})$$
$$\theta(x) = (N_R-N_L)\frac{\pi x}{L} - \frac{i\pi}{L}\sum_p \left(\frac{L|p|}{2\pi}\right)^{1/2}\frac{1}{p}e^{-ipx}(b_p^\dagger - b_{-p}). \tag{3.10}$$

$$[\phi(x_1), \nabla\theta(x_2)] = i\pi\theta(x_2-x_1) \tag{3.11}$$

$\frac{1}{\pi}\nabla\theta(x)$ we obtain:

$$[\phi(x_1), \Pi(x_2)] = i\delta(x_2-x_1). \tag{3.12}$$

The Hamiltonian can be rewritten in terms of the new fields: In the thermodynamic

$$H = \frac{1}{2\pi}\int dx v_F[(\pi\Pi(x))^2 + (\nabla\phi(x))^2] \tag{3.13}$$

limit $\mathcal{L} \to \infty$ the single operator becomes

$$\psi_r(x) = \frac{U_r}{\sqrt{2\pi\alpha}} e^{irk_F x} e^{-i[r\phi(x)-\theta(x)]} \tag{3.14}$$

3.3 spectra equivalence of boson and fermion in 1D

Having discussed the bosonization scheme in the previous section, we now show the spectral equivalence of bosons and fermions in one dimension.

Based on Eq. (3.9) a state in the bosonic basis is characterized by the total number of fermions of each species N_r and the bosonic numbers of each momentum n_p. Define $U_{R/L}$ such that we can readily write down the basis state as: where $|0\rangle$ is the vacuum.

$$\begin{aligned} U_R^\dagger |N_R, N_L\rangle &= |N_R + 1, N_L\rangle \\ U_L^\dagger |N_R, N_L\rangle &= |N_R, N_L + 1\rangle, \end{aligned} \tag{3.15}$$

$$|N_R, N_L, n_p\rangle = \prod_p \frac{(b_p^\dagger)^{n_p}}{(n_p!)^{1/2}} (U_R^\dagger)^{N_R} (U_L^\dagger)^{N_L} |0\rangle, \tag{3.16}$$

To check the completeness of the bosonic representation we calculate the partition function in both the fermionic and bosonic representations. In the fermionic representation the energy is: using the quantization relation for k and putting Fermi levels in the mid point. A single state above the Dirac sea contributes to the partition function as: where $\omega = e^{-\beta\pi v_F/L}$.

$$\xi_{r,k} = v_F(rk - k_F) = v_F(r\frac{2\pi n}{\mathcal{L}} - \frac{2\pi n_F}{\mathcal{L}} - \frac{\pi}{\mathcal{L}}), \tag{3.17}$$

$$Z_1 = 1 + e^{-\beta|\xi_{r,k}|} = 1 + \omega^{|2(rn-n_F)-1|}, \tag{3.18}$$

Note that there are two branches of excitations (right and left), thus the total partition function is: where the exponent of ω is always positive and we have shifted the definition of

$$Z = \left[\prod_{n=1}^{\infty}(1+\omega^{2n-1})^2\right]^2, \tag{3.19}$$

n.

In the bosonic representation, the contribution to the partition function from a single boson of energy $\epsilon_n = v_F 2\pi|n|/L$ is:

$$Z_{1B} = \sum_{m=0}^{\infty} e^{-\beta m\epsilon} = \frac{1}{1-\omega^{2n}}. \tag{3.20}$$

The total boson partition function is: Note that there is another contribtion to the partition function from the states $|N_R, N_L\rangle$ is: Thus the total partition function in the bosonic representation is:

If we compare Eq. (3.19) and Eq. (3.23), we notice that they are quite different. However, using the Jacobi Triple product Identity: we see that the bosonic partition function and the

$$Z_b = \prod_{n\neq 0} \frac{1}{1-\omega^{2n}} = \left[\prod_{n=1}^{\infty} \frac{1}{1-\omega^{2n}}\right]^2. \tag{3.21}$$

$$Z_N = \left[\sum_{m=-\infty}^{\infty} \omega^{m^2}\right], \tag{3.22}$$

$$Z_b = \left[\prod_{n=1}^{\infty} \frac{1}{1-\omega^{2n}} \sum_{m=-\infty}^{\infty} \omega^{m^2}\right]^2. \tag{3.23}$$

$$\sum_{m=-\infty}^{\infty} q^{m^2} = \prod_{n=1}^{\infty} (1+q^{2m-1})^2(1-q^{2m}), \tag{3.24}$$

fermionic partition are equivalent and thus the spectra are equivalent.

3.4 effects of interactions

Having shown that the mapping between fermion and boson is exact, we now discuss the effects of interactions. One can argue that the interaction is of form[40]:

For spinless fermions we only need to consider the g_4 (forward-scattering) and g_2 (backscattering) processes: the g_4 process can be written as: and similar terms for the left movers ($R \to L$ and $\phi - \theta \to \phi + \theta$). The sum of these two terms gives:

$$H = \int dx V(x - x')\rho(x)\rho(x'). \tag{3.25}$$

$$\begin{aligned} \frac{g_4}{2}\psi_R^\dagger(x)\psi_R(x)\psi_R^\dagger(x)\psi_R(x) &= \frac{g_4}{2}\rho_R(x)\rho_R(x) \\ &= \frac{g_4}{2}\frac{2}{(2\pi)^2}(\nabla\phi - \nabla\theta)^2, \end{aligned} \tag{3.26}$$

$$\frac{g_4}{(2\pi)^2}\int dx[(\nabla\phi)^2 + (\nabla\theta)^2]. \tag{3.27}$$

Recall Eq. (3.13), one sees that the g_4 process only renormalizes the velocity, which becomes:

$$u = v_F(1 + \frac{g_4}{2\pi v_F}). \tag{3.28}$$

Similarly, the backscattering process g_2 can be written as: where we have considered the

$$\begin{aligned} g_2\psi_R^\dagger(x)\psi_R(x)\psi_L^\dagger(x)\psi_L(x) &= g_2\rho_R(x)\rho_L(x) \\ &= \frac{g_2}{(2\pi)^2}[(\nabla\phi)^2 - (\nabla\theta)^2], \end{aligned} \tag{3.29}$$

q independent interaction processes (δ function in real space).

Combining the g_4 and g_2 process, we can rewrite the Hamiltonian as: where u has

$$H = \frac{1}{2\pi}\int dx[uK(\pi\Pi(x))^2 + \frac{u}{K}(\nabla\phi(x))^2], \tag{3.30}$$

dimension of velocity and K is dimensionless: For repulsive interactions ($g_2 > 0$) we have

$$\begin{aligned} u &= v_F[(1+\frac{g_4}{2\pi v_F})^2 - (\frac{g_2}{2\pi v_F})^2]^{1/2} \\ K &= \left(\frac{2\pi v_F + g_4 - g_2}{2\pi v_F + g_4 + g_2}\right)^{1/2}. \end{aligned} \tag{3.31}$$

$K < 1$ and for attractive interactions ($g_2 < 0$) we have $K > 1$.

Note here we have "solved" the spinless fermions with "weak" interactions in one-dimension. The case of spin-1/2 fermions can be solved in essentially the same manner using spin-charge separation. More details can be found in [40]. In the next sections we will discuss the correlation functions in TLL.

3.5 correlation functions in TLL

We start with the density-density correlation function. In the continuum model[40] and the

$$\psi(x) = \psi_R(x) + \psi_L(x) \tag{3.32}$$

density $\rho(x) = \psi(x)^\dagger\psi(x)$ composes of four terms. Recall Eq.(3.14) and Eq.(3.8), we get

$$\begin{aligned}\rho(x) &= \rho_R(x) + \rho_L(x) + [\psi_R^\dagger(x)\psi_L(x) + h.c.] \\ &= -\frac{1}{\pi}\nabla\phi(x) + \frac{1}{2\pi\alpha}[e^{i2k_F x}e^{-i2\phi(r)} + h.c.]\end{aligned} \tag{3.33}$$

$$\langle\rho(r)\rho(0)\rangle = \frac{1}{\pi^2}\langle\nabla\phi(r)\nabla\phi(0)\rangle + \frac{1}{(2\pi\alpha)^2}[e^{-i2k_F x}\langle e^{i(2\phi(r)-2\phi(0))}\rangle + h.c.] \tag{3.34}$$

The density-density correlation is then where $\langle\dots\rangle$ denotes the time-ordered average. Evaluating the 2-point correlation functions[40]: For $T = 0$ we get: where $r = (x, u\tau)$ and

$$\begin{aligned}\langle[\phi(r) - \phi(0)]^2\rangle &= KF_1(r) \\ \langle[\theta(r) - \theta(0)]^2\rangle &= K^{-1}F_1(r) \\ \langle[\phi(r)\theta(0)]\rangle &= \frac{1}{2}F_2(r)\end{aligned} \tag{3.35}$$

$$\begin{aligned}F_1(r) &= \frac{1}{2}\log[\frac{x^2 + (u|\tau| + \alpha)^2}{\alpha^2}] \\ F_2(r) &= -i\mathrm{Arg}(y_\alpha + ix)\end{aligned} \tag{3.36}$$

$y_\alpha = u\tau + \alpha\mathrm{Sign}(\tau)$.

For a quadratic Hamiltonian one has for any number of A_j and B_j: This allows us to

$$\langle e^{i\sum_j (A_j\phi(r_j)+B_j\theta(r_j))}\rangle = e^{-\frac{1}{2}\langle(\sum_j A_j\phi(r_j)+B_j\theta(r_j))^2\rangle} \tag{3.37}$$

calculate all correlation functions. Here we only present the results[1].

The density-density correlation function is The non-oscillatory part (first term on the

$$\langle\rho(r)\rho(0)\rangle = \frac{K}{2\pi^2}\frac{y_\alpha^2 - x^2}{(x^2+y_\alpha^2)^2} + \frac{2}{(2\pi\alpha)^2}\cos[2k_F x]\left(\frac{\alpha}{r}\right)^{2K} \tag{3.38}$$

right) is Fermi liquid like (free fermion correlation decays as $1/x^2$). The $\cos[2k_F x]$ term differs from Fermi liquids where its decay remains $1/r^2$.

One can also obtain the pair correlation: from the bosonic representation the same way

$$O_{SU}(r) = \psi^\dagger(r)\psi^\dagger(r+1) \tag{3.39}$$

as the density-density correlation[40] and we only show results here: We see that the pair

$$\langle O_{SU}(r)O_{SU}(0)\rangle = \frac{1}{(\pi\alpha)^2}\left(\frac{\alpha}{r}\right)^{1/(2K)} \tag{3.40}$$

correlation also decays as power law. As mentioned before, for attractive interaction $K > 1$, and the pairing correlation decays slower.

[1] More detailed calculations can be found in Ref. [40]

One can also calculate the single-particle Green's function in the same manner. For right-movers: which is again a power law. The occupation factor $n(k)$ is the Fourier transform of

$$\begin{aligned} G_R(r) &= -\langle \psi_R(r)\psi_R^\dagger(0)\rangle \\ &= -\frac{e^{ik_F x}}{2\pi\alpha}\langle e^{i(\phi(r)-\theta(r))}e^{-i(\phi(0)-\theta(0))}\rangle \\ &= -\frac{e^{ik_F x}}{2\pi\alpha}e^{-[\frac{K+K^{-1}}{2}F_1(r)+F_2(r)]} \end{aligned} \tag{3.41}$$

the equal time Green's function and Here we see that instead of a discontinuity at k_F (which

$$n(k) \propto |k-k_F|^{\frac{K+K^{-1}}{2}-1} \tag{3.42}$$

is the case for Fermi liquids), we observe a power law. This is the siganture that fermionic quasiparticles do not exist in one dimension.

To summarize, we have discussed the behavior of single and two-partilce correlation functions in Luttinger liquids. In the next two chapters we will see how we numerically extract the Luttinger parameter K from the correlation functions and cross-validate the decaying exponents.

4.0 $N-$COMPONENT ONE DIMENSIONAL QUANTUM LIQUIDS WITHOUT SU(N) SYMMETRY

Having discussed the basics of our numerical methods-DMRG and the nature of the fermionic liquids (TLL) that we are interested in, we now move on to the first "key" focus in this thesis–n-component one dimensional quantum liquids.

Recently our experimental collaborators (Jeremy Levy's group at University of Pittsburgh) observed an interesting phenomena in their LAO/STO quantum wire devices: electrons from different bands come together and form pairs, even trions (electron from three bands come together and form bound states). In section 4.6 of this chapter we will present details of the experiemental data.

The nature of interactions between electrons in different bands in the LAO/STO material is unclear but we know that they are attractive[44]. To simulate the behavior of electrons for this material, we use mutli-component Hubbard-like model and assume onsite attractive interactions. We first analyze the two species case and later extend the discussions to three-species case. We aslo investigate models without SU(N) symmetry and comment on the stabilities of our results in each case.

In this chapter we first present the model Hamiltonian for our work, and discuss previous studies of this type of model. Next we discuss recent experimental progress which serves as a motivation for this work. Then we show some results at the low-filling fraction limit based on our numerical studies, which provides guidance for more detailed numerical analysis later in this chapter.

We separate our results into two categories: two-species and three-species case. In each of these category, we first investigate the SU(N) symmetric case[1]. Then we discuss the case

[1] I will discuss the meaning of SU(N) symmetry in each section.

in which the SU(N) symmetry being broken, which can be achieved by changing either the hopping amplitudes, the interaction strengths, or chemical potentials/magnetic fields. We plot out the phase diagrams for models with and without SU(N) symmetry, and discuss each phase in detail. We also comment on nature of the phase transitions.

Finally, we present the connections of our results with the recent experimental results of our collaborators in Prof. Jeremy Levy's group at University of Pittsburgh. We compare the experimental results to our numerical simulations, and find qualitative agreement. Then we analyze the transport properties of the n-component fermion liquids based on previous studies[45;46] and show that the conductance is quantized regardless of the nature of the liquids.

4.1 model Hamiltonian and SU(N) symmetry

The general form of the model we are considering for the n-component one-dimensional quantum liquids is the multiple-component Hubbard-like model: where $c_{i,\sigma}$ is the destruction

$$H = -\sum_{i,\sigma} t_\sigma \left(c^\dagger_{i,\sigma} c_{i+1,\sigma} + \text{h.c.} \right) - \sum_{i\sigma} (\mu_\sigma - 2t_\sigma) c^\dagger_{i,\sigma} c_{i,\sigma} + \sum_{i,\alpha>\beta} U_{\alpha\beta} n_{i,\alpha} n_{i,\beta}, \qquad (4.1)$$

operator for a with species (spin) σ on site i. The first term describes the kinectic term, i.e. the hopping of the fermions and t_σ is the hopping matrix element for fermion with species σ. The second term describes the on-site energy of the fermions depending on the chemical potential μ_σ[2]. We shifted μ_σ by half the bandwidth $2t_\sigma$ to align the bottom of the bands at zero energy. The last term is the on-site interaction term which describes the interactions between fermions of different species. α, β denotes species indices of two distinct fermion species.

The Hamiltonian shown above describes a general model for one-dimensional fermions with onsite interactions. In practice, the interactions between electrons in different bands

[2]Here we assume that the chemical potential is uniform (doesn't depend on lattice site) for each species.

are much more complex than point interactions, and this model can serve as a qualitative model for analyzing the experimental results in one-dimensional electron systems[3].

Here we comment on the SU(N) symmetry of the model Hamiltonian. If we ignore the chemical potential term[4], then the parameters are hopping amplitudes $t_1, t_2, \ldots$ and interaction strength $U_{\alpha,\beta}$. If all the hopping parameters are the same ($t_1 = t_2 = \ldots$) and the two-body interactions are of the same strength for any two pairs ($U_{\alpha,\beta} = U_{\gamma,\delta}$), then the Hamiltonian is invariant under the following transformations: where U are the unitary

$$\begin{pmatrix} c_{i,1} \\ c_{i,2} \\ \vdots \end{pmatrix} = U \begin{pmatrix} c_{i,1} \\ c_{i,2} \\ \vdots \end{pmatrix} \tag{4.2}$$

matrixes, which are generators of the Lie Algebra of the corresponding SU(N) group. As an example, for the 2 species case, U are the Pauli matrices and for three species U are the Gell-Mann matrices.

Having discussed the meaning of SU(N) symmetry, we can readily see that there are various ways to break the SU(N) symmetry. The first way is to make the hopping amplitudes different for different species, i.e. mass imbalance[5]. The second way is to introduce inhomogeneous interaction strength. We can also break the SU(N) symmetry by changing the chemical potential terms for different species.

In this chapter we focus on the 2-species and 3-species case, where in each case we present numerical results for the SU(N) symmetric case, and discuss the breaking of SU(N) symmetry in various ways and corresponding results.

[3]We will discuss in more detail about the validity of this model in section 4.7 in this chapter
[4]which is true in our numerical simulations as we run DMRG on fixed filling fractions.
[5]As the band mass is determined by the hopping amplitude via $m = 1/(2t)$

4.2 results in the low filling fraction limit

In this section we consider a finite lattice with just 2 or 3 electrons, we then calculate the full spectrum of such systems, from which we extract the ground state energy for the paired and trion state. Based on this we calculate the band mass for both pair and trion as a function of the interaction strength.

The Mathematica code for calculations in this section can be found in the appendix at the end of this chapter.

The basic idea is to consider a finite lattice of length L and the basis wavevectors are $\frac{2\pi}{L} \times \{0, 1, \ldots, L-1\}$. The functions above builds up the diagonal and offdiagonal elements for the Hamiltonian for both 2 species case and 3 species case. The script for calculating the pairing gap (2 species) is:

```
NN = 600;
E0 = Sort[Transpose[Eigensystem[pairgetH0[NN]]]][[1, 1]];
getDelta [NN_, U_] := Module[{es},
es = Sort[Transpose[Eigensystem[pairgetHH[NN, U]]]];
2*E0 - es[[1, 1]]
];
DeltaTable =
Table[{ii, getDelta[NN, ii]}, {ii,
 0., -0.5, -0.05}]; // AbsoluteTiming
```

where NN is the lattice size, $E0$ is the energy for 1 particle, es stands for the full spectrum for two particles with interaction strength U and $es[[1,1]]$ is the energy of the ground state. $2E0 - es[[1,1]]$ then represents the pairing gap (the energy difference between paired state and unpaired state).

The last line of code calculates a table of the pairing energy as a function of the interaction strength U, the resulting pairing gap are shown in Fig. 6, where the gap scales quadratic with interaction strength.

We can also calculate the band mass of pairs by calculating the energies for pairs with finite wavevectors and fit to $E(k) = E_0 + k^2/(2m)$ to get the effective band mass. The code is as follows:

```
kplist = Table[(ii - 1)*2*2. \[Pi]/NN, {ii, 1, 10}];
```

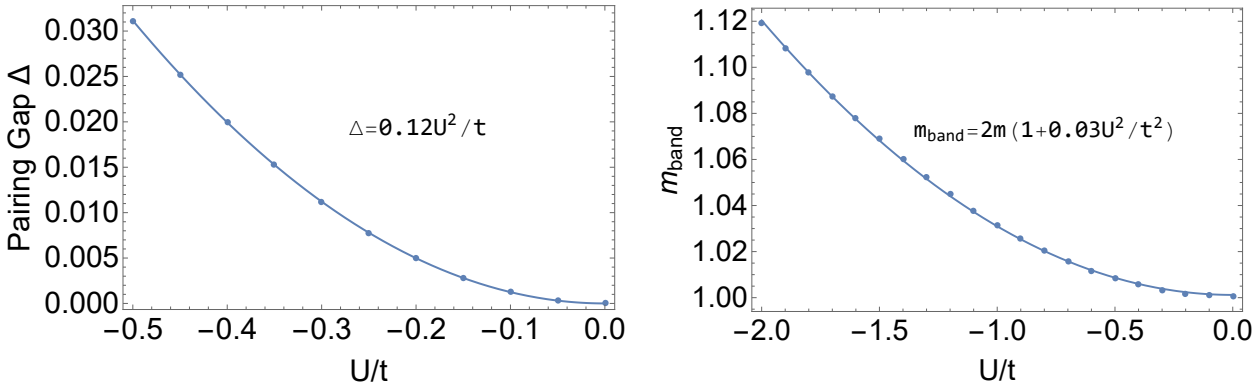

Figure 6: Pairing gap (left) and pair band mass (right) as a function of the interaction strength U. Dots are calculated data points and line is the fitted quadratic function.

```
    NN = 600;
    allTable = Table[
        U = U0;
        bmlist = Table[
        triE = Sort[Transpose[Eigensystem[pairgetHH2[NN, U, kp]]]][[1, 1]];
        {kp, triE}, {kp, kplist}];
    b0 = bmlist[[1, 2]];
    pbfit = FindFit[bmlist, a*x^2 + b0, {a}, x];
    {U0, 1/(2 a) /. pbfit}
  , {U0, 0, -2, -0.1}
  ]
```

where we calculate the ground state energy for a list of interaction strengths (from -2 to 0) and a list of momentum (from 0 to $2 \times 2\pi/NN \times 9$). For a fixed interaction strength we can calculate the band mass through the qudratic fitting mentioned above. Fig. 6 plots the band mass as a function of interaction strength U, showing a quadratic relation.

We can aslo calculate the pairing gap analytically. For the case of the Hubbard model, the most efficient way to find the binding energy is to look for zeros of the T-matrix. The equation for the zeros (at zero center of mass momentum) is where $\epsilon_k = 2t(1 - \cos(k))$ is

$$U^{-1} + \int_{-\pi}^{\pi} \frac{dk}{2\pi} \frac{1}{2\epsilon_k - \Delta} = 0, \tag{4.3}$$

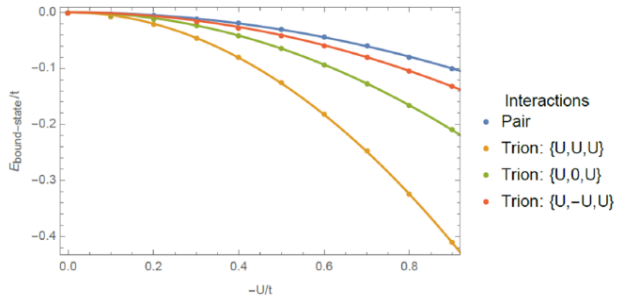

Figure 7: Comparison of Pair and Trion binding energies as a function of interaction strength. For the case of trions, we consider three cases: $\{U_{1,2}, U_{2,3}, U_{1,3}\} = \{U, U, U\}, \{U, 0, U\}, \{U, -U, U\}$ as labeled. The trion binding energies were computed on a 55-site Hubbard model lattice with periodic boundary conditions.

the kinetic energy of a fermion with momentum k. Solving this equation, we find For weak

$$\Delta = 4t - \sqrt{16t^2 + U^2} \tag{4.4}$$

attractive interactions $\Delta \approx -U^2/8t$, which is consistent with our numerical calculation.

For the case with three species there are no analytical solutions. We repeat the same numerical calculation process as with the 2 species case. The results of different interaction combinations are shown in Fig. 7 in comparison with the pair gap. From the plots we compare the trion and pair binding energy for several values of interaction parameters (as we do not know these ab initio). We observe that in all cases, for weak interactions the binding energy scales with U^2/t. For the case of weak symmetric attractive interactions ($\{U_1 2, U_2 3, U_1 3\} = \{U, U, U\}$) the trion binding energy is approximately four times stronger than the pair binding energy. Interestingly, we find that even if two components of the trion repel each other ($\{U_1 2, U_2 3, U_1 3\} = \{U, -U, U\}$), the trion still has a lower binding energy than the pair, indicating that there is a stable trion phase. We also calculate the band mass for trions by quadratic fitting as in the pair case, the calculated band mass for trion is $m_{trion} = 3m(1 + 0.14U^2/t^2)$ for $\{U, U, U\}$ type interactions.

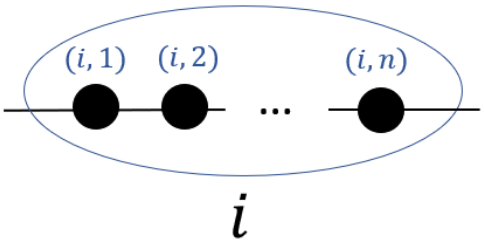

Figure 8: Schematic picture of the labeling of the particles on site i. Particles inside the same circle are located in the same lattice site.

4.3 Jordan-Wigner transformation and numerical setup

Throughout this chapter we use the TenPy2 package and dual_ising model and tri_ising model[6] for the 2 species and 3 species calculations, respectively. To connect from our Hamiltonian to the models used in the TenPy2 package, we need to perform Jordan-Wigner transformation (the package has a spin model where we have a lattice model). In this section we present the general Jordan-Wigner transformation for n-species fermions.

Suppose we have n species of particles. As shown in Fig. 8, we can label the sites on the chain by (i, j) such that the order of each site is $n * (i - 1) + j$. Here i stands for the lattice site labeling while j stands for the species labeling and $1 \leq j \leq n$.

We can do the following transformation:

$$c^{\dagger}_{i,j} = ((\prod_{i\prime=1}^{i-1}\prod_{j\prime=1}^{n}\sigma^{z}_{i\prime,j\prime})\prod_{k=1}^{j-1}\sigma^{z}_{i,k})\sigma^{+}_{i,j}$$
$$c_{i,j} = ((\prod_{i\prime=1}^{i-1}\prod_{j\prime=1}^{n}\sigma^{z}_{i\prime,j\prime})\prod_{k=1}^{j-1}\sigma^{z}_{i,k})\sigma^{-}_{i,j}$$

One can readily verify the anti-commutation relations of fermions, keeping in mind that Pauli matrix on different sites commute, while on the same site:

Having verified the commutation relations, we can start to apply the Jordan-Wigner

[6] which Prof. David Pekker and I wrote as a general extension of the dual_ising model

$$[\sigma^+, \sigma^z]_+ = 0$$
$$[\sigma^-, \sigma^z]_+ = 0$$
$$[\sigma^+, \sigma^-]_+ = I_2$$

transform to the desired terms in the Hamiltonian:

$$c^\dagger_{i,j} c_{i+1,j} = -\sigma^+_{i,j} \left(\prod_{j\prime=j+1}^{n} \sigma^z_{i,j\prime} \prod_{k=1}^{j-1} \sigma^z_{i+1,k} \right) \sigma^-_{i+1,j}$$
$$c^\dagger_{i+1,j} c_{i,j} = -\sigma^-_{i,j} \left(\prod_{j\prime=j+1}^{n} \sigma^z_{i,j\prime} \prod_{k=1}^{j-1} \sigma^z_{i+1,k} \right) \sigma^+_{i+1,j}$$
$$c^\dagger_{i,j} c_{i,j} = \sigma^+_{i,j} \sigma^-_{i,j} = \frac{I_2 + \sigma^z_{i,j}}{2}$$

We can also write out the correlation functions:

$$\langle c^\dagger_{i+r,j} c_{i,j} \rangle = -\sigma^-_{i,j} \left(\prod_{(i\prime,j\prime)=(i,j+1)}^{(i+r,j-1)} \sigma^z_{i\prime,j\prime} \right) \sigma^+_{i+r,j}$$
$$\langle c^\dagger_{i+r,k} c_{i+r,k} c^\dagger_{i,j} c_{i,j} \rangle = \frac{I_2 + \sigma^z_{i,j}}{2} \left(\prod_{(i\prime,j\prime)=(i,j+1)}^{(i+r,k-1)} I_2 \right) \frac{I_2 + \sigma^z_{i+r,k}}{2}$$
$$\langle c^\dagger_{i+r,j} c^\dagger_{i+r,k} c_{i,k} c_{i,j} \rangle = \sigma^-_{i,j} \left(\prod_{j\prime=j+1}^{k-1} \sigma^z_{i,j\prime} \right) \sigma^-_{i,k} \left(\prod_{(i\prime,k\prime)=(i,k+1)}^{(i+r,j-1)} I_2 \right) \sigma^+_{i+r,j} \left(\prod_{l\prime=j+1}^{k-1} \sigma^z_{i+r,l\prime} \right) \sigma^+_{i+r,k}$$

Here we have presented the general Jordan-Wigner transformation for n-species fermions. Later in the 2-species and 3-species section, we will show in details how to connect from the

lattice model parameters to the parameters used in the TenPy2 package.

4.4 2 species

4.4.1 numerical setup and expected phases

In this section we investigate on the 2 species case with Eq. (4.1), which we reproduces here: where the first line is the kinectic hopping term plus chemical potential term for fermion of

$$\begin{aligned} H = &- \sum_i t_1 \left(c^\dagger_{i,1} c_{i+1,1} + \text{h.c.} \right) - \sum_{i\sigma} (\mu_1 - 2t_1) n_{i,1} \\ &- \sum_i t_2 \left(c^\dagger_{i,2} c_{i+1,2} + \text{h.c.} \right) - \sum_{i\sigma} (\mu_2 - 2t_2) n_{i,2} \\ &+ \sum_i U_{1,2} n_{i,1} n_{i,2}, \end{aligned} \tag{4.5}$$

species 1, the second line represents the corresponding such terms for fermion of species 2. The last term denotes the onsite interaction term.

4.4.1.1 Numerical setup Recall the Jordan-Wigner transformation in the previous section, consider a chain with two species A/B ($n = 2$), We can model the system using four sites $ABAB$. Then the Hamiltonian is

Note that $\sigma^+\sigma^- + \sigma^-\sigma^+ = \frac{1}{2}(\sigma^x\sigma^x + \sigma^y\sigma^y)$, in the code we use the following line to represent the hopping term:

```
hop_list = [ ('pXZ','pXI',-t1/2), ('pYZ','pYI',-t1/2), ('pIX','pZX',-t2/2),
    ('pIY','pZY',-t2/2) ]
```

where pXZ stands for tensor product of σ^X and σ^Z matrices.

For the onsite interaction term, we use the following parameters:

```
Mpar = {
```

$$
\begin{aligned}
H =& t_1 * (\sigma^+ \otimes \sigma^z \otimes \sigma^- \otimes I_2 + \sigma^- \otimes \sigma^z \otimes \sigma^+ \otimes I_2) \\
&+ t_2 * (I_2 \otimes \sigma^+ \otimes \sigma^z \otimes \sigma^- + I_2 \otimes \sigma^- \otimes \sigma^z \otimes \sigma^+) \\
&+ (2t_1 - \mu) * (\frac{I_2 + \sigma^z}{2} \otimes I_2 \otimes I_2 \otimes I_2 + I_2 \otimes I_2 \otimes \frac{I_2 + \sigma^z}{2} \otimes I_2) \\
&+ (2t_2 - \mu) * (I_2 \otimes \frac{I_2 + \sigma^z}{2} \otimes I_2 \otimes I_2 + I_2 \otimes I_2 \otimes I_2 \otimes \frac{I_2 + \sigma^z}{2}) \\
&+ U * (\frac{I_2 + \sigma^z}{2} \otimes \frac{I_2 + \sigma^z}{2} \otimes I_2 \otimes I_2 + I_2 \otimes I_2 \otimes \frac{I_2 + \sigma^z}{2} \otimes \frac{I_2 + \sigma^z}{2})
\end{aligned} \tag{4.6}
$$

```
        'L': 1,
        'verbose': 1,
        'gzz': U,
        'hSz': -2 * t1 - U/2,
        'hTz': -2 * t2 - U/2,
        'constant offset': t1 + t2 + U/4,
        'extra_hoppings': [hop_list],
    }
```

where g_zz stands for the term $\sigma_z \otimes \sigma_z \otimes I_2 \otimes I_2$ and I_2 is the two-dimensional identity matrix.

Note here there is no definition of μ in our code. The reason is that we run the simulations at certain filling fractions n_1, n_2 with paricle number conservation. The procedure is as follows:

- Set parameters t_1, t_2 and $U_{1,2}$.
- Run the simulations at fixed filling fractions (n_1, n_2 constant) and obtain the ground state energy $E(n_1, n_2)$.
- Set parameters g_1, g_2 and for given chemical potential μ and magnetic field B, first calculate $E(\mu, B) = E(n_1, n_2) - (\mu + g_1 B)n_1 - (\mu + g_2 B)n_2$ for every filling fractions of n_1, n_2. Then choose the minimum energy and corresponding n_1, n_2.
- Given μ and B obtain the phase diagram determined by corresponding n_1, n_2 pairs.

In the previous procedure we only need to calculate $E(n_1, n_2)$ once for every pair of n_1, n_2. In our simulations we use filling fraction unit of $1/29$ and $n_{1,2}$ ranges from 0 to 1 in

steps of 1/29.

4.4.1.2 Expected phases

Before presenting the phase diagram, we first talk about the expected phases in our simulations and how to identify them.

- Vacuum phase.

  In this phase both species are empty: $n_1 = n_2 = 0$, this is a trivial phase.
- Fully fillied phase.

  In this phase both species are completely filled: $n_1 = n_2 = 1$.
- 1 Fermi Sea (1FS) phase.

  In this phase one of the species is either empty or completely filled while the other speces is partially filled. $n_1 = 0$ or $n_1 = 1$.
- Paired phase.

  In this phase the filling fractions for two species are the same and due to the attractive interactions they form pairs: $n_1 = n_2$.
- FFLO phase/ 2 Fermi seas (2FS) phase.

  In this phase $n_1 \neq n_2$.

4.4.2 attractive interaction case

In this subsection we present the phase diagram for $t_1 = t_2 = 1$. The interaction strength is $U_{1,2} = -3$, $g_1 = 1, g_2 = -1$. The filling fraction is in unit of 1/29. The phase diagram is shown in Fig. 9.

From the phase diagram we see that at low chemical potential and small magnetic field we get vacuum phase. As we increase the chemical potential, the total filling fraction will increase and ultimately reach to the Fully Filled phase at small magnetic field. As we increase the absolute value of magnetic field, the difference of filling fractions of species 1 and 2 also increases. As a result, we get FFLO/2FS phase next to the Paired phase, 1FS phase next to vacuum phase. Vacuum 2 here represents another kind of vacuum where one of the species

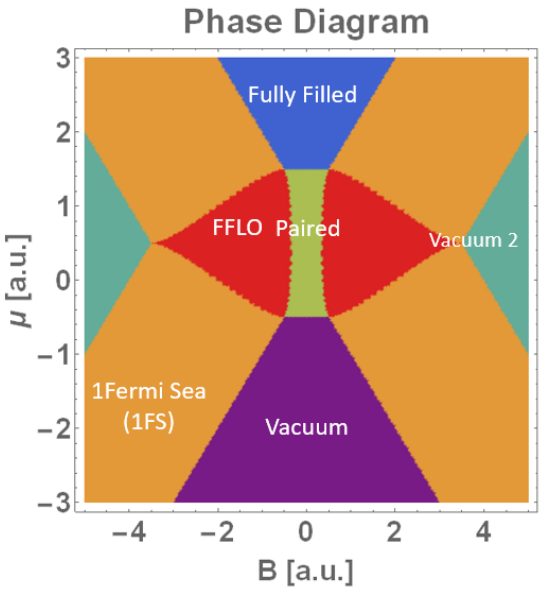

Figure 9: Phase diagram for 2 species fermion with attractive interaction $U_{1,2} = -3$. Vacuum 2 stands for $n_1 = 0, n_2 = 1$ or $n_1 = 1, n_2 = 0$. Here $g_1 = 1, g_2 = -1$.

is empty and the other is completely filled. Note here the SU(2) symmetric results can be obtained by taking a vertical cut along the $B = 0$ axis.

Having presented the phase diagram for $t_1 = t_2$, we now present the phase diagram for $t_1 \neq t_2$. This is called mass imbalance because hopping amplitude is related to the band mass of the fermions: $m_{\text{band}} = \frac{1}{2t}$.

In Fig. 10 we show the phase diagram at $t_2 = 2.1t_2$. Compared to the mass-balanced case in Fig. 9 we see that we obtain all the phases, but the phase diagram is skewed because of the mass imbalance. Here the parameters are $t_1 = 1, t_2 = 2.1, U_{1,2} = -3, g_1 = 1, g_2 = -1$.

4.4.3 repulsive interaction case

Having presented the phase diagram for the attractive interaction case, we now discuss what happens if the interaction is repulsive ($U_{1,2} > 0$).

It turns out that there exists an exact mapping from the attractive interaction to the repulsive interaction. The mapping is as follows:

The basic idea is to transform one of the fermion species into holes such that the hole is

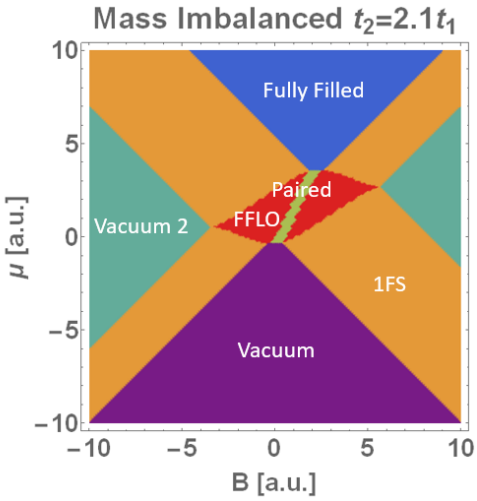

Figure 10: Phase diagram for 2 species fermion with attractive interaction $U_{1,2} = -3$ and mass imbalance $t_2 = 2.1t_1$. We get all the phases as shown in Fig. 9 but are skewed because of the mass imbalance.

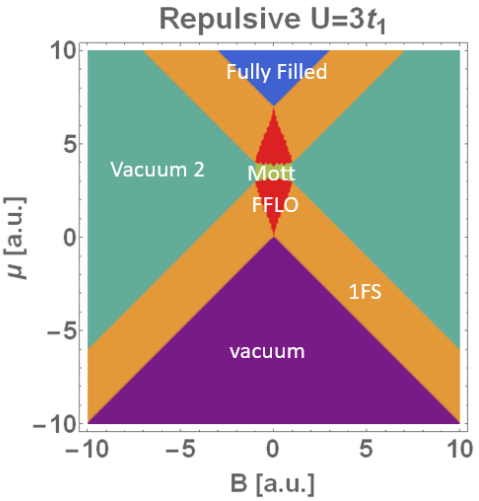

Figure 11: Phase diagram for 2 species fermion with repulsive interaction $U_{1,2} = 3$ and hopping parameters $t_1 = t_2 = 1$. Compared to Fig. 9 the phase diagram is rotated by 90 degree and the Mott phase is when $n_1 = n_2 = 1$, which corresponds to the pair phase after the transformation in Eq. (4.7).

$$
\begin{aligned}
c_{i,1}^{\dagger} \to (-1)^i c_{i,1}; c_{i,2} \to c_{i,2} \\
\mu \to 2t_2 - B - U_{1,2}/2 \\
B \to 2t_2 - \mu + U/2 \\
E \to E + t_1 + t_2 - \mu - B
\end{aligned} \tag{4.7}
$$

now attractive to the other fermion. The phase diagram for the repulsive case with $U_{1,2} = 2t$ is shown in Fig. **??**. Compared to the phase diagram with attractive interaction Fig. 9, we see that the phase diagram for repulsive case is rotated by 90 degree and shifted, which is consistent with the transformation in Eq. (4.7). The Mott phase represents $n_1 + n_2 = 1$, which corresponds to the pair phase $n_1 = n_2$ after the transformation (the transformation makes $n_1 \to 1 - n_1$).

4.4.3.1 correlators in FFLO phase and paired phase

Having presented the phase diagrams for the 2 species model, we now discuss the FFLO (2FS) phase in detail. In this phase the filling fraction for two species are different and the interaction is attractive to promote pairing. We first measure the central charge and obtain 2, which means there are two gapless mode in such phase. Because of the unmatched Fermi sea, unlike the paired phase where there exists a gap for adding one particle, there is no such gap in the FFLO phase. The single correlators and pairing correlators are plotted in Fig. 12, where we obtain algebraicaly decay for both correlators.

So far the results are consistent with 2 independent Fermi Seas, where the single correlator decay algebraically and pair correlator also decay algebraically because it is simply the product of two single correlators. Because of the attractive interaction, the decay exponent for the pair correlator is smaller than the sum of the decay exponents of two single correlators. In this regard, one might view this FFLO phase as 2 Fermi Sea (2FS) phase.

In the paired phase the filling fractions for both species are the same $n_1 = n_2$. Due to

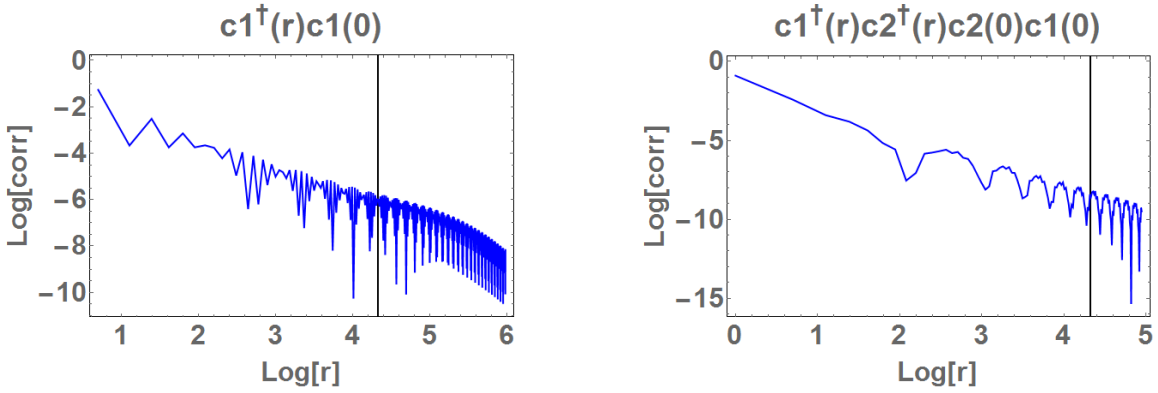

Figure 12: Single correlator (left) and pair correlator (right) in the FFLO phase. Data is taken at $t_1 = t_2 = 1, n_1 = 6/13, n_2 = 5/13, U = -3$. Black vertical line represents the correlation length.

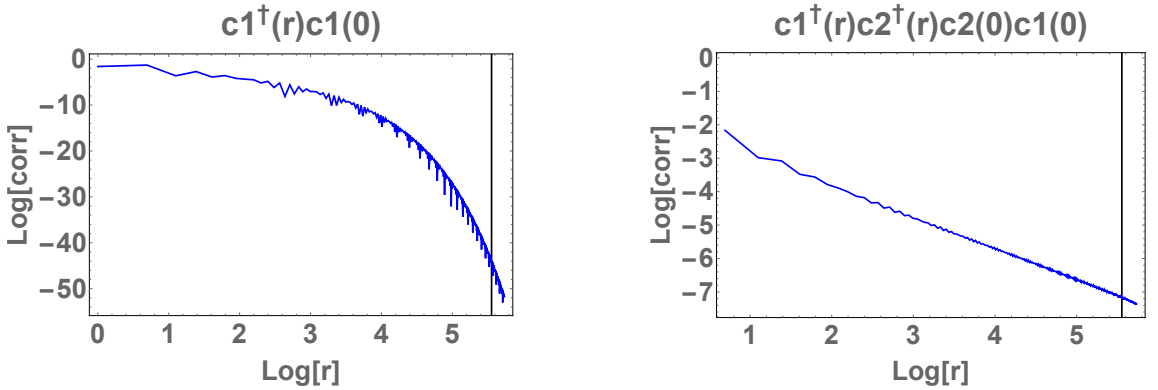

Figure 13: Single correlator (left) and pair correlator (right) in the paired phase. Data is taken at $t_1 = t_2 = 1, n_1 = n_2 = 6/13, U = -3$. Black vertical line represents correlation length.

the attractive interaction, the two types of fermions are attracted to each other and form pairs. In this phase the central charge is 1, which means there is only one gapless mode in such phase. In Fig. 13 we plot out the single and pair correlators in such phase. We observe exponential decay for the single correlator and algebraically decay for the pair correlator, which means two-particle excitation is gapless while adding a single type of particle requires a finite amount of energy.

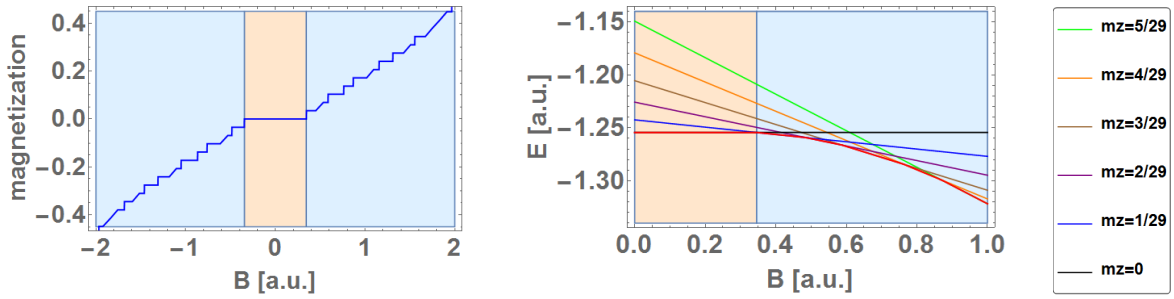

Figure 14: (left) Magnetization as a function of B field. The zig-zag structure is an artifact of the finite filling fraction. (right) Energy of various mz sectors as a function of B field. The ground state energy is plotted in red.

4.4.4 pair to FFLO transition

After identifying the various phases, we now investigate the phase transition from fully paired phase to FFLO phase. Fig. 14 shows the magnetization as a function of magnetic filed B. We see that the magnetization changes linearly along the transition from FP and $FFLO$ phase. Fig.4b shows energy v.s. B plot for various mz sectors. From these two plots we conclude that the transition is a cross-over.

4.4.5 strong repulsion and mass imbalance

In this subsection we investigate the case with strong mass imbalance. Specifically we focus on the filling ratio of $n_1 = n_2 = 5/12$ and interaction strength U ranges from -1 to 4 in steps of 0.25. The mass imbalance is defined as $j = t_1/t_2$, ranges from 0.01 to 0.2 in steps of 0.01. We perform iDMRG on bond dimensions of 40, 80, 160, 300 and extrapolate the central charge, shown in Fig. 15.

From Fig. 15 we observe that for negative U we get central charge 1. Based on the correlation functions measurement we observe exponential decay for single correlator and power law decay for pair correlator. This indicates that these two species have been paired up and this is the pair phase.

At large postive $U > 2$ and small $j < 0.1$ (large mass-imbalance) we observe a region with arbitrary central charge. Further investigation in this region shows that the DMRG

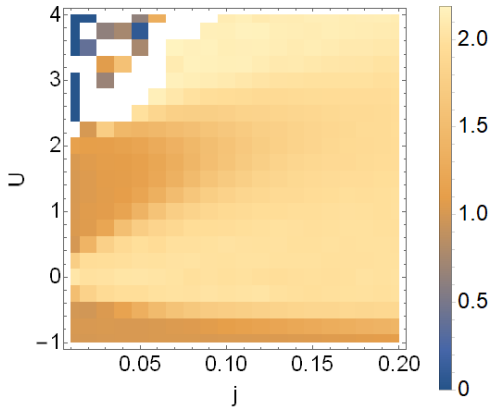

Figure 15: Phase (central charge) diagram of a mass-imbalanced mixtures with $n_1 = n_2 = 5/12$. $j = t_1/t_2$ measures the mass imbalance and U is the interaction between the two species. The top-left corner are regions where the code fails to converge, leading to arbitrary central charge numbers.

fails to converge in this region and the correlation length we get from the DMRG is unusually small. This indicates a region of phase separation.

At small positive U and small $j < 0.1$ we see a region of central 1. From the correlation mesurement we observe exponential decay for both the single correlators as well as the pair correlator. We speculate that this phase is spin density wave (SDW), but still needs further investigation to confirm this.

At large j and positive U we observe a region with central charge 2. The correlation measurement shows that all the correlators decay algebraically, indicating there is no gap in either the spin sector or the charge sector. This is the $2TLL$ phase where the two species with repulsive interactions act independently.

Compared with Ref.[47], the Pair phase, SDW phase, 2TLL and Phase Separation are observed. However, we fail to observe the crystal phases mentioned in Ref.[47].

4.5 3 species

In this section we investigate on the 3 species case of Eq. (4.1), which we reproduces here:

where the first three lines are the kinetic terms plus chemical potential terms for these

$$
\begin{aligned}
H = &- \sum_i t_1 \left(c_{i,1}^\dagger c_{i+1,1} + \text{h.c.} \right) - \sum_{i\sigma} (\mu_1 - 2t_1) n_{i,1} \\
&- \sum_i t_2 \left(c_{i,2}^\dagger c_{i+1,2} + \text{h.c.} \right) - \sum_{i\sigma} (\mu_2 - 2t_2) n_{i,2} \\
&- \sum_i t_3 \left(c_{i,3}^\dagger c_{i+1,3} + \text{h.c.} \right) - \sum_{i\sigma} (\mu_3 - 2t_3) n_{i,3} \\
&+ \sum_i \left(U_{1,2} n_{i,1} n_{i,2} + U_{1,3} n_{i,1} n_{i,3} + U_{2,3} n_{i,2} n_{i,3} \right), \qquad (4.8)
\end{aligned}
$$

three species of fermions. The last line denotes the onsite 2-body interaction terms among these three species.

4.5.0.1 Numerical setup

We use DMRG algorithm and the TenPy2 package from Professor Roger Mong for the numerical calculations. Similar to the 2-species case, the sample code using the TenPy2 package is as follows:

```
onsite_list = [ ('pIII',t1 + t2 + t3 + U12/4 + U13/4 + U23/4),
              ('pZII', -t1 - U12/4 - U13/4),
              ('pIZI', -t2 - U12/4 - U23/4),
              ('pIIZ', -t3 - U13/4 - U23/4),
              ('pZZI', U12/4),
              ('pZIZ', U13/4),
              ('pIZZ', U23/4)]
    hop_list = [ ('pXZZ','pXII',-t1/2), ('pYZZ','pYII',-t1/2),
        ('pIXZ','pZXI',-t2/2), ('pIYZ','pZYI',-t2/2), ('pIIX','pZZX',-t3/2),
        ('pIIY','pZZY',-t3/2)]
    Mpar = {
           'L': 1,
           'verbose': 1,
           'extra_onsite': [onsite_list],
           'extra_hoppings': [hop_list]
    }
```

The numerical running procedure is also similar to the 2-species case:

- Set parameters t_1, t_2, t_3 and $U_{1,2}, U_{1,3}, U_{2,3}$.

- Run the simulations at fixed filling fractions (n_1, n_2, n_3 constant) and obtain the ground state energy $E(n_1, n_2, n_3)$.
- Set parameters g_1, g_2, g_3 and for given chemical potential μ and magnetic field B, first calculate $E(\mu, B) = E(n_1, n_2, n_3) - (\mu + g_1 B)n_1 - (\mu + g_2 B)n_2 - (\mu + g_3 B)n_3$ for every filling fractions of n_1, n_2, n_3. Then choose the minimum energy and corresponding n_1, n_2, n_3.
- Given μ and B obtain the phase diagram determined by corresponding n_1, n_2, n_3 pairs.

In the previous procedure we only need to calculate $E(n_1, n_2, n_3)$ once for every pair of n_1, n_2, n_3. In our simulations we use filling fraction unit of $1/17$ and $n_{1,2,3}$ ranges from 0 to 1 in steps of $1/17$.

4.5.0.2 Expected phases Before presenting the phase diagram, we first talk about the expected phases in our simulations and how to identify them.

- Vacuum phase.

  In this phase all three species are empty: $n_1 = n_2 = n_3 = 0$, this is a trivial phase.
- Fully fillied phase.

  In this phase all species are completely filled: $n_1 = n_2 = n_3 = 1$.
- 1 Fermi Sea (1FS) phase.

  In this phase two of the species are either empty or completely filled while the third species is partially filled. e.g. $n_1 = n_2 = 0$ or $n_1 = 0, n_2 = 1$.
- Paired phase.

  In this phase the filling fractions for two of the three species are the same while the third species is either empty or fully filled. e.g. $n_1 = n_2$, $n_3 = 0/1$.
- FFLO phase/ 2 Fermi seas (2FS) phase.

  In this phase one of the species is either empty or fully filled while the other two species are partially filled with different filling fractions. e.g. $n_1 \neq n_2$, $n_3 = 0/1$.
- trion phase.

  In this phase the filling fractions for all three species are the same. e.g. $n_1 = n_2 = n_3$.
- 1FS+1Pair (1Fermi Sea plus 1 pair) phase.

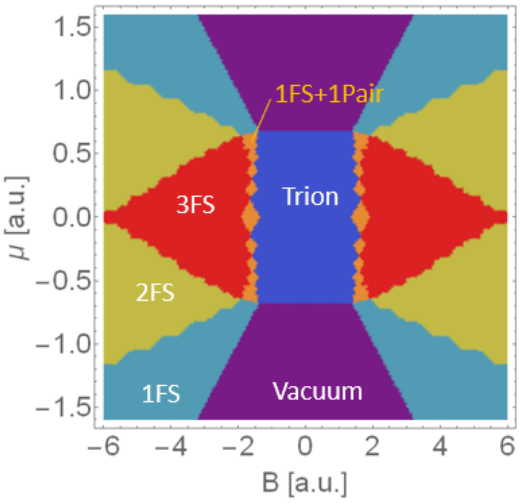

Figure 16: Phase diagram for 3 species fermion: $t_{1,2,3} = 1, U_{1,2} = U_{1,3} = U_{2,3} = -2$. Data is calculated using fill fraction step of $1/17$. $g_1 = 0.5, g_2 = 0, g_3 = -0.5$.

In this phase all three species are partially filled and two of them have the same filling fraction. i.e. $n_1 = n_2$, $n_1 \neq n_3$.

- 3FS (3 Fermi Sea)

  In this phase all three species are partially filled with different filling fractions. i.e. $n_1 \neq n_2$, $n_1 \neq n_3$, $n_2 \neq n_3$.

4.5.1 isotropic interaction case

We first present the phase diagram for the isotropic interaction Hamiltonian and the parameters are $t_1 = t_2 = t_3 = 1$, $U_{1,2} = U_{1,3} = U_{2,3} = -2$. The phase diagram is shown in Fig. 16.

In the phase diagram again at low chemical potential and small magnetic field we obtain the vacuum phase. At larger magnetic field, we get 1FS phase neighboring the vacuum phase. As we increase the chemical potential, we start to get more filling fractions for all species. At small magnetic field, we get trion phase and fully filled phase. At larger magnetic field, we observe 1FS+1Pair phase neighboring the trion phase and 3FS phase. The wiggled lines are artifacts of the finite filling fractions of our numerical simulations.

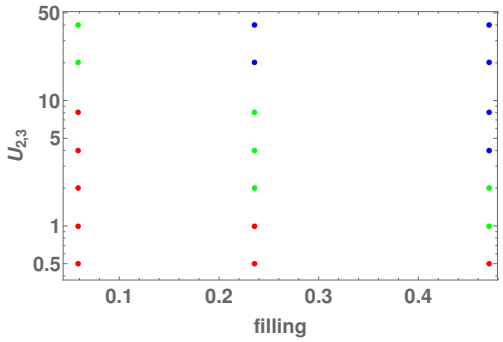

Figure 17: Phase diagram of three species case as filling and $U_{2,3}$ varies with $U_{1,2} = U_{1,3} = -2$ and $t_1 = t_2 = t_3 = 1$. Red points stand for trion phase, blue points stand for 3-LL phase and green points are in between (undetermined).

4.5.2 trion with anisotropic interactions

In the 3 species case there are two ways to break the SU(3) symmetry other than the chemical potential/magnetic field. The first is to introduce mass imbalance. As mentioned in the two-species case, the effects of mass-imbalance is quite complex so we omit it here. The other way to break SU(3) symmetry is to introduce unisotropic interactions.

In order to reduce the parameter space, we keep $U_{1,2} = U_{1,3} = -2t$ while varying $U_{2,3}$. We also focus on three filling fractions for these three species $n_1 = n_2 = n_3 = (1, 4, 8)/17$. In this study we want to observe the robustness of trion versus a repulsive $U_{2,3}$. The bond dimension in this study goes up to 600 and both central charge calculation and correlation functions are investigated to determine the phase of the ground state.

As shown in Fig. 17, we use different color to represent different phases. The red dots represent trion phase, blue dots represent 3TLL phase and green dots represent undetermined phase. At low filling ($n = 1/17$), we see that trion phase persists up to repulsive interaction $U_{2,3} = 10$. As we increase the filling fractions, the repulsive interaction needed to break trions decreases. For filling fraction of $n = 4/17$, trion survives up to $U_{2,3} = 1$ while trion only survives up to $U_{2,3} = 0.5$ for filling fraction of $n = 8/17$.

From the discussion above see that trions are stable against repulsive $U_{2,3}$ at small filling fractions and tend to be less stable at higher filling fractions. However, even near half-filling, trions can be achieved with one of the interactions being negative. This shows that trion

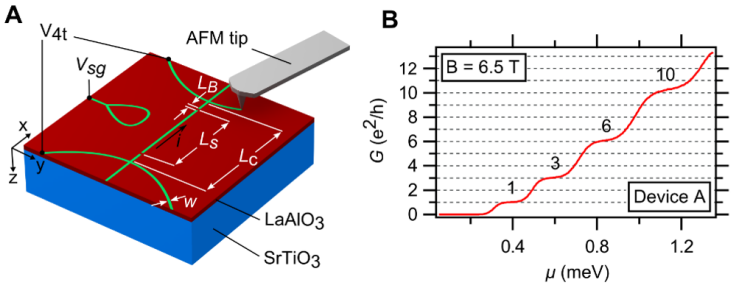

Figure 18: (A) Depiction of the sketched waveguide. Green lines indicate conductive paths at the LaAlO3/SrTiO3 interface. Device dimensions are indicated: barrier width L_B, barrier separation L_S, total length of the channel between the voltage sensing leads L_C, and nanowire width as measured at room temperature typically w $\approx$ 10 nm. (B) Conductance G through Device A at $T = 50mK$ and $B = 6.5T$. A series of quantized conductance steps appears at $(1, 3, 6, 10,)e^2/h$.

can be obtained in a wide range of interactions and are quite stable.

4.6 connections with LAO/STO experiments

In this section we present the connections between this work and the LAO/STO experiments performed by our collaborators. We first show the experimental setup and their key results. Then we show how we simulate the experimental system using our model Hamiltonian and compare the results to the experiental data. We also analyze the stability of trion phase by calculating the band mass of the trion. Finally, we discuss the transport properties.

4.6.1 experimental setup and results

The experiments was done on a thin film of $LaAlO_3$ [44] where an electron waveguide (Fig. 18) is created using "sketched" approach. The conductance of the waveguide depends principally on the chemical potential μ and magnetic field B. The chemical potential is controlled by a local side gate votage V_{sg} and the magnetic field is external magnetic field which is perpendicular to the film.

For typical quantum point contacts we expect the conductance to be a linear sequence: $2\times(1,2,3\ldots)e^2/h$, where the factor 2 relects the spin degeneracy. In the presence of magnetic field, the elctron states are Zeeman split and resolve into sequences of $(1,2,3\ldots)e^2/h$. In the experiment the conductance was measured as a function of V_{sg} (chemical potential) and magnetic field B. As shown in Fig. 18, however, for certain values of magnetic field, the conductance steps follow the sequence $(1,3,6,10\ldots)e^2/h$, or $G_n = n(n+1)/2e^2/h$.

In order to better understand the origin of this sequence, it is helpful to examine the transconductance $dG/d\mu$ and plot it as an intensity map as a function of B and μ. Transconductance maps for one of device is shown in Fig. 19. A peak in the transconductance demarcates the chemical potential at which a new sub-band emerges; these chemical potentials occur at the minima of each subband, and as such we refer to them as subband bottoms (SBB). The peaks generally shift upward as the magnitude of the magnetic field is increased, sometimes bunching up and then again spreading apart. Near a special value of the magnetic field, the peaks merge to produce the Pascal series of conductance plateaus as a function of chemical potential.

4.6.2 numerical models and results

4.6.2.1 single-particle model To model the waveguide we start with a single-particle picture where electrons are confined by the waveguide in the vertical and lateral directions and an external magnetic field affects the electron via Zeeman and orbital effects. The waveguide Hamiltonian can be written as: where m_x^*, m_y^*, m_z^* are the effective masses along

$$H = \frac{(p_x - eB_z y)^2}{2m_x^*} + \frac{p_y^2}{2m_y^*} + \frac{p_z^2}{2m_z^*} + \frac{m_y^*\omega_y^2}{2}y^2 + \frac{m_z^*\omega_z^2}{2}z^2 - g\mu_B B_z s, \tag{4.9}$$

the x, y, z directions, ω_y, ω_z are the frequencies associated with parabolic confinements in the lateral (y) direction and half-parabolic confinement in the vertical ($z > 0$) direction, rspectively. Eigenenergies corresponding to the SSBs (subband bottoms) are given by: where

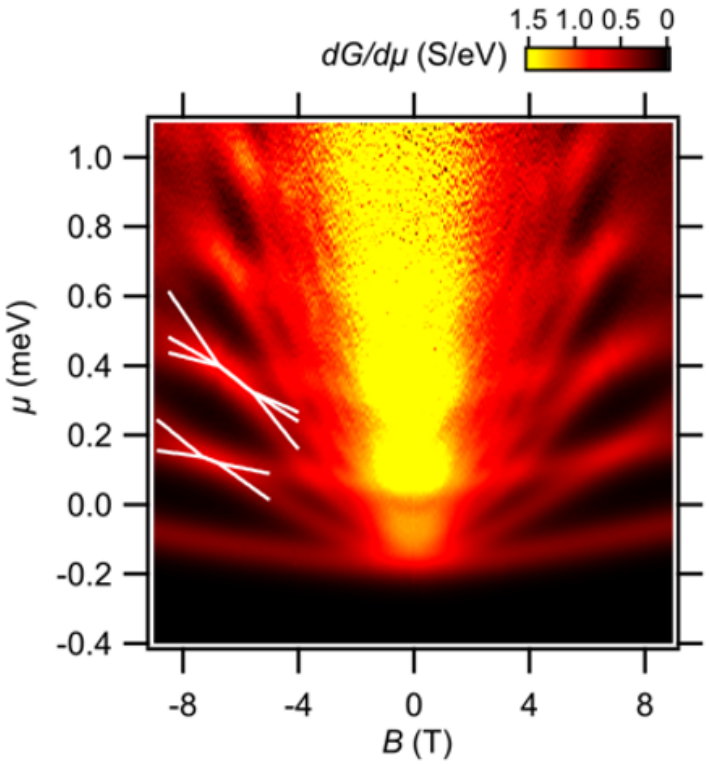

Figure 19: Transconductance data for one device. White lines are fits of the peak locations for the $n = 2$ and $n = 3$ Pascal states and correspond to contribution of additional subbands in the transconductance data.

$$E_{n_z,n_y,s} = \hbar\Omega(n_y + 1/2) + \hbar\omega_z\left((2n_z + 1) + 1/2\right) - g\mu_B B_z s, \tag{4.10}$$

n_z, n_y, s are the orbital quantum numbers and spin quantum number. $\Omega = \sqrt{\omega_y^2 + \omega_c^2}$, $\omega_c = eB_z/\sqrt{m_x^* m_y^*}$ is the magnetic field-dependent frequency.

To obtain the equispaced energies observed in the quantized conductance steps we need the "Pascal condition": $\Omega = 4\omega_z = 2g\mu_B B_z/\hbar$, which requires fine tuning of the magnetic field as well as the geometry of the waveguide. However, the Pascal series has been observed in multiple devices and single-particle picture cannot explain the locking begavior observed in the experiments. Therefore we need to include the electron-electron interactions.

4.6.2.2 Effective 1D lattice model with interactions

Our analysis here is not intended to be ab-initio. In constructing our model, we make a number of simplifying assumptions about the nature of the attractive electron-electron interaction, and therefore our numerical results should be seen as qualitative and not quantitative. Direct comparison to experimental data would require putting some complexity back into the modellike long-ranged interactionsas well as fitting of the model parameters. Rather, we aim to get the correct set of phases and the rough shape of the phase boundaries to justify our interpretation of the experimental data.

Our analysis begins with a derivation of a multi-band 1D continuous model starting from our 3D continuous Hamiltonian. We then introduce interactions and specify simplifying assumptions to ultimately arrive at an effective 1D lattice model. Importantly, the lattice spacing, and hence U and t, in this model do not correspond to the actual microscopic values associated with LaAlO3/SrTiO3 but are rather effective parameters.

We start with Eq. (4.9), in which we define the 3D continuous model of the electron waveguide without an interaction term.

Next, we solve this model to find the one-electron eigenstates (i.e. the waveguide modes):

where index $\alpha = \{n_y, n_z, s\}$ combines the quantum numbers. We can then rewrite Hamil-

$$\Phi_{\alpha,k_x}(x,y,z) = e^{ik_x x}\Phi_{\alpha,k_x}(y,z), \tag{4.11}$$

tonian as a one-dimensional, multi-band model: where $m'_x = m^*_x\Omega^2/\omega_y^2$ is the effective mass

$$H = \sum_{\alpha,k_x}\left(E_\alpha + \frac{\hbar^2 k_x^2}{2m'_x}\right)c^\dagger_{\alpha,k_x}c_{\alpha,k_x}, \tag{4.12}$$

and the energy E_α follows Eq. (4.10).

Next, we introduce the electron-electron interactions. As we do not know the microscopic origin, we begin with the most general form of the interactions:

$$H_{int} = \sum_{\alpha,\beta,\gamma,\delta,k_1,k_2,k_3,k_4}\tilde{U}_{\alpha,\beta,\gamma,\delta}(k_1,k_2,k_3,k_4)c^\dagger_{\alpha,k_1}c^\dagger_{\beta,k_2}c_{\gamma,k_3}c_{\delta,k_4}. \tag{4.13}$$

At this point, we make some simplifying assumptions. First, we assume the system is translationally invariant and hence $\tilde{U}_{\alpha,\beta,\gamma,\delta}(k_1,k_2,k_3,k_4) \propto \delta(k_1+k_2-k_3-k_4)$. Second we ignore sub-band mixing $\tilde{U}_{\alpha,\beta,\gamma,\delta}(k_1,k_2,k_3,k_4) \propto \delta_{\alpha,\delta}\delta_{\beta,\gamma}$. Finally, while $\tilde{U}$ is generally a function of momentum, we assume that for the range of momenta that we are interested in $\tilde{U}$ is momentum independent. Under these assumptions, H_{int} greatly simplifies:

To perform numerical simulations we need to map the model onto an effective lattice model. Introducing an effective lattice length-scale a (or equivalently momentum cutoff $2\pi/a$) we obtain the lattice Hamiltonian: where the first term denotes the chemical potential term, the second term denotes the hopping and the last term denotes the effective onsite interactions. Compared to the general Hamiltonian in Eq. (4.1), we see that these two

$$H_{int} = \sum_{\alpha,\beta,k_1,k_2,k_3} \tilde{U}_{\alpha,\beta} c^\dagger_{\alpha,k_1} c^\dagger_{\beta,k_2} c_{\beta,k_3} c_{\alpha,k_1+k_2-k_3}. \quad (4.14)$$

$$H = \sum_{\alpha,j}(-\mu + E_\alpha - 2t_\alpha)c^\dagger_{\alpha,j}c_{\alpha,j} - \sum_{\alpha,j}(t_\alpha c^\dagger_{\alpha,j}c_{\alpha,j+1} + h.c.) + \sum_{\alpha,\beta,j} U_{\alpha,\beta} c^\dagger_{\alpha,j} c^\dagger_{\beta,j} c_{\beta,j} c_{\alpha,j}, \quad (4.15)$$

Hamiltonian are effectively the same.

4.6.2.3 numerical results The DMRG phase diagram in the vicinity of the $n = 2$ Pascal liquid is shown in Fig. 20A. Distinct phases are illustrated by regions of solid color and identified with text in each representative region. In addition to a vacuum phase (V; no electrons) and a one-Fermi-sea phase (F; one mode is occupied), we also find a two-Fermi sea phase (2F; both modes occupied) and an electron-pair phase (P) in which single electron excitations are gapped out and both modes have equal electron density. Boundaries between phases are of two types: phase boundaries in which the number of fermion modes is unchanged (indicated by dashed lines) and phase boundaries in which the number of fermion modes changes (indicated by solid white lines). The solid white line boundaries correspond to peaks in the transconductance, which are also highlighted in the experimental data in Fig. 20A. Experimentally, DC measurements cannot distinguish between phases that have the same conductance (e.g., P and 2F). We expect the pairing strength to scale as U^2/t, where U is the attractive interaction strength and $t = {}^2/ma^2$ is the bandwidth (where m is the band mass and a is the lattice spacing). This energy scale determines the range of magnetic field over which electrons are locked together.

Extending this calculation to three electron modes with attractive interactions maps out the $n = 3$ Pascal liquid and associated phases (Fig. 20B). The $n = 3$ Pascal liquid

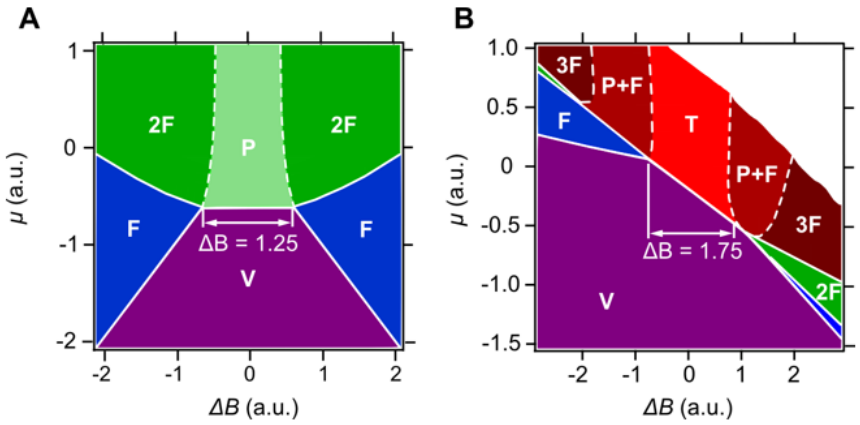

Figure 20: DMRG phase diagrams calculated for two (A) and three (B) fermions with attractive interactions in one dimension. Abbreviations for various phases: mF: m distinct fermi surfaces, P: paired phase, T: trion phase, V: vacuum, A+B: phase composed of A and B. The black numbers on the plots indicate the strength of the locking for the pair (A) and trion (B) phases. Similar to what is observed in fits of the experimental data, the trion phase is locked over a larger range of magnetic field values.

is comprised of trions, bound states of three electrons (T) that form a one-dimensional degenerate quantum liquid. In this phase, all one- and two-electron excitations are gapped out, but three-electron excitations are gapless. Adjacent to the trion phase are two related 3-electron phases: one in which a single electron breaks free, leaving behind a pair (F+P), and another in which all three fermions are independent (3F). The three phases are distinguished by the number of gapless modes but all contribute three conductance quanta to the DC conductivity. Other phases exist at lower chemical potentials (P, 2F, F, V), rounding out the entire phase diagram. We explore the stability of the phase diagram as we deviate from the Pascal Condition and find that the trion phase is remarkably stable, as compared to the competing phases (see next section).

4.6.3 transport properties analysis

In this section we analyze the transport properties of TLL when connected to normal leads. This section follows from Ref.[45] that use Green's function to calculate the conductivity for

Luttinger liquid[7].

We use a simple model such that K for the Luttinger liquid changes stepwise from leads value K_L ($x > |L/2|$) to K_W in the wire. The electric field is assumed to be 0 outside the wire but can take any value in the wire.

The charge current can be written as: where $\sigma_\omega(x, x')$ is the non-local ac conductivity. In

$$I(x,t) = \int_{-L/2}^{L/2} dx' \int \frac{\omega}{2\pi} \sigma_\omega(x,x') E_\omega(x') \tag{4.16}$$

the Matsubara representation, $\sigma_\omega(x, x')$ can be expressed via the current-current correlation function by the usual Kubo formula

$$\sigma_\omega(x,x') = \frac{ie^2}{\hbar\omega} \int_0^\beta d\tau < T_\tau^* j(x,\tau) j(x',0) > e^{-i\bar{\omega}\tau}|_{\bar{\omega}=-i\omega+\epsilon} \tag{4.17}$$

In the Bosonized form, the current is given by $j = -i\partial_\tau\phi/\sqrt{\pi}$ and we get where $G_{\bar{\omega}}$ is

$$\sigma_\omega(x,x') = \frac{e^2}{\hbar} \frac{i\bar{\omega}^2}{\pi\omega} G^0_{\bar{\omega}}(x,x')|_{\bar{\omega}=-i\omega+\epsilon} \tag{4.18}$$

$$G_{\bar{\omega}}(x,x') = \int_0^\beta d\tau < T_\tau^* \phi(x,\tau)\phi(x',0) > e^{-i\bar{\omega}\tau} \tag{4.19}$$

the propagator of the boson field. The general form of action for spin/charge part is

Expand the $\cos 2\sqrt{2}\phi$ term as $1 - 4\phi^2$, we can readily get the equation for the propagator (assume $v(x) = v$):

For convenience purpose, we define: and similarly for $\Omega_W = \sqrt{\bar{\omega}^2 + 8|g|vK_W}$.

[7] Ref. [46] also gives the same result

$$S = \frac{1}{2\pi}\int dx \int_0^\beta d\tau [\frac{1}{K(x)}(\frac{1}{v(x)}(\partial_\tau \phi(x,\tau))^2 + v(x)(\partial_x \phi(x,\tau))^2) + g\cos 2\sqrt{2}\phi] \tag{4.20}$$

$$(-\partial_x(\frac{v}{K(x)}\partial_x) + \frac{\bar{\omega}^2}{vK(x)} + 8|g|)G_{\bar{\omega}}(x,x') = \delta(x,x') \tag{4.21}$$

$$\begin{aligned}\Omega_L &= \sqrt{\bar{\omega}^2 + 8|g|vK_L} \\ &= \begin{cases} \sqrt{8|g|vK_L - \omega^2} & \text{for } \omega < \sqrt{8|g|vK_L} \\ -i\sqrt{\omega^2 - 8|g|vK_L} & \text{otherwise} \end{cases}\end{aligned} \tag{4.22}$$

Note $\bar{\omega} = -i\omega + \epsilon$ and $G_{\bar{\omega}}(\infty, x') = 0$. The Green's function thus has the following form:

$$G_{\bar{\omega}}(x,x') = \begin{cases} Ae^{\frac{\Omega_L}{v}x} & \text{for } x \le -L/2 \\ Be^{\frac{\Omega_W}{v}x} + Ce^{-\frac{\Omega_W}{v}x} & \text{for } -L/2 < x \le x' \\ Ce^{\frac{\Omega_W}{v}x} + De^{-\frac{\Omega_W}{v}x} & \text{for } x' < x \le L/2 \\ Fe^{-\frac{\Omega_L}{v}x} & \text{for } x > L/2 \end{cases} \tag{4.23}$$

For the boundary conditions:

1. $G_{\bar{\omega}}(x,x')$ is continuous everywhere.

2. $-\frac{v}{K(x)}G_{\bar{\omega}(x,x')}$ is continuous everywhere and has a jump at $x = x'$.

We can match the boundary conditions at $x = -L/2$, $x = x'$ and $x = L/2$: where

$$\begin{aligned}
A' &= \frac{1}{c_1}B + c_1 C \\
c_2 A' &= \frac{1}{c_1}B - c_1 C \\
c_3 B + \frac{1}{c_3}C &= c_3 D + \frac{1}{c_3}E \\
c_3 B - \frac{1}{c_3}C &= c_3 D - \frac{1}{c_3}E + \frac{K_W}{\Omega_W} \\
c_1 D + \frac{1}{c_1}E &= F' \\
-c_1 D - \frac{1}{c_1}E &= c_2 F'
\end{aligned} \tag{4.24}$$

$c_1 = e^{\frac{\Omega_W L}{2v}}$, $c_2 = \frac{K_W \Omega_L}{K_L \Omega_W}$, $c_3 = e^{\frac{\Omega_W}{v}x'}$ and $A' = Ae^{-\frac{\Omega_L L}{2v}}$, $F' = Fe^{-\frac{\Omega_L L}{2v}}$.

We can solve the equations and notice that $F' = G_{\bar{\omega}}(L/2, x')$ and $A' = G_{\bar{\omega}}(-L/2, x')$, respectively. After solving these equations, we get

$$F' = 2\frac{K_W}{2\Omega_W}\frac{\cosh[\frac{\Omega_W}{v}(\frac{L}{2}+x')] + \frac{K_W}{K_L}\frac{\Omega_L}{\Omega_W}\sinh[\frac{\Omega_W}{v}(\frac{L}{2}+x')]}{2\frac{K_W}{K_L}\frac{\Omega_L}{\Omega_W}\cosh[\frac{\Omega_W}{v}L] + (1+(\frac{K_W}{K_L}\frac{\Omega_L}{\Omega_W})^2)\sinh[\frac{\Omega_W}{v}L]} \tag{4.25}$$

Use equation (3) and integrate x' from $-L/2$ to $L/2$ and get

$$\frac{1}{L}\int_{-L/2}^{L/2} dx' \sigma_\omega(x,x')|_{x=L/2} = \frac{e^2}{h}\frac{2v(-i\omega)}{\Omega_W^2 L}\frac{\sinh[\frac{\Omega_W}{v}L] + \frac{K_W}{K_L}\frac{\Omega_L}{\Omega_W}(\cosh[\frac{\Omega_W}{v}L]-1)}{2\frac{K_W}{K_L}\frac{\Omega_L}{\Omega_W}\cosh[\frac{\Omega_W}{v}L] + (1+(\frac{K_W}{K_L}\frac{\Omega_L}{\Omega_W})^2)\sinh[\frac{\Omega_W}{v}L]} \tag{4.26}$$

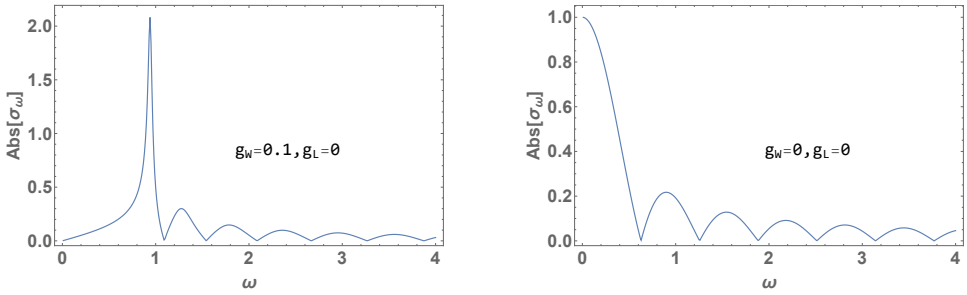

Figure 21: a.c. conductivity for two sets of parameters. For both plots $K_W = K_L = 1$, $L = 10$.

In Fig.21 we present the results for two sets of parameters $g_W = g_L = 0$ and $g_W = 0.1, g_L = 0$. If we take the $\omega \to 0$ limit from previous equation, we observe that the d.c. conductivity depends entirely on the lead, which is always quantized. This is exactly what have been observed in the LAO/STO experiments by our collaborators in Jeremy Levy's group. To investigate the properties of the TLL in the wire, one needs to perform a.c. measurement, where we can gain more information based on the frequency dependence of the conductivity.

4.7 Mathematica code for section 4.2

```
    pairgetElem[klist1_, klist2_, U_, NN_] := Module[{k1, k2},
   If[klist1 == klist2,
    k1 = klist1;
    -4. Cos[k1] + U/NN,
    k1 = klist1;
    k2 = klist2;
    U/NN
    ]];
pairgetk1k2[nn_, NN_] := 2 \[Pi]/NN*nn;
pairgetHH[NN_, U_] := Module[{klist1, klist2},
   Table[
    klist1 = pairgetk1k2[ii, NN];
    klist2 = pairgetk1k2[jj, NN];
    pairgetElem[klist1, klist2, U, NN]
    , {ii, 1, NN}, {jj, 1, NN}]];
pairgetElem2[klist1_, klist2_, kp_, U_, NN_] := Module[{k1, k2},
   If[klist1 == klist2,
    k1 = klist1;
```

```
    -2. Cos[k1] - 2. Cos[kp - k1] + U/NN,
    k1 = klist1;
    k2 = klist2;
    U/NN
    ]];
pairgetHH2[NN_, U_, kp_] := Module[{klist1, klist2},
   Table[
    klist1 = pairgetk1k2[ii, NN];
    klist2 = pairgetk1k2[jj, NN];
    pairgetElem2[klist1, klist2, kp, U, NN]
    , {ii, 1, NN}, {jj, 1, NN}]];

pairgetE0[klist_, klist2_, NN_] := Module[{k1},
   If[klist == klist2,
    k1 = klist;
    -2.*Cos[k1],
    0]
   ];
pairgetH0[NN_] := Module[{klist1, klist2},
   Table[
    klist1 = pairgetk1k2[ii, NN];
    klist2 = pairgetk1k2[jj, NN];
    pairgetE0[klist1, klist2, NN]
    , {ii, 1, NN}, {jj, 1, NN}]];

trigetElem[klist1_, klist2_, U_, NN_] := Module[{k1, k2, k3, k4},
   If[klist1 == klist2,
    {k1, k2} = klist1;
    -2. Cos[k1] - 2 Cos[k2] - 2 Cos[k1 + k2] + 3 U/NN,
    {k1, k2} = klist1;
    {k3, k4} = klist2;
    If[Mod[(k1 + k2 - k3 - k4)/(2. \[Pi]), 1] ==
       0 || (k1 == k3) || (k2 == k4),
     U/NN, 0]
    ]];
trigetk1k2[nn_, NN_] := Module[{n1, n2},
   {n1, n2} =
    If[Mod[nn, NN] == 0, {Quotient[nn, NN],
      NN}, {Quotient[nn, NN] + 1, Mod[nn, NN]}];
   2 \[Pi]/NN*{n1, n2}
   ];
trigetHH[NN_, U_] := Module[{klist1, klist2},
   Table[
    klist1 = trigetk1k2[ii, NN];
    klist2 = trigetk1k2[jj, NN];
    trigetElem[klist1, klist2, U, NN]
    , {ii, 1, NN^2}, {jj, 1, NN^2}]];
```

```
newgetk1k2[nn_, NN_] := 2 \[Pi]/NN*nn;
trigetE0[klist_, klist2_, NN_] := Module[{k1},
   If[klist == klist2,
    k1 = klist;
    -2.*Cos[k1],
    0]
   ];
trigetH0[NN_] := Module[{klist1, klist2},
   Table[
    klist1 = newgetk1k2[ii, NN];
    klist2 = newgetk1k2[jj, NN];
    trigetE0[klist1, klist2, NN]
    , {ii, 1, NN}, {jj, 1, NN}]];
trigetElem2[klist1_, klist2_, kp_, U_, NN_] := Module[{k1, k2, k3, k4},
   If[klist1 == klist2,
    {k1, k2} = klist1;
    -2. Cos[k1] - 2 Cos[k2] - 2 Cos[kp - k1 - k2] + 3 U/NN,
    {k1, k2} = klist1;
    {k3, k4} = klist2;
    If[Mod[(k1 + k2 - k3 - k4)/(2. \[Pi]), 1] ==
       0 || (k1 == k3) || (k2 == k4),
     U/NN, 0]
    ]];
trigetk1k2[nn_, NN_] := Module[{n1, n2},
   {n1, n2} =
    If[Mod[nn, NN] == 0, {Quotient[nn, NN],
      NN}, {Quotient[nn, NN] + 1, Mod[nn, NN]}];
   2 \[Pi]/NN*{n1, n2}
   ];
trigetHH2[NN_, U_, kp_] := Module[{klist1, klist2},
   Table[
    klist1 = trigetk1k2[ii, NN];
    klist2 = trigetk1k2[jj, NN];
    trigetElem2[klist1, klist2, kp, U, NN]
    , {ii, 1, NN^2}, {jj, 1, NN^2}]];
```

5.0 EMERGENT MODE AND BOUND STATES IN ONE-COMPONENT ONE-DIMENSIONAL LATTICE FERMIONIC SYSTEMS

5.1 Introduction

In the previous chapter we talked about bound state formed from fermions of different bands. In this chapter we discuss an even simpler model which consists of a single fermionic channel. The original goal for studying this model was to see if bound states of multiple fermions can form in the single-component lattice fermion system.

To do this we consider a Hamiltonian with finite range interactions (as discussed in the model Hamiltonina section), at shorter range the interaction is attractive to promote the formation of bound states, at larger distances the interaction is repulsive to avoid phase separation[1]. In section 5.3 (Numerical details) we present the numerical details of our calculation: the parameter range we choose, the method we use (DMRG) and the quantities we measure.

Next in section 5.4, we present the main numerical results, specifically the phase diagram and Fourier spectra through two cuts of our phase diagram. We analyze each of the phases in the phase diagram. One of the phases has an emergent mode and its explanation goes beyond the standard TLL. We discuss in detail on the central charge and correlators in each phase later in section 5.6.

Based on the numerical findings we come up with a 2-mode theory which explains the results we get. In section 5.5 We describe in details the construction of the theory as well as the predictions of theory which agree with our numerical data. In section 5.6 we present the central charge calculation as well as the correlators in each phase.

[1] Phase separation means that all the particles come together and form a cluster.

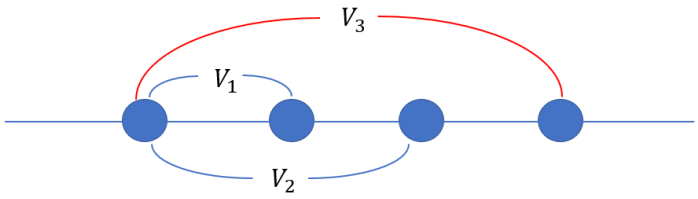

Figure 22: Schematic picture of the model Hamiltonian. $V_1, V_2 < 0$ and $V_3 > 0$ to promote the formation of bound states of multiple fermions (pairs and trions).

In section 5.7 we discuss the phases transitions in the phase diagram. We construct a collapse method for measuring the central charge right at the transition point for single to pair transition. We also speculate on the nature of other transitions and provide DMRG data at the interface of single and trion phase. Finally in section 5.8 we present numerical data for quaternion phase (bound states of four fermions) as an extension to our results.

5.2 Bound states of multiple fermions

5.2.1 model Hamiltonian

In this chapter we consider the one-component one-dimensional lattice model with finite range interactions. The Hamiltonian is of the following form: where c_i and $c_i^\dagger$ are the fermion

$$H = \sum_i \left[-\frac{1}{2}\left(c_i^\dagger c_{i+1} + c_{i+1}^\dagger c_i \right) + \sum_{m=1}^{3} V_m n_i n_{i+m} \right], \tag{5.1}$$

annihilation and creation operators at lattice site i, $n_i = c_i^\dagger c_i$ is the number operator, and V_m defines the shape of the fermion-fermion interaction potential. Notice here we omit the definition of the hopping parameter t which is common in most lattice models[2].

Fig. 22 shows a schematic picture of the parameter setup. We choose short-ranged attractive interactions ($V_1 < 0$ and $V_2 < 0$) to promote the formation of pairs and trions,

[2]We can view this as $t = 1$ and our paramters are in units of t

but with $V_3 > 0$ to prevent phase-separation[48]. In order to decrease the parameter space we restrict our attention to the subspace $V_1 = V_2$[3]. We expect that extending the range of attractive interactions will result in liquid phases of multi-fermion bound states. As an example We provide the numerical evidence for quaternion phase where we introduce another V_4 into the model.

In our numerical simulations we focus on the low filling ratios (primarily 1/5 filling), where the expected phases are single phase (TLL of a single fermion), pair phase (TLL of pair fermions) and trion phase (TLL of bound states of three fermions).

5.3 Numerical details

5.3.1 how we run DMRG

Throughout this chapter we use Prof. Roger Mong's implementation[49;50] the standard two-sites iDMRG[34;51;52] to study the ground state properties of the Hamiltonian (5.1) with focus on the 1/5 filling with a unit cell of 30 fermion sites (lower filling fraction would require larger unit cell for our computation and introduce more computational cost). The number of particles in conserved in the DMRG calculation and package np_conserved is used.

As discussed in the DMRG chapter, the accuracy is controlled by the bond dimension χ, where the result becomes exact as $\chi \to \infty$. In our calculations we use various bond dimensions χ for the purpose of checking convergence and doing finite χ scaling. The central charge diagram Fig. 23 is computed using $\chi = \{40, 80, 160, 300\}$. The Fourier spectra Fig. 24 is plotted using the $\chi = 300$ data. The parameter range we use for $V_1 = V_2$ are -1 to -0.65 and the range for V_3 is 1 to 1.7.

Another important quantities we calculate in the DMRG is the correlation length ξ, which is used to compute the central charge c and also determine whether correlators are algebraically or exponentially decaying. χ also depends on bond dimension and we denote its dependence as $\xi(\chi)$. In the DMRG calculation we can seperate quantities into various charge sectors and for each charge sector q, we can compute $\xi_q(\chi)$–the length scale for correlators of

[3]We have also run data points at $V_1 = 2V_2$ and reproduce the same phases as discussed in this chapter.

form $\langle A^\dagger(0)B(r)\rangle$ where A, B are charge-q operators. As χ increases, $\xi_q(\chi)$ goes to infinity as long as that charge-q sector is gapless. If instead, the charge-q sector is gapped, then $\xi_q(\chi)$ saturates to its physical value $\xi_q(\infty)$.

As discussed in the following sections, we find for Tomanaga Luttinger liquids of $q_{\min}$-bound states, the charge q-sectors are gapless only if q is a multiple of $q_{\min}$. In practice if $\xi_{q=jq_{\min}}(\chi), j = 0, 1, 2...$ reach some values significantly larger than other charge sectors whose $\xi_q(\chi)$ tend to saturate, we claim the formation of liquid of $q_{\min}$-bound states. The neutral sector ($q = 0$) is always gapless in our calculation and the corresponding $\xi_0(\chi)$ is used to extract c[39], which we we discuss in details in the following subsection.

One last aspect regarding our DMRG calculation is that translational invariance is not preserved exactly by iDMRG at finite χ. Instead, the magnitude of violation decays algebraically with increasing χ. When we compute correlators, we average over sites r_1 in one unit cell: $G(r) = \frac{1}{\text{unit cell size}} \sum_{r_1} G(r_1, r_1 + r)$. We also do this when calculating entanglement entropy. The averaging improves the quality of the data.

5.3.2 entanglement entropy and central charge

To analyze the properties of the ground states that we obtain through DMRG, we calculate physical quantities such as bi-partite entanglement entropy S, central charge c and various correlators.

The entanglement entropy serves as a measure of quantum-mechanical nature of correlations[39]. The entanglement entropy of a pure state of a bipartite system AB is defined as: where $\rho_{A/B}$ are the reduced density matrix of subsystem $A(B)$.

$$S = -Tr\rho_A \log \rho_A = -Tr\rho_B \log \rho_B, \tag{5.2}$$

In our numerical calculations we study the bipartite entanglement entropy S, i.e., the von Neumann entropy of DMRG ground state traced over either half the system. Both S

and the correlation length ξ are infinite for the true ground state, but are cut off by finite χ. The manner in which these two variables diverge gives the central charge[39;53] [4]:

$$S = \frac{c}{6}\log(\xi) + \text{const} \tag{5.3}$$

Numerically the calculation of correlation length is given by $\xi = -1/(\log(\lambda_1))$, where λ_1 is largest eigenvalue of the normalized density matrix of the system and $\sum_i \lambda_i^2 = 1$. In practice, we perform numerical calculations on various bond dimensions and linear fit the relation between entanglement entropy S and the log of correlation length ξ to extrapolate the central charge. We will show the fitting of central in each phase later in the chapter.

One important fact about central charge is that it is related to the degree of freedom of the system. The system we are working on are Tomanaga-Luttinger liquids and the expected phases are 1 mode phases (single, pair, trion) with central charge 1 and 2-mode phase (2M) with central charge 2. Therefore the central charge serves as a measure of the number of distinct gapless mode in our numerical calculation.

In our numerical calculations we use bond dimensions of $40, 80, 160, 300$ and linear fit the relation between entanglement entropy S and correlation length ξ to extract central charge c. In the following discussions we will show the overall central charge plot and centra charge fit in each phases.

5.3.3 correlators

The other important quantities that we calculate through DMRG are the correlators. More specifically we compute the single, pair and trion two-point correlators: The qualitative behavior of correlators tell whether the corresponding mode are gapped or gapless. In the single phase all correlators decay algebraically; in the pair phase only G_2 decays algebraically

[4]This formula was derived in the context of a CFT, where there is a single velocity. For two-component phases, we still use this formula as an operational definition of the central charge despite the likely possibility of mismatched Fermi velocities.

$$G_1(r) = \left\langle c_i^\dagger \, c_{i+r} \right\rangle, \tag{5.4a}$$

$$G_2(r) = \left\langle (c_i c_{i+1})^\dagger \, c_{i+r} c_{i+r+1} \right\rangle, \tag{5.4b}$$

$$G_3(r) = \left\langle (c_i c_{i+1} c_{i+2})^\dagger \, c_{i+r} c_{i+r+1} c_{i+r+2} \right\rangle. \tag{5.4c}$$

while G_1 and G_3 decay exponentially; in the trion phase G_3 is algebraic while G_1 and G_2 are exponential. This behavior implies that there is a gap to adding a single fermion into the pair/trion phase however there is no gap to adding two/three fermions.

In our numerical calculations we calculate the correlators up to five times of the correlation length. The decay character are obtained through a log-log plot of the correlators as a function of distance r and algebraically decay manifest as a linear feature in such plots. We show the plots of correlators in different phases in the discussion of corresponding phases.

5.3.4 sample code

In this subsection we present the sample code for this chapter. We present the sample code in several parts where we explain the usage of each parts.

```
def model_longsc(t, V1, V2, V3):
        t, V1, V2, V3 = float(t), float(V1), float(V2), float(V3)
        Jcouplingz = np.hstack([[0], [V1], [V2], [V3]])
        Jcouplingpm = np.hstack([[0], [- t]])
        #print Jcouplingz
        #print Jcouplingpm
        #plt.plot(J)
        #plt.yscale('log')
        #plt.show()
        Mpar = {
                'verbose': 2,
                'L': 1,
                'S': 0.5,
                'Jz': Jcouplingz,
                'Jpm': Jcouplingpm,
                'Veps': 1e-6,
```

```
17                'ignore_herm_conj':False,
18                'parstring': 't{}_V{},{},{}'.format(t, V1, V2, V3),
19        }
20        return Mpar
21
22
23 default_sim_par = {
24        'VERBOSE': True,
25        'STARTING_ENV_FROM_PSI': 1,
26        'N_STEPS': 20,
27        'MAX_ERROR_E': 1e-10,
28        'MAX_ERROR_S': 1e-8,
29        'MIN_STEPS': 40,
30        'MAX_STEPS': 5000,
31        'LANCZOS_PAR' : {'N_min': 2, 'N_max': 20, 'e_tol': 5*10**(-15),
             'tol_to_trunc': 1/5.},
32 #       'mixer': (1e-3, 1.5, 5, 'id'),
33 }
```

This is the part where we define the model Hamiltonian. We use long_range_spin_chain model in the TenPy2 package. The parameters are t, V_1, V_2, V_3.

```
1  def run_dmrg(sim, dmrg_par, model_par=None, chi=None, min_steps=None,
       save_sim=False):
2         if sim is None:
3                 print 'Initializing "{}"...'.format(model_par['parstring'])
4                 M = mod.spin_chain_model(model_par)
5                 psi = iMPS.product_imps(M.d, [M.up, M.up, M.up, M.up, M.up, M.up,
                      M.up, M.up, M.up, M.up, M.up, M.up, M.dn, M.dn, M.dn, M.dn,
                      M.dn, M.dn, M.up, M.up, M.up, M.up, M.up, M.up, M.up, M.up,
                      M.up, M.up, M.up, M.up], dtype=np.float, conserve = M,
                      bc='periodic')
6                 sim = simulation.simulation(psi, M)
7                 sim.model_par = model_par
8
9         else:
10                if model_par is not None:
11                        print 'Updating simulation
                              "{}"...'.format(model_par['parstring'])
12                        sim.update_model(model_par)
13                else:
14                        print 'Running simulation
                              "{}"...'.format(model_par['parstring'])
15                try:
16                        del sim.canon_psi
17                except:
18                        pass
```

```
19
20          sim_par = deepcopy(dmrg_par)
21          if chi is not None: sim_par['CHI_LIST'] = {0:chi}
22          if min_steps is not None: sim_par.update['MIN_STEPS'] = min_steps
23          sim.dmrg_par = sim_par
24          print 'DMRG parameters:\n' + '\n'.join([ " {} : {}".format(k,v) for k,v
                in sim.dmrg_par.items() ])
25          sim.ground_state()
26
27          try:
28                  sim.append
29          except AttributeError:
30                  sim.append = {}
31          if 'xi' in sim.append: del sim.append['xi']
32
33          sim.append['GS Energy'] = sim.sim_stats[-1]['Es'][-1]
34          sim.canon_psi = sim.psi.copy()
35          sim.canon_psi.canonical_form()
36          if save_sim:
37                  filename = outroot + model_par['parstring'] +
                        '_chi{}'.format(max(sim_par['CHI_LIST'].values()))
38                  uncanon_psi = sim.psi
39                  sim.psi = sim.canon_psi
40                  print 'Presaving simulation to "{}"...'.format(filename)
41                  sim.save(filename)
42          sim.append['xi'] = sim.canon_psi.correlation_length()
43          print "xi = {}".format(sim.append['xi'])
44
45          sim.append['Sbond'] = np.average(sim.canon_psi.entanglement_entropy())
46          print "Sbond = {}".format(sim.append['Sbond'])
47
48          if save_sim:
49                  print 'Saving simulation to "{}"...'.format(filename)
50                  sim.save(filename)
51                  sim.psi = uncanon_psi
52          print
53          return sim
```

This is the part where we run DMRG. We set the initial state in a unit cell of 30 and use periodic boundary condition. In the end, we save the energy, entanglement entropy and correlation length of the ground state.

```
1   if 1:
2           t = 1.0
3           V1 = float(sys.argv[1])
4           V2 = float(sys.argv[2])
```

```
        V3 = float(sys.argv[3])
        for V1 in [V1]:
                for V2 in [V2]:
                        for V3 in [V3]:
                                for ii in range(8):
                                        model_par = model_longsc(t, V1, V2, V3)
                                        sim = load_sim(model_par, [40, 80, 120, 160,
                                            200, 240, 300, 400, 500, 550, 600,
                                            840][ii])
                                        if sim is None:
                                                sim_par = deepcopy(default_sim_par)
                                                CHI_LIST = dict([(0,14), (60,20),
                                                    (120,28), (200,40), (260,80),
                                                    (320,120), (380,160), (460, 200),
                                                    (560, 240), (700, 300), (600,
                                                    400), (700,500), (900, 550),
                                                    (1000, 600), (1200, 840)][:ii+4])
                                                logfile = outroot2 +
                                                    model_par['parstring'] +
                                                    '_chi{}.out'.format([40, 80, 120,
                                                    160, 200, 240, 300, 400, 500, 550,
                                                    600, 840][ii])
                                                pipe_output(logfile)
                                                sim_par.update({'CHI_LIST':CHI_LIST,
                                                    'MIN_STEPS':1.2*max(CHI_LIST.keys())})
                                                sim = run_dmrg(None, sim_par,
                                                    model_par=model_par, save_sim=True)
                                        else:
                                                continue
##############################################################################################
if 1:
        t = 1.0
        datalist = []
        for V1 in [-0.901,-0.9016,-0.902,-0.903,-0.904]:
                for V2 in [V1]:
                        for V3 in [1.4]:
                                model_par = model_longsc(t, V1, V2, V3)
                                for chi in [40, 80, 120, 160, 200, 240, 300, 400,
                                    600, 840][6:7]:
                                        sim = load_sim(model_par,chi)
                                        if sim is None: continue
                                        if hasattr(sim, 'canon_psi'):
                                                psi = sim.canon_psi
                                        else:
                                                psi = sim.psi
                                        M = sim.M
                                        xi = sim.append['xi']
```

```
38                                      dist = int(5 * xi)
39                                      site_n1 = 0.5 -
                                            psi.site_expectation_value(M.Sz)
40                                      corr_c1d_c1 =
                                            psi.string_correlation_function([M.Sm[0]],
                                            [M.Sp[0]], dist + 20, OpStr=2*M.Sz[0])
41                                      corr_pairing =
                                            psi.string_correlation_function([M.Sm[0],
                                            M.Sm[0]], [M.Sp[0], M.Sp[0]], dist + 20,
                                            OpStr=None)
42                                      corr_nn =
                                            psi.string_correlation_function([M.Sm[0],
                                            M.Sp[0]], [M.Sm[0], M.Sp[0]], dist + 20,
                                            OpStr=None)
43                                      corr_tring =
                                            psi.string_correlation_function([M.Sm[0],
                                            M.Sm[0], M.Sm[0]], [M.Sp[0], M.Sp[0],
                                            M.Sp[0]], dist + 20, OpStr=2*M.Sz[0])
44                                      datalist.append([t,V1,V2,V3,site_n1,
                                            sim.append['xi'],sim.append['Sbond'],sim.append['GS
                                            Energy'], corr_c1d_c1, corr_pairing,
                                            corr_nn, corr_tring])
45          file = open("lsctestTri6in30v314line.txt", "w")
46          file.write(to_mathematica_lists(datalist))
47          file.close()
```

In the first part we run the DMRG for a set of parameters t, V_1, V_2, V_3 on different bond dimensions. In the second part we load the saved calculations. In the loading procedure, we also measure various correlation functions: single correlator (corr_c1d_c1), pairing correlator (corr_*pairing*), density-density correlator (corr_nn) and trion correlator (corr_tring). In the end we save all the measured data into a text file for further analysis.

5.4 Numerical results

5.4.1 phase diagram

Using the central charge data and the correlators we can readily generate the phase diagram. Specifically we first calculate the central charge and identify the number of modes in each region. Then we analyze the decay behavior of correlators to distinguish between one-mode

phases (single, pair and trion).

Figure 23 shows c as a function of the interaction parameters $V_1 = V_2$ and V_3. The blue regions denote the single-mode phases with $c = 1$, we identify these as single, pair, and trion phases based on their two-point correlators [Eq. (5.4)]. While we observe a direct transition between the pair and single phases[1;48], we do not find a direct transition between the pair and trion phases; instead we find an intermediate phase with $c \approx 2$ which we call the 2M (2-mode) phase (we will discuss in detail about this 2M phase later in this chapter). The 2M phase neighbors all other phases and indicates a parent theory with an emergent mode, which enables a unified description of the multi-fermion bound-state phases and their phases transitions, wchich I will discuss in the next section.

The phase transition regions in Fig. 23 have central charge larger than 2. In such regions our previous formula Eq.(5.3) doesn't work and exact calculation of central charge require data collapse which we will discuss in the phase transition section later in this chapter.

5.4.2 Fourier spectra

Having obtained the phase diagram we want to gain more information about each individual phase. We achive this by analyzing the properties of various correlators in Eq.(5.4). The long-distance behavior of the correlation functions of gapless operators can be written as a sum of algebraically decaying terms of the form

$$\frac{\cos(k_{\text{osc}}|r| + \varphi)}{|r|^{\eta}}. \tag{5.5}$$

Note here the correlators have power law decay as a function of r and we need to perform Fourier transform with derivatives to compensate the pow law decay: the "n^{th}" derivative of Fourier transform on the correlation functions $G_{1,2,3}(r)$: where the value of r_{trunc} is set to be several times of the correlation length $\xi_0(\chi)$.

Any harmonic component (Eq. (5.5)) of correlators with algebraic decay exponent $\eta <$

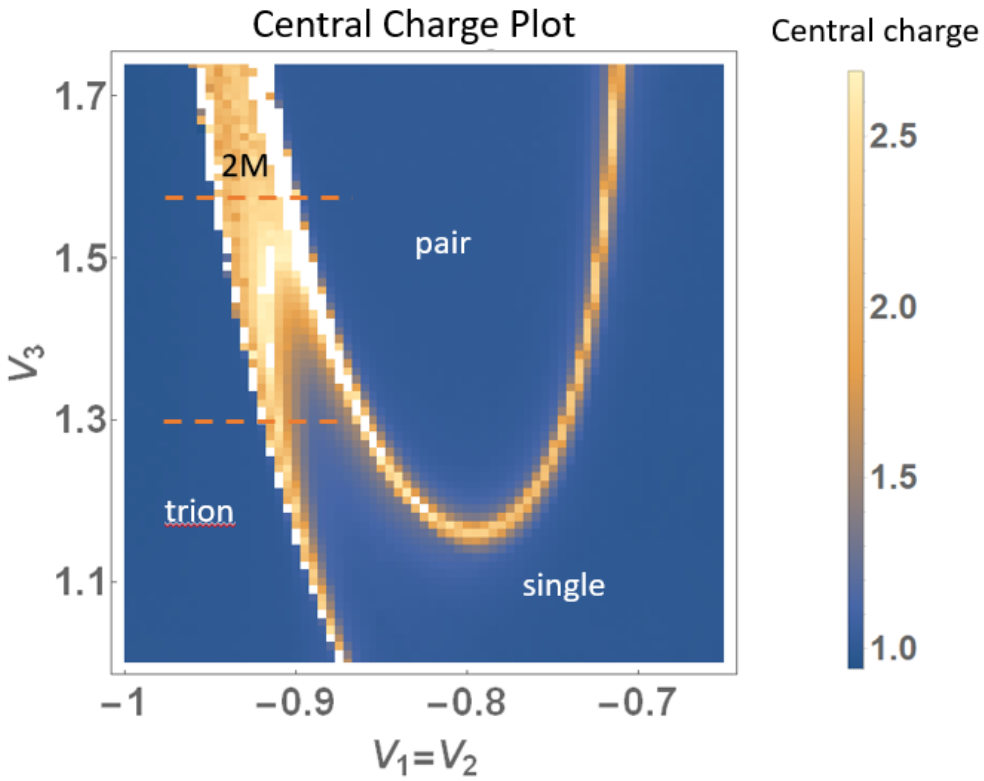

Figure 23: Central charge as a function of interactions in the lattice model (5.1) computed at filling fraction 1/5. We have identified single, pair and trion phase based on the central charge and correlators. Besides these three phases there is a region with $c \approx 2$ which we call 2M phase. The two dashed lines represent the linecuts for our Fourier spectra analysis.

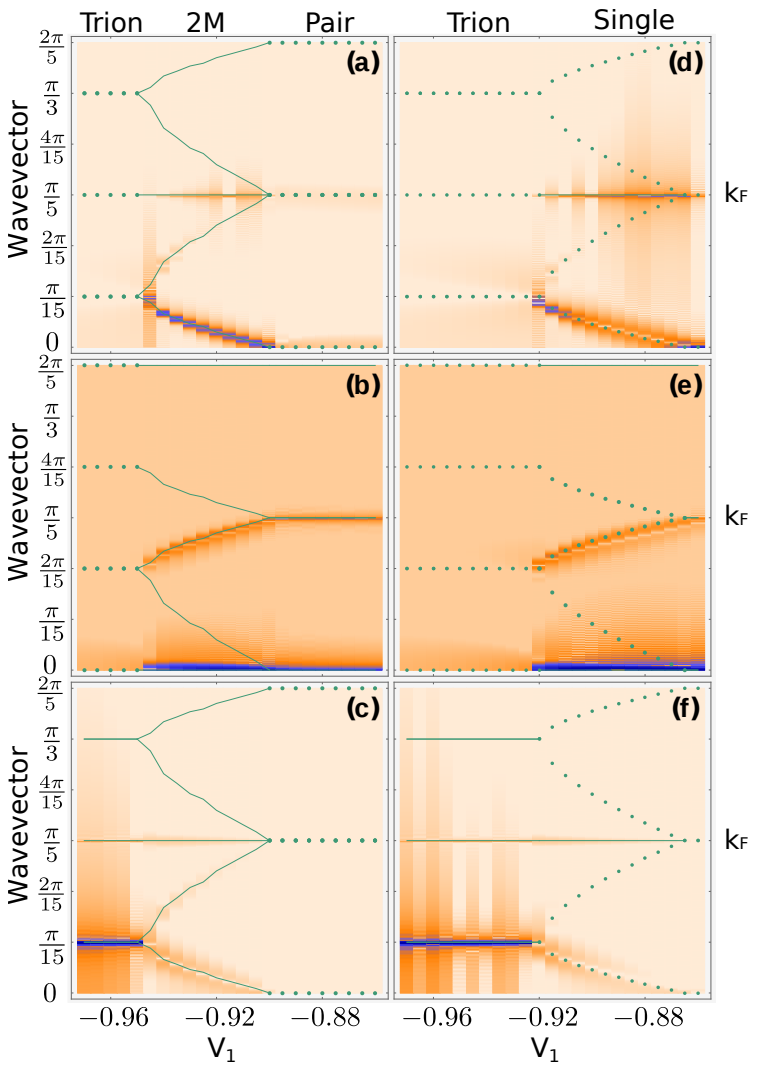

Figure 24: Spectra G_1, G_2 and G_3 (from top to bottom) as a function of wavevector and interaction strength ($V_1 = V_2$), showing agreement of peak locations between DMRG and theory. The data is taken at cuts shown in Fig. 23. Plots (a–c) taken at $V_3 = 1.56$ show the trion, 2M, and pair phases; plots (d–f) taken at $V_3 = 1.3$ show the trion and single phases (with a possible 2M phase in between). Darker (Blue) colors represent larger values of amplitudes. The peak in the data of G_1, which continuously varying between 0 and $k_F/3$ in the 2M/single phase is identified as k'. The lines added to the color plot are theoretic predictions with the determined parameter k'. The solid lines denote several long distance k_{osc} associated with algebraic-decay; the dotted lines denote several exponential-decay "peaks", which are possibly visible if the decay-length-scale is large. The peak smaller than the k_F in the single phase in panel (d) is not expected in the single phase and can be viewed as a precursor of the trion phase.

$$\tilde{G}^{n}_{1,2,3}(q) = \frac{1}{\sqrt{2r_{\text{trunc}}}} \sum_{r=-r_{\text{trunc}}}^{r_{\text{trunc}}} e^{iqr}|r|^{n} G_{1,2,3}(r), \tag{5.6}$$

$n+1$ will in principle show a divergent peak at the corresponding k_{osc}. In our numerics to make the subleading k_{osc} visible, we choose $n = 2$, 2.5, 2.8 for G_1, G_2 and G_3.

The Fourier spectra is shown in Fig.24. In panels (d-f) we see the linecut goes through single and trion phase: in the single phase all correlators decay algebraically and we see the strongest peaks for G_1 and G_3 is k_F, for G_2 is 0, there are second order peaks which are reminiscent of possible 2M phase in between (I will discuss about this in the later section of this chapter); in the trion phase only G_3 decays algebraically and we observe no features on panel (d-e). In panel (f) we see distinct peaks at $k_F/3, k_F, 5k_F/3$. The peak at $k_F/3$ is expected based on the conservation of particle number. Other peaks are odd multiples of $k_F/3$ which matches the results of a Tomanaga Luttinger liquid theory of bound states of trions(I will discuss in details in the 2-mode theory section).

Panels (a-c) shows the linecut at $V_3 = 1.56$ which goes through trion, 2M and pair phase. The trion phase shows the same behavior as in panel (f). In the pair phase only G_2 has power law decay and show visible peaks on Fouerier spectra. The peaks are at 0 and k_F, which is in agreement with a TLL of pairs. In the 2M phase we observe something interesting: From panel (a) we see two distinct peaks: one fixed at k_F and one moving from $k_F/3$ to 0, connecting the trion and pair phase. The appearance of an additional moving peak is beyond standard single-mode TLL theory and the interpretation requires a new theory.

5.5 2-mode theory

Motivated by Ref.[1;48] and our numerical data, we introduce a theory with two modes. In this theory, the charge-1 operators in the lowest harmonic are: where $\eta = +1/-1$ denotes a right/left mover; θ_μ is dual field of the compact bosonic field ϕ_μ and satisfies

$$\begin{aligned}\psi^{(\pm)}_{0,\eta} &= e^{\pm i\theta_1} e^{i\theta_0 + i\eta(\phi_0 + k_{\mathrm{F}} x)},\\ \psi^{(\pm)}_{1,\eta} &= e^{i\theta_0} e^{\pm i\theta_1 \pm i\eta(\phi_1 + k' x)},\end{aligned} \tag{5.7}$$

$[\partial_x \theta_\mu(x), \phi_\nu(x')] = i\pi\delta_{\mu\nu}\delta(x - x')$. The charge is carried by the θ_0 mode, while θ_1 is neutral, as a result k_{F} is fixed by the density of electrons while k' is a free parameter.

The set of local physical operators can be generated via products of operators from Eq. (5.7), i.e., $\left(\psi^+_{0,1}\right)^l \left(\psi^+_{0,-1}\right)^m \left(\psi^-_{1,1}\right)^n \cdots$. (Note that the generators Eq. (5.7) are over-complete.) As a result, primary operators of charge q take the form: Due to the restrictions

$$\begin{gathered}c(x)^q \sim \sum_{q_1, r_0, r_1} e^{i(q\theta_0 + q_1\theta_1 + r_0(\phi_0 + k_{\mathrm{F}} x) + r_1(\phi_1 + k' x))},\\ \text{where } q_1 \equiv r_0 + r_1 \equiv q \pmod 2.\end{gathered} \tag{5.8}$$

on the coefficients q_1, r_0, and r_1 of physical operators, we cannot simply treat this theory as a product of θ_0/ϕ_0 and θ_1/ϕ_1 theories.

The theory must obey charge conservation, and is invariant under both parity ($\phi_{0,1} \to -\phi_{0,1}$ and $x \to -x$) and time-reversal ($\theta_{0,1} \to -\theta_{0,1}$, $i \to -i$ and $t \to -t$). Generically, the kinetic part of the Hamiltonian takes the form: $\mathcal{H}_{\mathrm{KE}}$ describes a 2-mode TLL, which we

$$\mathcal{H}_{\mathrm{KE}} = \sum_{\mu,\nu} \left[A_{\mu\nu} (\partial_x \theta_\mu)(\partial_x \theta_\nu) + B_{\mu\nu} (\partial_x \phi_\mu)(\partial_x \phi_\nu) \right]. \tag{5.9}$$

later demonstrate to be consistent with the 2M phase found in the numerics.

5.5.1 single mode phase as a descent of the 2-mode theory

Having talked about the 2M theory, we now discuss how we can achieve single-mode phase from the 2-mode theory.

The single-mode phases (single, pair, trion, ...) are constructed by introducing locking terms, shown in Table 1, to the Hamiltonian Eq. (5.9). For a term to appear, it must be of the form of Eq. (5.8) with $q = 0$, and also respect parity and time-reversal. At large interaction strength, some of these terms may 'lock'[28]; taking an expectation value and reducing the theory to a 1-component TLL.

Our analysis for the locking terms is as follows[54]. For an interaction term to lock it should have no oscillation (i.e., x dependence), which places constraints on the Fermi momenta. For each locking term of the form $\cos\Lambda$, we find linear combinations of the θs and ϕs that commute with Λ. Among this set we find a conjugate pair which we denote as θ_+ and ϕ_+. The set of gapless operators are then generated by $e^{i\Lambda}$, $e^{i\theta_+}$ and $e^{i\phi_+}$ and must be a subset of Eq. (5.8) [5]. We show that the minimal (unit) charges for these operators are indeed $q_{\min} = 1$, 2, 3 for the single, pair, and trion phases respectively, with the given locking terms. We will show the locking terms and the corresponding phases in the next section.

5.6 Data and theory in each phases

Having obatined the numerical data and constructed the theory, we now examine the agreement of theory predictions and data in each phase that appeared in our phase diagram Fig. 23.

5.6.1 single phase

Single phase is the standard Tomanaga Luttinger liquid. We find this phase when the attractive interaction is not strong enough to form bound states of multiple particles. In this

[5] Although the operators $e^{ib\Lambda}$ are not gapless, they are long-ranged correlated (ordered).

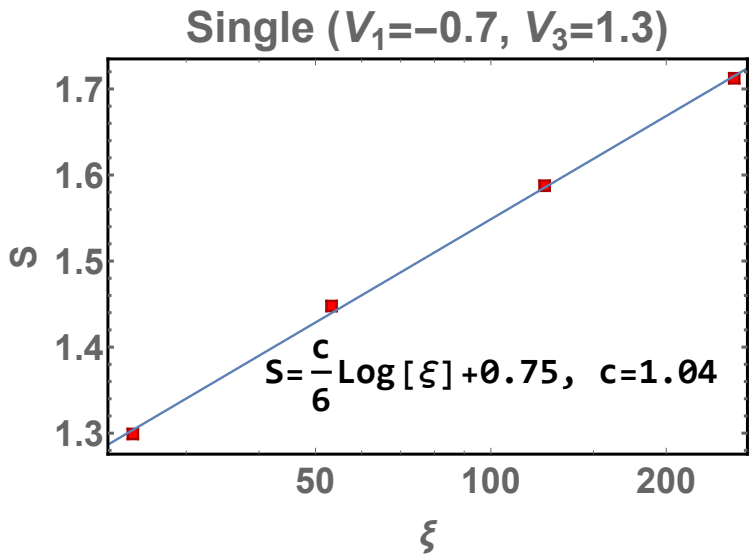

Figure 25: Entanglement entropy v.s. correlation length on a linear-log scale in the single phase. From the linear fit we obtain $c = 1.04$. The data is taken at $V_1 = -0.7, V_3 = 1.3$.

subsection we first show the numerical data for this phase: central charge fit, correlators, Fourier spectra, then we discuss how to get the single phase from the 2-mode theory, and the agreement of theory and numerics.

5.6.1.1 central charge and correlators In the single phase the central charge is calculated by linear fitting entanglement entropy S and the log of correlation length ξ as in Eq. (5.3). As an example we pick a point $V_1 = V_2 = -0.7, V_3 = 1.3$ in the phase diagram and the fit is shown in Fig. 25. From the fit we get a central charge of 1.04.

Next we analyze the correlators and their Fourier spectra, shown in Fig. 26. We see that all the correlators decay as power law at $r < \xi$ where ξ is the correlation length, shown as the dashed lines on the left three plots of Fig. 26. The right three figures plot the Fourier spectra of all the correlators: for G_1 and G_3 we see the spectra peaks at $k_F = \pi/5$ and for G_2 the spectra shows peaks at 0 and $2k_F$, which is exactly what we would expect for a standard Tomanaga Luttinger liquid.

5.6.1.2 single phase as a descent of the 2-mode theory Having presented the numerical results, we now discuss how to get the single phase from our 2-mode theory. Here

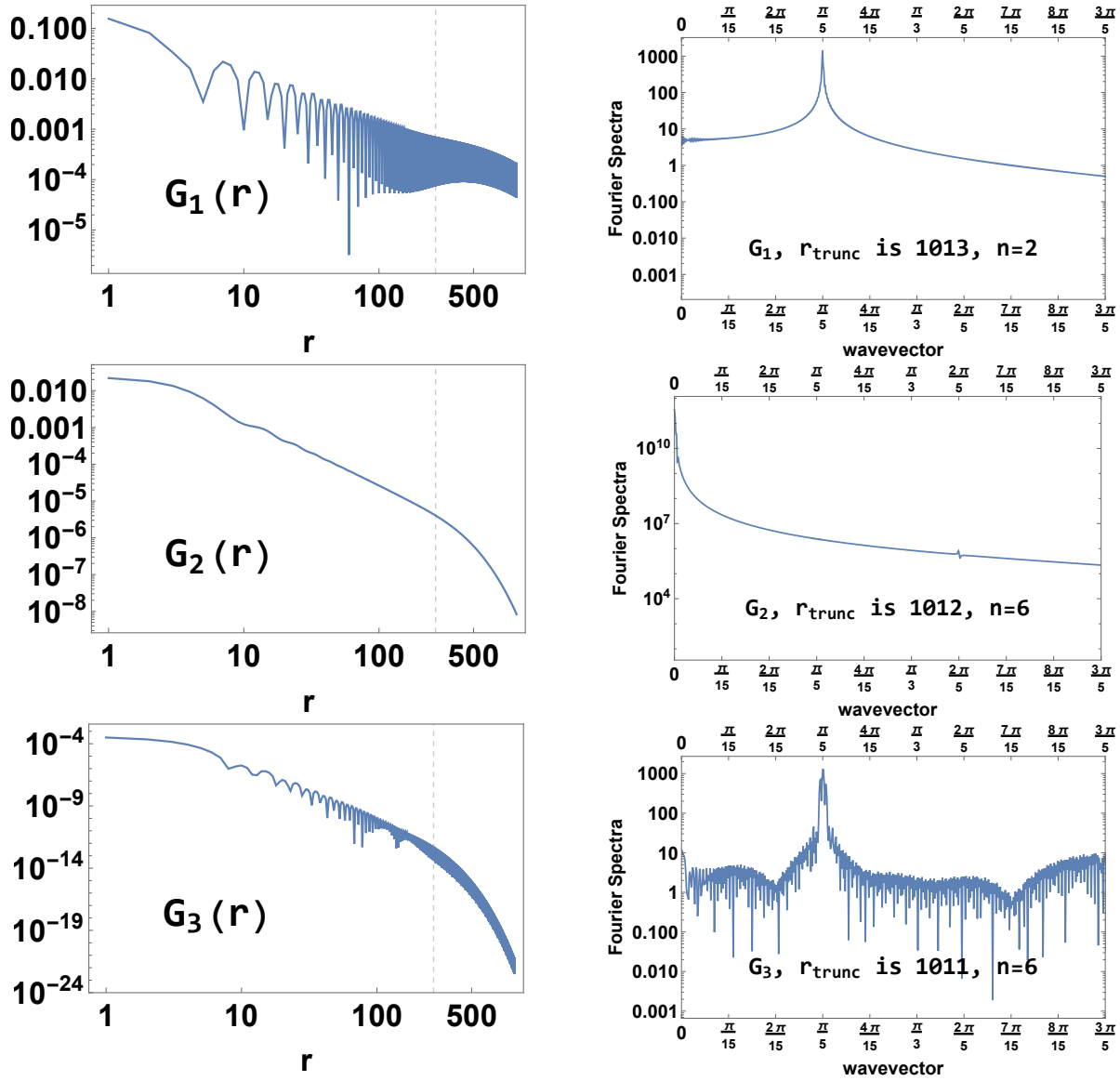

Figure 26: Correlators $G_1(r), G_2(r), G_3(r)$ and theirs Fourier spectra in the single phase at $V_1 = -0.7, V_3 = 1.3$ and filling ratio of 1/5. The dashed lines on the left figures denote the correlation length ξ, and all the correlators decay exponentially after $r > \xi$. On the right figures we see k_F peak for G_1 and G_3, and 0 and $2k_F$ peaks for G_2.

the locking term is $\cos(\Lambda)$ where $\Lambda = 2\theta_1$. To get the gapless mode, we need to find θ_+ and ϕ_+ such that they commute with Λ. We can readily write down $\theta_+ = \theta_0$ and $\phi_+ = \phi_0$. Then the set of gapless operators are generated by $e^{i\Lambda}$, $e^{i\theta_+}$ and $e^{i\phi_+}$ and must be of the form Eq. (5.8). The general form of gapless operators is where n is an integer and a an odd integer. Note that $\Lambda = 2\theta_1$ is locked, $e^{i\theta_1}$ is a constant, $c(x)$ reduces to which is the standard

$$c(x) \sim \sum e^{ia\theta_1} e^{i\theta_0} e^{i(2n+1)(\phi_0+k_F x)} \tag{5.10}$$

$$c(x)^1 \approx \sum_{n=-\infty}^{\infty} e^{i\theta_0} e^{i(2n+1)(\phi_0+k_F x)}, \tag{5.11}$$

bosonization form of a fermion mode[28;55].

5.6.2 pair phase

Pair phase is the Tomanaga Luttinger liquid of pairs, we find this phase when the attractive interaction is strong enough to form pairs, but not strong enough to form trions. In this subsection we first show the numerical data for this phase: central charge fit, correlators, Fourier spectra, then we show how to obtain the pair phase from the 2-mode theory, and discuss the agreement of theory and numerics.

5.6.2.1 central charge and correlators In the pair phase the central charge is calculated by linear fitting the entanglement entropy S and the log of correlation length ξ as in Eq. (5.3). As an example we pick a point $V_1 = V_2 = -0.8, V_3 = 1.3$ in the phase diagram and the fit is shown in Fig. 27. From the fit we get a central charge of 1.03.

Next we analyze the correlators and their Fourier spectra, shown in Fig. 28. We see that only $G_2(r)$ decays as power law with repect to r while $G_1(r)$ and $G_3(r)$ decay exponentially. This means that only excitations of 2-particles are gapless, adding a single particle or 3 particles would require a finite energy. From this we identify the phase as pair phase. Because $G_1(r)$ and $G_3(r)$ decay exponenetially, we cannot extract the Fourier spectra from

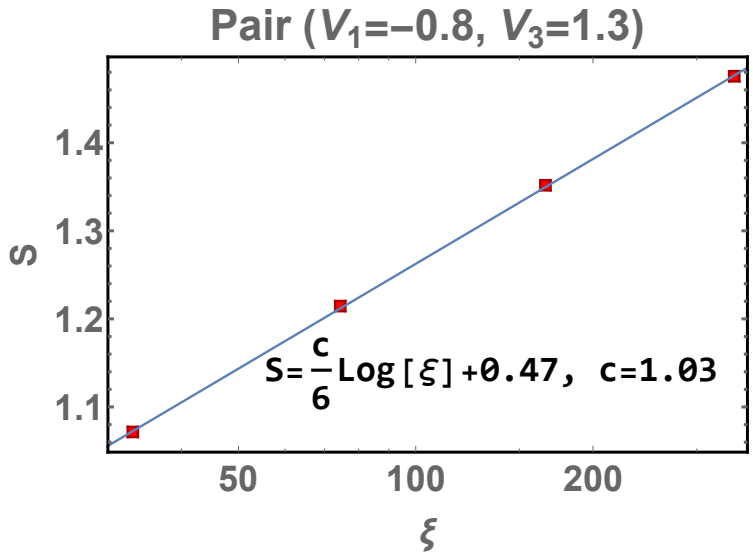

Figure 27: Entanglement entropy v.s. correlation length on a linear-log scale in the pair phase. From the linear fit we obtain $c = 1.04$. The data is taken at $V_1 = -0.8, V_3 = 1.3$.

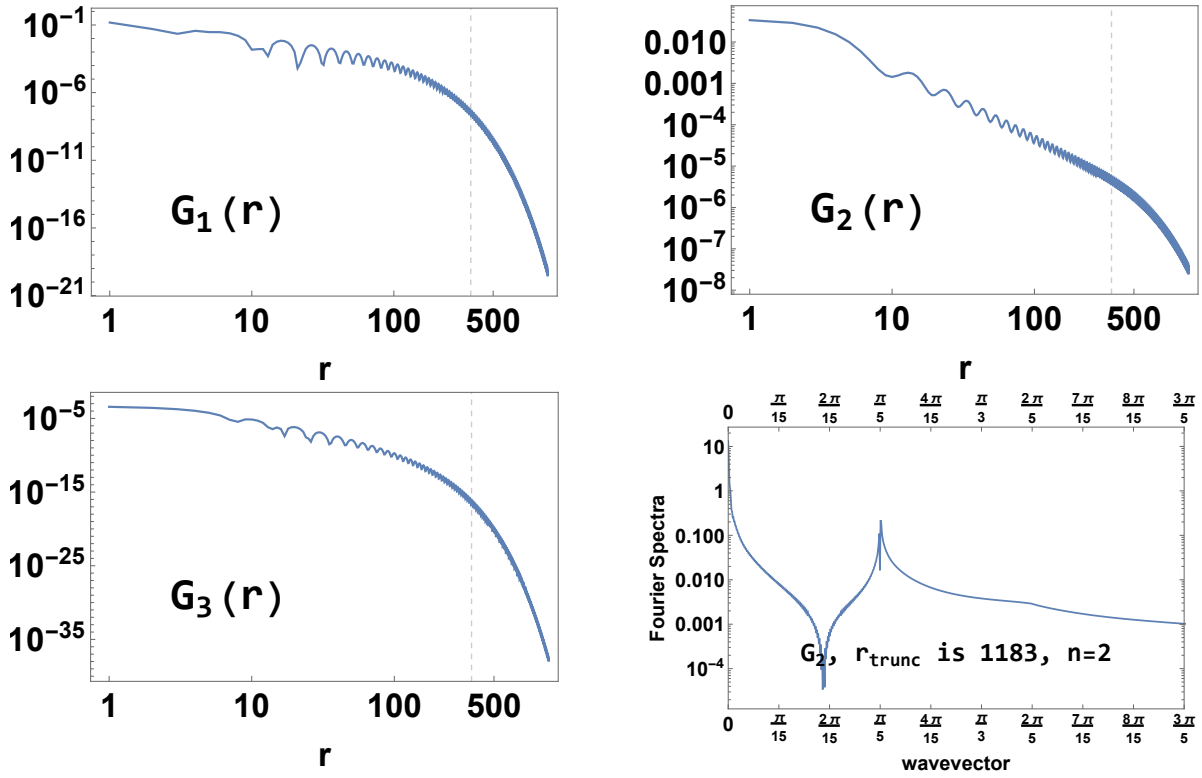

Figure 28: Correlators $G_1(r), G_2(r), G_3(r)$ and the Fourier spectra of G_2 in the pair phase at $V_1 = -0.8, V_3 = 1.3$ and filling ratio of 1/5. We see that only G_2 decays algebraically while G_1 and G_3 decay exponentially. The Fourier spectra of G_2 is shown, with peaks at 0 and k_F.

Fourier transform with derivatives, so we only present the Fourier spectra of G_2. We see that the spectra peaks at k_F, which is different compared the the spectra of G_2 in the single phase. We will discuss about this peak in the following subsubsection.

5.6.2.2 pair phase as a desecnt of the 2-mode theory Having presented the numerical results, we now discuss how to get the pair phase from our 2-mode theory. Here the locking term is $\cos(\Lambda)$ where $\Lambda = 2\phi_1 + 2k'x$. Recall that the locking term cannot have any x dependence, we immediately get $k' = 0$. As θ_1 is disordered, it cannot appear in the exponent of a gapless operator, i.e., $q_1 = 0$. From the parity relation (5.8), we see that q must be an even integer and thus the single and trion correlators decay exponentially, which agrees with our numerical findings.

To get the gapless mode, we need to find θ_+ and ϕ_+ such that they commute with Λ. We can readily write down $\theta_+ = 2\theta_0$ and $\phi_+ = \phi_0/2$. Then the set of gapless operators are generated by $e^{i\Lambda}$, $e^{i\theta_+}$ and $e^{i\phi_+}$ and must be of form Eq. (5.8). The general form of gapless operators are where n is an integer and $k_B = k_\mathrm{F}/2$. This is the standard bosonization form

$$c(x)^2 \sim b(x) \approx \sum e^{i\theta_+} e^{i(2n)(\phi_+ + k_B x)}, \tag{5.12}$$

of a boson mode[28;55]. We interpret the descendant theory as a TLL of fermion pairs, with the density of pairs being half of the density of elementary fermions.

5.6.3 trion phase

Trion phase is the Tomanaga Luttinger liquid of trions, we find this phase when the attractive interaction is strong enough to form trions. In this subsection we first show the numerical data for this phase: central charge fit, correlators, Fourier spectra, then we talk about how to get the trion phase from the 2-mode theory, and the agreement of theory and numerics.

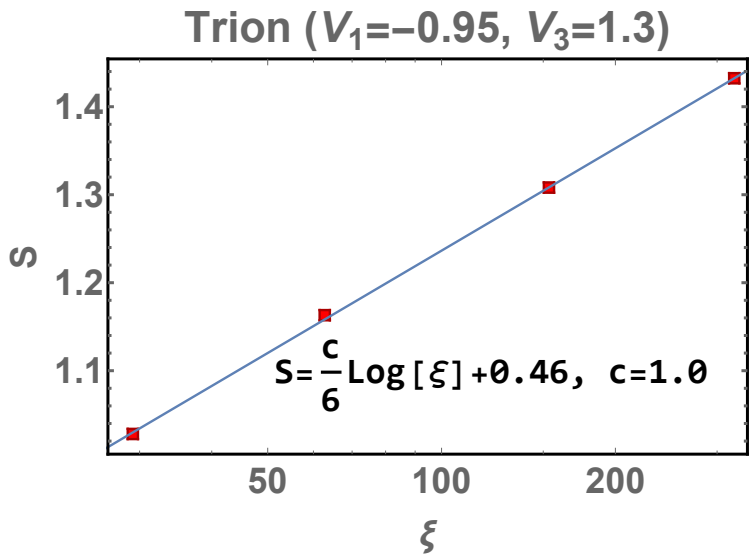

Figure 29: Entanglement entropy v.s. correlation length on a linear-log scale in the trion phase. From the linear fit we obtain $c = 1.0$. The data is taken at $V_1 = -0.95, V_3 = 1.3$.

5.6.3.1 central charge and correlators In the trion phase the central charge is also calculated by linear fitting entanglement entropy S and the log of correlation length ξ as in Eq. (5.3). As an example we pick a point $V_1 = V_2 = -0.95, V_3 = 1.3$ in the phase diagram and the fit is shown in Fig. 29. From the fit we get a central charge of 1.0, which means there are only one gapless mode in such phase.

Next we analyze the correlators and their Fourier spectra, shown in Fig. 30. We see that only $G_3(r)$ decays as power law with repect to r while $G_1(r)$ and $G_2(r)$ decay exponentially. This means that only excitations of 3-particles are gapless, adding a single particle or 2 particles would require a finite energy. From this we identify the phase as trion phase. Because $G_1(r)$ and $G_2(r)$ decay exponenetially, we omit their Fourier spectra and only present the Fouerier spectra of G_3. We see that the spectra peaks at $k_F/3$ and k_F, which is different as compared to the the spectra of G_3 in the single phase.

5.6.3.2 trion phase as a desecnt of the 2-mode theory Having presented the numerical results, we now discuss how to get the trion phase from our 2-mode theory. Here the locking term is $\Lambda = 3(\phi_1 + k'x) - (\phi_0 + k_{\mathrm{F}}x)$ which yields the trion phase while fixing $k' = k_{\mathrm{F}}/3$. As Λ commutes with $\theta_+ = 3\theta_0 + \theta_1$ and $\phi_+ = \phi_1$, the gapless operators take

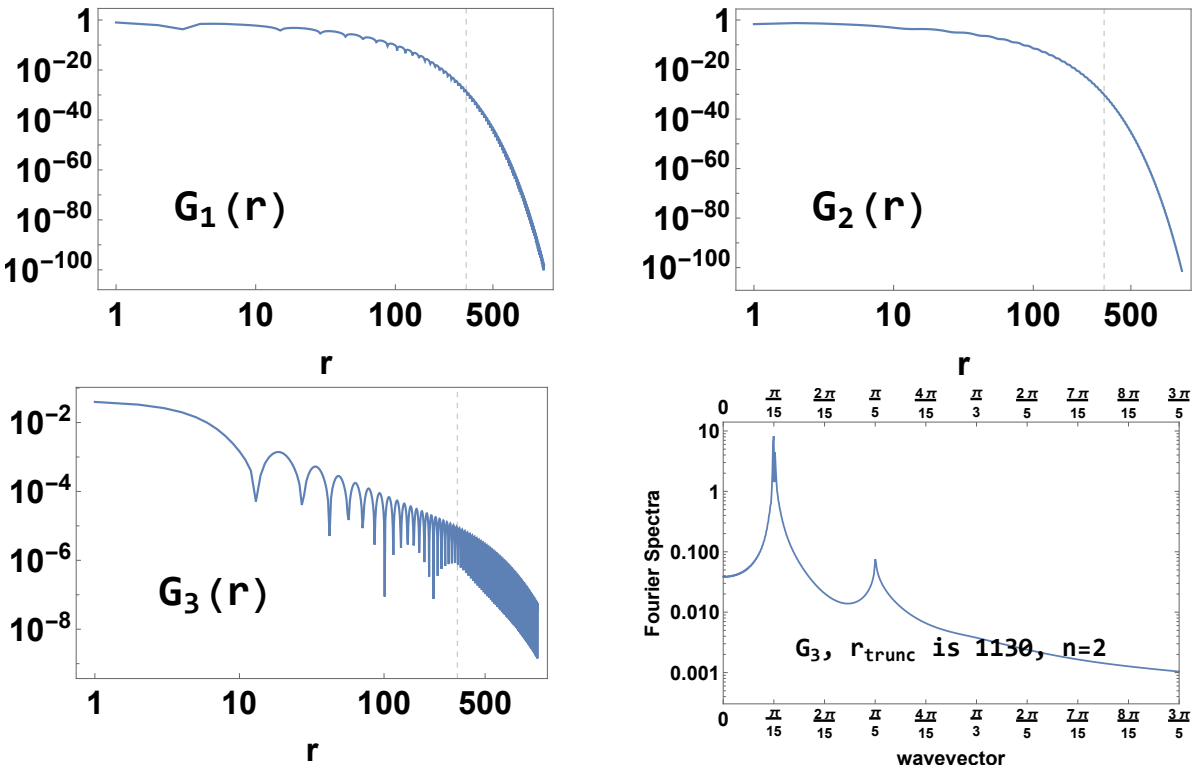

Figure 30: Correlators $G_1(r), G_2(r), G_3(r)$ and the Fourier spectra of G_3 in the trion phase at $V_1 = -0.8, V_3 = 1.3$ and filling ratio of 1/5. In the trion phase only G_3 decays algebraically while G_1 and G_2 decay exponentially. The Fourier spectra of G_3 show peaks at $k_F/3$ and k_F.

the form $c(x)^q \sim \sum e^{i(q/3)\theta_+} e^{ia(\phi_+ + k'x) + ibL}$. Mapping the expression to Eq. (5.8), we get $q_1 = q/3$, $r_0 = -b$, and $r_1 = a + 3b$; we determine the consistency conditions $q/3, a, b \in \mathbb{Z}$ and $a \equiv q \pmod 2$. Hence for any gapless operator, q must be a multiple of 3, which implies exponential decay of G_1 and G_2. As Λ takes on an expectation value, the trion operator expansion reduces to: $c(x)^3 \sim \sum e^{i\theta_+} e^{i(2n+1)(\phi_+ + k'x)}$, where $k' = k_F/3$ is the Fermi wavevector of the trions and n is an integer.

5.6.4 summary of locking terms and validation of decaying exponents

5.6.4.1 summary of locking terms and resulting phases Having discussed the locking terms in the single-mode phases we now summarize the results. Within the low

Locking term	$\cos(2\theta_1)$	$\cos(2k'x + 2\phi_1)$	$\cos[(3k' - k_F)x + 3\phi_1 - \phi_0]$
Resulting phase	single	pair	trion
Single correlator $G_1(r)$	$\sum_n \frac{\sin[(2n+1)k_F\lvert r\rvert]}{\lvert r\rvert^{(1/K+(2n+1)^2K)/2}}$		
Pair correlator $G_2(r)$	$\sum_n \frac{\cos[(2n)k_F\lvert r\rvert]}{\lvert r\rvert^{2/K+2n^2K}}$	$\sum_n \frac{\cos[(2n)\frac{k_F}{2}\lvert r\rvert]}{\lvert r\rvert^{(1/K+(2n)^2K)/2}}$	
Trion correlator $G_3(r)$	$\sum_n \frac{\sin[(2n+1)k_F\lvert r\rvert]}{\lvert r\rvert^{(9/K+(2n+1)^2K)/2}}$		$\sum_n \frac{\sin[(2n+1)\frac{k_F}{3}\lvert r\rvert]}{\lvert r\rvert^{(1/K+(2n+1)^2K)/2}}$

Table 1: Locking terms and correlators of single-mode phases. The first line lists interaction terms and the second line shows the corresponding phases when interaction terms get locked. The remaining rows show the algebraic decay form of correlators $G_{1,2,3}$; the coefficient of each term is neglected for simplicity. In Fig. 31, we show the numeric data verifying the predicted dependence.

energy theory for each of the three single TLL mode phases, $c(x)^{q_{\min}}$ admits a standard bosonization expansion in terms of θ_+ and ϕ_+. The effective Hamiltonian is thus where K

$$\mathcal{H}_+ = \frac{v_+}{2\pi}\big[K(\partial_x\theta_+)^2 + \frac{1}{K}(\partial_x\phi_+)^2\big], \tag{5.13}$$

is the Luttinger parameter.

We summarize various locking terms and the resulting phases in Table. 1. We aslo present the forms of algebraically decaying correlators in each phase. Next we validate the decaying exponents in the table in the pair phase and trion phase.

5.6.4.2 validation of decaying exponents in the pair and trion phases We demonstrate that the pair and trion phases are well-described by a single-mode TLL theory. We do this by extracting the decay exponents of the correlators from our data, and comparing them to prediction from TLL theory. In particular, we first extract the Luttinger parameter K from the scaling dimension of the leading oscillatory term in the density operator. We then

compute the leading decay exponent ($\eta_{2,3}$) of $G_{2,3}$, and show that they follow the relation $\eta(K)$ as predicted by TLL theory.

We first show that K can be read out from charge-density wave quasi-order. The density-density correlator is defined as: where $n_i = c_i^\dagger c_i$. TLL theory predicts $n(x) \sim \langle n \rangle + \partial_x \phi_+ / \pi +$

$$G_0(r) = \langle n_i n_{i+r} \rangle - \langle n_i \rangle^2 , \tag{5.14}$$

$\sum_{m \neq 0} e^{i2m(\phi_+ + k_F x/q_{\min})} + \ldots$ and thus the long-distance behavior of $G_0(r)$ reads: where the

$$G_0(r) = \frac{1}{r^2} + \sum_{m \neq 0} \frac{\cos(2m k_{\mathrm{F}} r/q_{\min})}{|r|^{2m^2 K}} + \ldots , \tag{5.15}$$

coefficient of each term is neglected. The term with $m = 1$ is the leading oscillatory (quasi-CDW order) term with decay exponent $2K$. Thus the leading scaling dimension of the quasi-CDW order is K.

While it is possible to extract K by computing G_0 from our data, we choose to fit K by taking advantage of the artificial long-range charge-density-wave order induced by iDMRG. The method [6] is as follows. When the unit cell of iDMRG is commensurate to the oscillatory vector(s) of the quasi-charge-density-wave order, there is a corresponding artificial long-range density-wave order induced from finite bond dimension χ, the amplitude of which decays with χ and the correlation length $\xi_0(\chi)$. Specifically, its amplitude scales as where

$$\left\langle n\left(\frac{2k_F}{q_{\min}}\right) \right\rangle_\chi \propto \xi_0(\chi)^{-K}, \tag{5.16}$$

[6] The method works for any quasi-orders which are not forced to vanish by the MPS ansatz

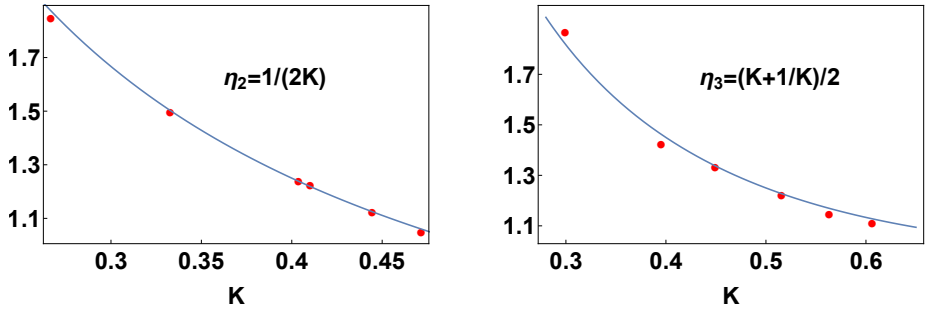

Figure 31: Verification of predicted decay exponents. Left figure: leading decay exponent (η_2) of pair correlator in pair phase. Right figure: leading decay exponent (η_3) of trion correlator in trion phase. The two lines are prediction from TLL theory. According to Table 1, $\eta_2 = \frac{1}{2K}$, $\eta_3 = \frac{1}{2}(K + \frac{1}{K})$. The values of Luttinger parameter K are extracted from the information of neutral sector. In order to cover larger range of K, we use DMRG data from fillings (left to right) $\frac{1}{5}$, $\frac{1}{6}$,... $\frac{1}{10}$. The parameters for the left figure are $V_1 = V_2 = -0.8$, $V_3 = 1.4$; the parameters for the right figure are $V_1 = V_2 = -1$, $V_3 = 1.4$.

$\langle n(2k_F/q_{\min})\rangle = \sum_j e^{2ik_F/q_{\min}j} \langle n_j\rangle$. For our plots, we use the peak-to-peak amplitude of the density profile as a substitute for $\langle n(2k_F/q_{\min})\rangle$.

TLL theory [cf. Tab. 1] gives the prediction of leading term of $G_{2,3}$ of pair and trion phases respectively as: with We numerically fit $\eta_{2,3}$ directly from the data of $G_{2,3}$.

$$\begin{aligned} G_2(r) &= \frac{1}{|r|^{\eta_2}} + \ldots, \\ G_3(r) &= \frac{\sin(k_F|r|/3)}{|r|^{\eta_3}} + \ldots, \end{aligned} \tag{5.17}$$

$$\begin{aligned} \eta_2 &= \frac{1}{2K}, \\ \eta_3 &= \frac{1}{2}\left(K + \frac{1}{K}\right). \end{aligned} \tag{5.18}$$

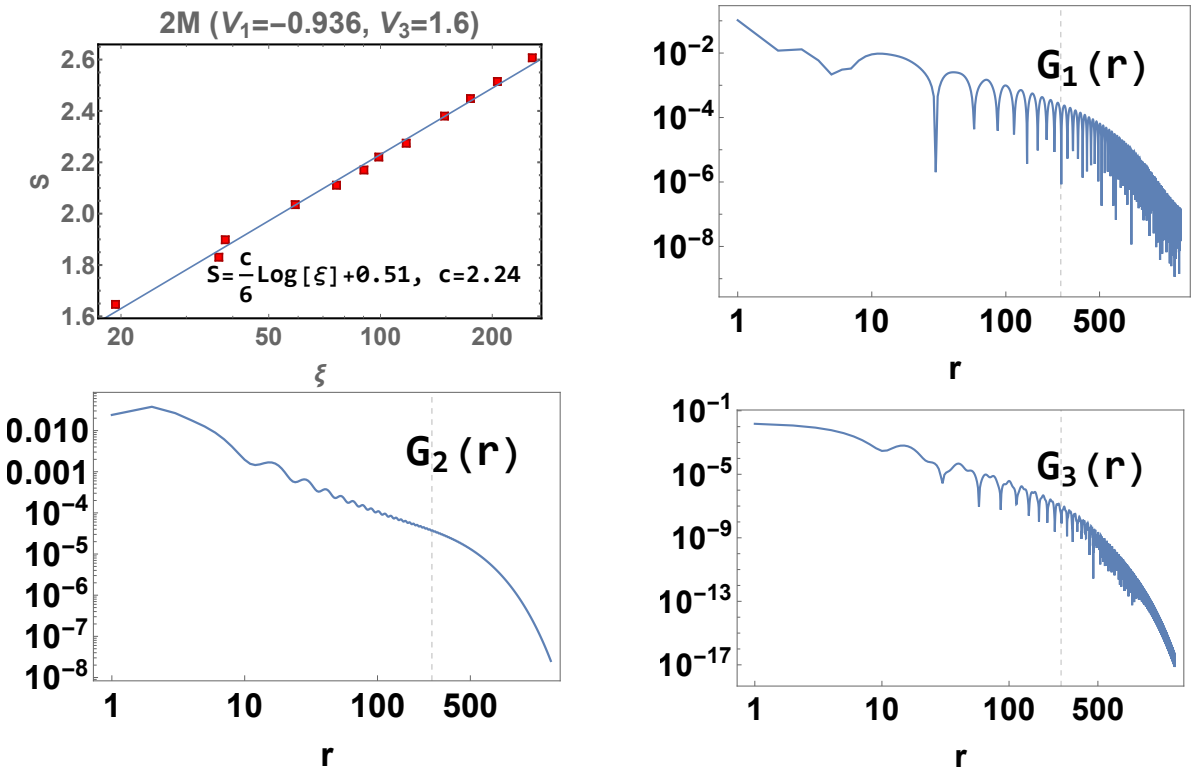

Figure 32: DMRG data for the 2M phase at $V_1 = V_2 = -0.9936, V_3 = 1.6$: central charge fit with bond dimensions 40, 57, 80, 120, 160, 200, 240, 300, 450, 600, 800, 1200; Correlators $G_1(r), G_2(r), G_3(r)$ in the same data point with bond dimension 1200, all showing algebraically decay.

Figs. 31(a) and (b) show $\eta_{2,3}$ vs. K for the pair and trion phases respectively. We see that the data points (red) agree with Eqs. (5.18) (blue line), which shows that the liquids are well described by single-mode TLL theory. We also note that the extracted Luttinger parameters K are all smaller than 1; this indicates the effective interaction between pairs or trions is repulsive.

5.6.5 2M phase

The 2M phase is a direct prediction of our 2-mode theory: there are no locking terms and we natually get the phase with two gapless mode. In this subsection we first present the central charge calculation, then we present the correlators in the 2-mode theory. We also

discuss the nature of the two gapless modes in the 2M phase.

5.6.5.1 central charge in the 2M phase To calculate the central charge, we use the same fitting method where we linear fit the relation between entanglement entropy and the log of correlation length. The result is shown in Fig. 32. We see that linear fitting gives $c = 2.24$. The reason that it is not exactly at 2 is an artifact of the finite bond dimensions we use and the central charge moves towards 2 as we add higher bond dimension data.

5.6.5.2 correlators in the 2M phase The correlators in the 2M phase are shown in Fig. 32. We observe pow law decay for all the correlators, indicating that all the modes are gapless. Combining the fact that we have two wavevectors and all the correlators decay algebraically, we readily see the necessity of our 2-mode theory.

A key feature of the DMRG data in the 2M phase is that k' is not fixed; it varies continuously between the two limiting values $k' = k_{\mathrm{F}}/3$ on the trion side and $k' = 0$ on the pair side (while $k = k_F$ remains fixed). The variation of this wavevector is a clear signature of a neutral emergent mode and confirms our effective two-mode TLL.

5.7 phase transitions

There are five potential phase transitions in our phase diagram, which we discuss here. The locking mechanisms give hints about the phase transitions, we shall now discuss our data for each of these transitions. Later we provide numerical evidence for single-pair transition and DMRG data at the interface of single and trion phases.

- Single-pair transition. The transition is controlled by the competition between the terms $\cos(2\theta_1)$ and $\cos(2\phi_1)$, and results in a quantum Ising transition[1;48;56–58]. In the next subsection, we provide the definitive evidence that the single-pair transition is Ising via finite-χ scaling.
- 2M-single transition. This transition is driven by the term $\cos(2\theta_1)$, and is likely a Berezinskii-Kosterlitz-Thouless (BKT) transition.

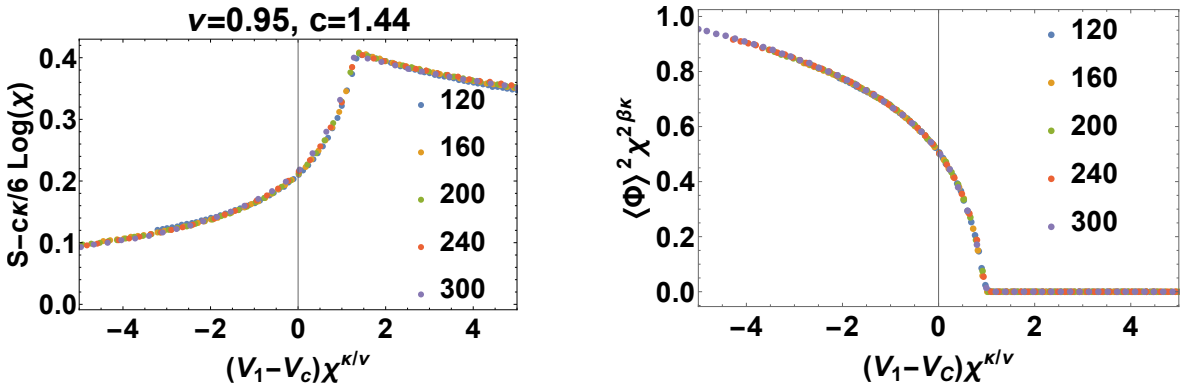

Figure 33: single to pair transition collapsing: (left) collapse of the entanglement entropy (S) data computed as a function of the tuning parameter ($V_1 = V_2$) for various bond dimensions (χ – indicated by different color points as labeled) using the scaling ansatz Eq. (5.19); (right) collapse of the disorder parameter (Φ) computed as a function of the tuning parameter ($V_1 = V_2$) for various bond dimensions (χ – indicated by different color points as labeled) using the scaling ansatz Eq. (5.21).

- 2M-pair/trion transition. The 2M-to-pair and 2M-to-trion transitions are accompanied by k' reaching a commensurate value. This suggests a commensurate-incommensurate (CIC) transition
- Single-trion transition. We are unable to determine if there is a direct transition between the trion and single phase, or whether there is an intervening 2M phase which extends down as V_3 is decreased. In both cases, our numeric analysis suggests a (at least one) first-order transition, the DMRG data is shown in subsection 5.7.2.

5.7.1 sinlge-pair transition

In this section we investigate the single-pair phase transition. We establish that this is an Ising transition by (1) measuring the central charge at the critical point, (2) measuring the correlation length critical exponent ν, and (3) identifying the order parameter for the pair phase and finding its scaling dimension β. Our technical approach is to perform a two-parameter scaling collapse on our DMRG data, where the parameters are detuning $V_1 - V_C$ and bond dimension χ.

We begin by extracting the central charge at the critical point and the correlation length critical exponent by analyzing the entanglement entropy in the vicinity of the critical point. Using the finite χ scaling of CFT states[39], we collapse the entanglement entropy data from various χ near the pair-single transition. The collapse ansatz is as follows: where $\kappa = \frac{6}{c(1+\sqrt{\frac{12}{c}})}$ and ν is the correlation-length critical exponent and f is the universal function for this collapsing. We note that $\nu = 1$ and $c = 1/2$ for the Ising transition. The best collapse of our DMRG data yields $\nu = 0.95$ and $c = 1.44$. These values differ by less than 5% from the Ising critical point values, once we realize that in addition to the CFT that corresponds to the Ising transition, there is a background free boson CFT with central charge 1, and thus $c = 1 + 1/2 = 3/2$. We suspect that the 5% deviation is due to the subleading corrections to the entanglement entropy scaling, which have been ignored in the collapse anstaz.

$$S - \frac{c\kappa}{6}\log(\chi) = f\left((V_1 - V_c)\,\chi^{\kappa/\nu}\right), \tag{5.19}$$

We also analyze the expectation value of the vortex operator $\Phi(x)$ and perform the corresponding collapse of the finite χ data (Fig. 33). The vortex operator $\Phi(x)$, is neutral and incurs a π phase upon braiding (in spacetime) with fermions; i.e., it anticommutes with fermion operators on its left and commutes with fermion operators on its right. Expanding in terms of primary fields, $\Phi(x)$ has the following operator expansion: The operator $\cos(\phi_1 + k'x)$, which is one of the lowest harmonic terms in $\Phi(x)$, acquires long-range order in the pair phase, because $\cos(2\phi_1)$ is locked and $k' = 0$. In the context of the Ising transition, $\cos(\phi_1)$ corresponds to the disordered parameter, which gains an an expectation value on

$$\Phi(x) \sim \sum_{r_0,r_1} e^{i(r_0(\phi_0+k_{\mathrm{F}}x)+r_1(\phi_1+k'x))}, \quad \text{where } r_0 + r_1 \text{ is odd.} \tag{5.20}$$

the disordered side of the transition with the magnetization critical exponent β.

In our lattice model, the vortex operator corresponds to: $\Phi(x) = \prod_{j<x}(-1)^{n_j}$. Its two-point correlator is well defined and measurable in iDMRG. Its large distance limit gives: $\lim_{r\to\infty} \langle \Phi(i+r)\Phi(i)\rangle = \langle\Phi\rangle^2$. We measure $\langle\Phi\rangle^2$ near the phase transition point for various bond dimensions χ and the collapse the data using the following ansatz: In Fig. 33, we plug

$$\langle\Phi\rangle^2 \chi^{2\beta\kappa} = g\left((V_1 - V_c)\,\chi^{\kappa/\nu}\right). \tag{5.21}$$

in the exact Ising exponents $\beta = \frac{1}{8}$, $\nu = 1$, and $\kappa = \frac{6}{c(1+\sqrt{\frac{12}{c}})}$ with $c = 3/2$ to obtain good collapse of the iDMRG data near the Ising transition.

5.7.2 DMRG data at the interface of single and trion phases

We also analyze the iDMRG data along the cut $V_3 = 1.02$ which goes from the trion to the single phase. In Fig. 34 we plot $\Delta E(V_1) = E(V_1) - (aV_1 + b)$, the ground state energy minus a linear component, as a function of the tuning parameter V_1. We subtract the linear component to make the kink in the ground state energy easier to visualize. We see that ΔE has different slopes on trion/single side, which is a signature of a first-order transition. However, we cannot rule out the possibility that there is an intermediate 2M phase between the trion and the single mode phases.

5.8 quaternion phase

The Hamiltonian Eq. (5.1) can be extended to have longer ranges of attractive interaction, which is expected to give rise to more $q_{\min}$-bound state. We use the same numeric method to study the range-four model with $V_1 = V_2 = V_3 < 0$, $V_4 > 0$ at 1/5 filling to find a quaternion phase.

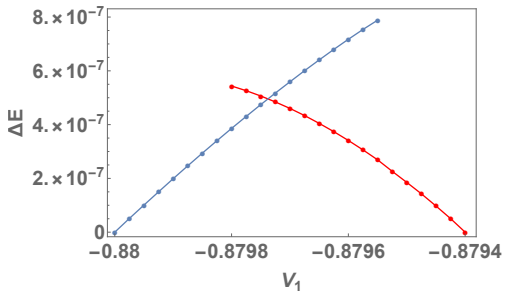

Figure 34: DMRG ground state energy (after subtracting a linear function, see text) along a cut at the interface of single (right) and trion (left) phases. The bond dimension is $\chi = 300$. These two sets of data points correspond to the energy of two phases on either of the transition. There is a region where the two curves have overlap in the parameter (V_1) space. In this region, the data point with lower energy is the ground state, while the data point with higher energy indicates a metastable states. This metastability is an artifact of DMRG which occurs near a first-order transition.

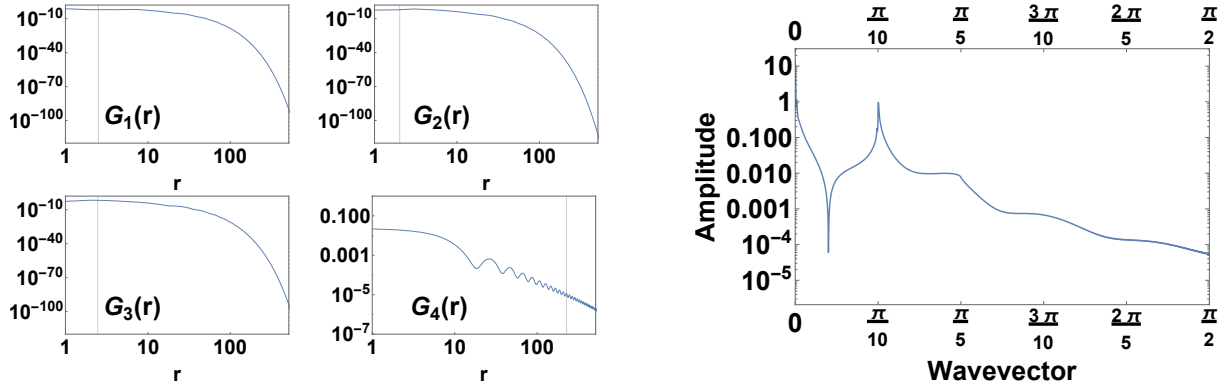

Figure 35: DMRG data in the quaternion phase: (left) Correlators in quaternion phase. The parameters of Hamiltonian are $V_1 = V_2 = V_3 = -0.7$, $V_4 = 1.7$. The DMRG bound dimension $\chi = 600$. The data indicates that $G_1(r)$, $G_2(r)$ and $G_3(r)$ decay exponentially while $G_4(r)$ decays algebraically. (right) Fourier spectra of quaternion correlator (G_4 of Fig. **??**) in a quaternion phase. The oscillatory wavevectors (k_{osc}) are located at even multiples of $\pi/20$. With a choice "derivative" $n = 2$, the first three k_{osc} can be seen in this plot as peaks or step.

To show the minimal charge (q_{min}) for gapless charged sector is 4, we plot the correlators $G_{1,2,3,4}$ of a state in the quaternion phases in Fig. 35, where G_4 is the quaternion correlator:

$$G_4(r) = \left\langle (c_i c_{i+1} c_{i+2} c_{i+3})^\dagger \, c_{i+r} c_{i+r+1} c_{i+r+2} c_{i+r+3} \right\rangle . \tag{5.22}$$

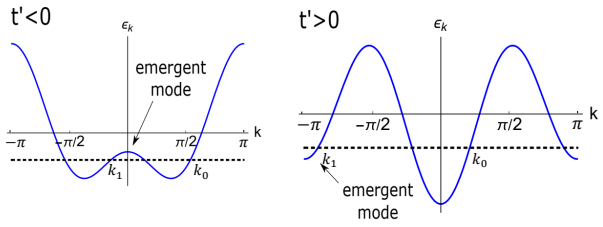

Figure 36: Band bending pictures from Ref.[1] where k_0 and k_1 are the right moving wavevectors. To satisfy Luttinger's theorem we need $k_0 + k_1 = k_{\rm F}$ (left) and $k_0 + k_1 + \pi = k_{\rm F}$ (right).

In Fig. 35, we also show the Fourier spectrum of G_4 with the choice of derivative $n = 2$ (see the last section). As the filling is 1/5, the quaternion density is 1/20. As quaternions are bosons, the spectrum shows peaks or steps at the even multiples (0, 2, 4) of $\pi/20$.

5.9 Why our numerical data is inconsistent with the band bending theory of Ref.[1]

In the effective theory of Ref.[1] two distinct Fermi-vectors appear due to the bending of the band (as shown in Fig. 36). The two Fermi-vectors k_0 and k_1 should satisfy Luttinger's theorem: $k_0 + k_1 = k_F$ or $k_0 + k_1 + \pi = k_F$. In our numerical calculations we focus on filling fraction of 1/5 and $k_F = \pi/5$. However, our numerical data shows that in the 2M phase one of the Fermi-vectors moves from $k_1 = 0$ to $k_1 = k_F/3$ while the other Fermi-vector stays constant at $k_0 = \pi/5$. The band bending picture would suggest that both Fermi points move together, either $k_0 + k_1 = \pi/5$ or $k_0 + k_1 + \pi = \pi/5$. Hence, our numerical results are inconsistent with the predictions of the effective theory of Ref.[1]. It should be noted that Ref.[1] deals with a different microscopic model, which may have a different effective field

theory.

5.10 summary

In summary we find conclusive evidence for an emergent mode in one dimensional attractive fermion chain. This emergent mode results in the formation of a stable 2M phase with two Fermi surfaces. We argue that the multi-fermion bound state liquids are not descendants of the single-mode TLL phase but are rather descendants of this 2M phase. The 2M parent theory may be interpreted as a mixture of single and pair particles[48]. Curiously, we can also rewrite the theory in terms of a mixture of pairs/trions, or trions/quarternions, etc.; however, we fail to find interpretations in terms of mixtures such as singles/trions.

The two ingredients required to realizing the proposed phenomenology is (1) confining the fermions to one-dimension and (2) controlling the form of the interaction potential between the fermions. In the setting of solid states systems the two ingredients could be realized in nanowires made of superconducting semiconductors[59–64].

In ultracold atoms confinement could be provided by either optical lattices[5;8;65] or atom chips[7] and tunable long-range interaction by the use of dipolar interactions[66;67] or Rydberg state-mediated interactions[68].

The 1D systems studied here can also be used to construct higher dimensional topological phases via the coupled-wire construction[11;48;69;70]. TLL enriched by emergent mode(s) may give a pathway to a wide range of new phases in condensed matter.

6.0 LANDAU LEVELS IN STRAINED OPTICAL LATTICES [PAPER]

In this section we present a published paper about previous project which is not related to the bound states of fermions in one dimension. This is the first project of my PhD research and we provide it here as a appendix to my thesis. I separate the different parts of the paper into different sections.

6.1 Introduction

We propose a hexagonal optical lattice system with spatial variations in the hopping matrix elements. Just like in the valley Hall effect in strained Graphene, for atoms near the Dirac points the variations in the hopping matrix elements can be described by a pseudo-magnetic field and result in the formation of Landau levels. We show that the pseudo-magnetic field leads to measurable experimental signatures in momentum resolved Bragg spectroscopy, Bloch oscillations, cyclotron motion, and quantization of in-situ densities. Our proposal can be realized by a slight modification of existing experiments. In contrast to previous methods, pseudo-magnetic fields are realized in a completely static system avoiding common heating effects and therefore opening the door to studying interaction effects in Landau levels with cold atoms.

6.2 Synthetic field in cold atoms

The Lorentz force, which acts on charged particles moving in a magnetic field, results in a number of fundamental phenomena in condensed matter systems including the Hall effect

in metals, Abrikosov lattices in superconductors, and the integer and fractional quantum Hall effects in ultra-pure two-dimensional electron gases. While phenomena, such as the quantized conductance plateaus of the integer and fractional quantum Hall effects have been both observed experimentally and described theoretically[71], many properties, such as the non-abelian nature of excitations in the fractional quantum Hall effects[72–74], remain subjects of active research.

These problems are difficult – they involve strongly interacting systems that are resistant to conventional theoretical and numerical tools. The current theoretical state of the art involves comparisons of trial wave functions and numerical calculations on small systems using exact diagonalization and DMRG[73;74]. Ultra cold atom experiments offer an alternative route, in which, potentially, the interplay of gauge fields, band structure, interactions, and disorder can be studied by engineering and controlling these effects independently[75]. Moreover, by engineering these properties one could generate novel phases that have not yet been observed in condensed matter systems[76;77].

Various groups have recently experimentally demonstrated 'synthetic gauge fields' – methods for driving neutral atoms using laser beams in such a way that they behave as if they were charged particles moving in a magnetic field[78–82]. A number of effects, such as Abrikosov lattice formation[83], Hall deflection[81;84;85], and chiral currents[86], have been observed. However, an important limitation of these methods, that use either periodic lattice modulations or Raman transitions, seems to be significant heating of the atom clouds. For optical lattice experiments, this limits the timescale in which experiments can be performed to several tens of milliseconds (later section in this chapter), in contrast to experiments in static lattices which allow for several hundreds of milliseconds[2]. Further, experiments so far have been performed with noninteracting or weakly interacting atoms. An extension of synthetic gauge fields experiments to the strongly interacting regime would require low heating rates in combination with low initial temperatures.

In this Letter, we propose an alternative method for generating synthetic magnetic fields in ultracold atom systems that relies on a completely static optical lattice, and leads to the formation of relativistic Landau levels. Inspired by pseudo-magnetic fields observed in strained graphene[87;88], molecular graphene[89], and photonic systems[90], we propose a method

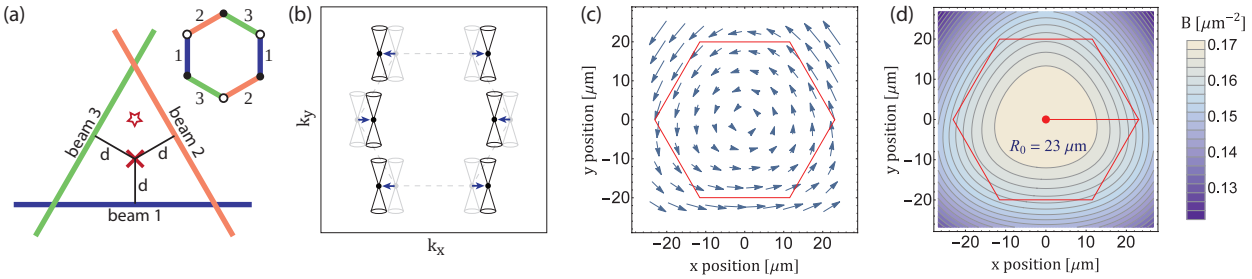

Figure 37: (a) Schematic of the setup: the optical lattice is produced by three Gaussian laser beams intersecting at 120° with offset d – lattice orientation is depicted in the upper right. The cross marks the center of the harmonic trap, and the star marks the position associated with the displaced Dirac cones depicted in (b). (b) Schematic of the displacement of the Dirac cones in momentum space associated with stretching type 1 bond. First Brillouin zone is indicated with the dashed line. (c) Pseudo-vector potential $\vec{A}$ as a function of position. (d) Pseudo-magnetic field $\vec{B} = \nabla \times \vec{A}$ as a function of position. The hexagon in (c) and (d) marks the sample area with 80% uniformity in the pseudo-magnetic field.

for generating spatially varying hopping matrix elements in a hexagonal optical lattice. Starting from a standard configuration of three Gaussian laser beams intersecting at 120°, our method relies on simply displacing the beams [Fig. 37a]. We show that pronounced Landau levels are generated close to the original Dirac points corresponding to almost homogeneous magnetic fields in real space with opposite sign at the nonequivalent Dirac points. This leads to a host of observable phenomena, such as the valley Hall effect, quantization of in-situ densities, Landau-Zener effects in Bloch oscillations, and the emergence of gap structure in Bragg spectroscopy. Since our method relies on fully static optical lattices, it forms an attractive starting point for investigating interaction effects in Landau levels[76;77;91–96] with ultracold atoms.

6.2.1 Pseudo magnetic fields in optical lattices

Consider an optical lattice that is created by the intersection of three blue-detuned laser beams at 120° angles[97;98]. The resulting honeycomb potential has the form where $\vec{k}_m$ is the wave vector of the m-th laser beam and $I_m(\vec{r})$ is it's position dependent intensity that

$$V(\vec{r}) = \left| \sum_{m=1}^{3} \sqrt{I_m(\vec{r})} e^{-i\vec{k}_m \cdot \vec{r}} \right|^2 \tag{6.1}$$

accounts for the Gaussian nature of the beams. We consider the case that the lattice is sufficiently deep so that the tight binding model is applicable. If all three beams have identical intensities the resulting band structure (in the lowest band) is identical to that of graphene with two degeneracy points in the first Brillouin zone described by the Dirac equation. Changing the intensity of one of the beams corresponds to applying a uniform strain to graphene[99], which can be captured by modifying the hopping matrix elements in the tight binding model and results in the shift of the Dirac cones in the Brillouin zone [see Fig. 37b]. This shift can be encoded in terms of the Dirac equation by adding a vector gauge field $\vec{A}$: where v_f is the group velocity near the Dirac point, and σ^μ are the Pauli matrices.

$$H_{\text{Dirac}} = \hbar v_f \left(-i\partial_\mu + A_\mu\right) \sigma^\mu, \tag{6.2}$$

Allowing for the intensities of all three beams to vary in space, we can obtain a non-uniform $\vec{A}(\vec{r})$.

The tight binding model with non-uniform hopping matrix elements on the honeycomb lattice is [1] where t_{ij} are the hopping matrix elements, $V_i = \frac{1}{2} m_{\text{at}} \omega_{\text{eff}}^2 r_i^2$ is the on-site potential that is a combination of the trap potential and the anti-trapping effect of the blue lattice $\omega_{\text{eff}}^2 = \omega_{\text{trap}}^2 - \omega_{\text{anti-trap}}^2$ with m_{at} the atomic mass, and $a_i^\dagger$ and a_i are the creation and annihilation operators. There are three types of hopping matrix elements t_{ij} associated with the three hopping directions in a honeycomb lattice. We label these as $t_{ij} = t_u(\vec{r})$, where $\vec{r} = (\vec{r}_i + \vec{r}_j)/2$ and u is the index of the laser beam that is perpendicular to the vector $\vec{r}_i - \vec{r}_j$

[1] Since we are interested in the case $I_m \gtrsim 2E_R$ we only need to consider nearest neighbor hopping ($t_{\text{nnn}} = 0.02 t_{\text{nn}}$ at $2E_R$).

$$H = -\sum_{\langle i,j \rangle} t_{ij} a_i^\dagger a_j + \sum_i V_i a_i^\dagger a_i, \tag{6.3}$$

(see Fig. 37a). Using this notation, and making the approximation that $t_1(\vec{r}) \simeq t_2(\vec{r}) \simeq t_3(\vec{r})$ and all are slowly varying functions of $\vec{r}$, we find Here, λ is the wavelength of the laser,

$$\begin{pmatrix} A_x(\vec{r}) \\ A_y(\vec{r}) \end{pmatrix} = \pm \frac{\sqrt{3}}{2\lambda t_0(\vec{r})} \begin{pmatrix} 2t_3(\vec{r}) - t_1(\vec{r}) - t_2(\vec{r}) \\ \sqrt{3}(t_2(\vec{r}) - t_1(\vec{r})) \end{pmatrix}. \tag{6.4}$$

$t_0(\vec{r}) = (t_1(\vec{r}) + t_2(\vec{r}) + t_3(\vec{r}))/3$, and $\pm$ corresponds to the gauge field at the two distinct Dirac points. We note that this form of the vector gauge is identical to that obtained in strained graphene, but the origin of the variation in the hopping matrix elements is different – here it is induced by spatial variation of the lattice depth as opposed to strain in graphene[100;101].

We connect the tight binding parameters $t_u(\vec{r})$ and $V(\vec{r})$ to the laser light intensity $I_u(\vec{r})$ at point $\vec{r}$ using a simple analytical model that accurately captures a precise numerical calculation[102]. Our model assumes that the connection is completely local [valid when $I_u(\vec{r})$ varies slowly in space on the length-scale of a unit cell] and that the laser beam intensities are close to isotropic [$I_1(\vec{r}) \simeq I_2(\vec{r}) \simeq I_3(\vec{r})$] – precisely the assumptions required for the validity of the pseudo-magnetic field description.

6.2.2 A prescription for a uniform pseudo-magnetic field

To introduce spatial variations of beam intensities, we propose to use three Gaussian beams with the same intensity and beam waist and to align them such that the beam axis form

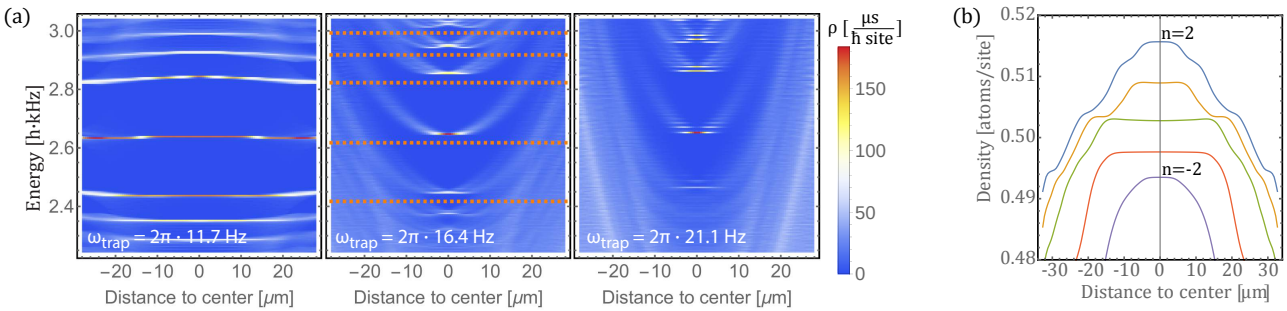

Figure 38: (a) Local Density of States as a function of energy and position in the trap for various trap frequencies. $\omega_{\text{trap}} = 11.7\,(2\pi\,\text{Hz})$ – trap cancels the anti-trapping potential of lattice beams. $\omega_{\text{trap}} = 16.4\,(2\pi\,\text{Hz})$ – bending of distinct Landau. $\omega_{\text{trap}} = 21.1\,(2\pi\,\text{Hz})$ – strong smearing of Landau levels. (b) Density of a fermionic fluid as a function of position in the trap showing incompressible plateaus [corresponding chemical potentials are indicated with dashed lines in (a)].

an equilateral triangle Fig. 37a. This choice results in a symmetric gauge field depicted in Fig. 37c, and a nearly uniform pseudo-magnetic field depicted in Fig. 37d. We note that this prescription does not introduce an offset between A and B sub-lattices. We can tune the strength and uniformity of the pseudo-magnetic field by varying the beam waist size w_0 and the displacement parameter d [Fig. 37a]. In order to probe uniform phases of matter, such as the quantized Hall effects, one typically requires a uniform magnetic field over the sample area. We have tabulated the optimal choice of w_0 and d for a range of sample sizes R_0 that ensure a uniform pseudo-magnetic field.

The maximum pseudo-magnetic field is limited because the description in terms of the Dirac equation with $\vec{A}$ breaks down when the displacement of the Dirac cones becomes comparable to the the size of the Brillouin zone $|\vec{A}| \sim 1/\lambda$. For the symmetric gauge choice $|\vec{A}|$ varies linearly across the sample, and hence the maximal pseudo-magnetic field is inversely proportional to the sample size. From Table II of the supplement we find $B_{\text{max}} = \nabla \times \vec{A} \approx 2.7/\lambda R_0$.

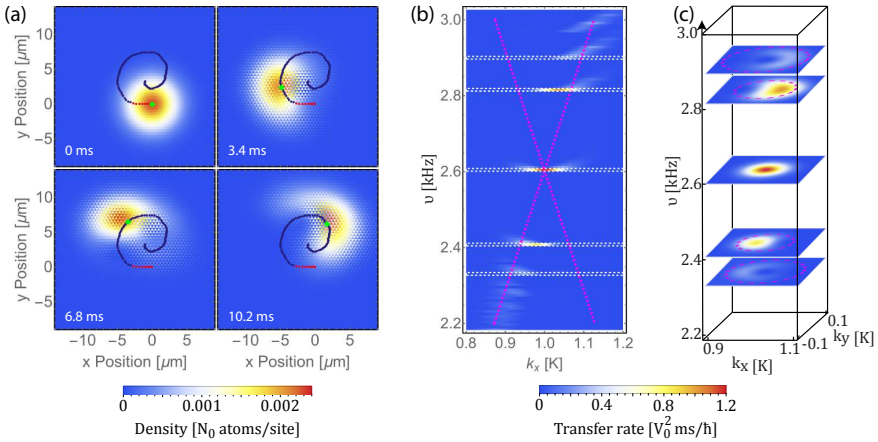

Figure 39: (a) Snap shots of the in-situ density of an atom cloud undergoing cyclotron motion, where N_0 is the total number of atoms in the cloud. Trajectory of the center of mass of the cloud is superimposed on top (red dots – tilt $\alpha/h = 0.84\text{kHz}/\mu\text{m}$, blue – no tilt, green – current frame). (b)-(c) Momentum resolved Bragg-spectroscopy: transition rate as a function of frequency $\nu = \omega/2\pi$ and momenta k_x and k_y. (b) Slice at fixed k_y=0. (c) Slices at fixed ω (as indicated by the dashed white lines in (b)). The location of the Dirac cone is indicated with dashed magenta line in (b) and (c).

6.2.3 Proposed experimental setup

To make a concrete connection to experiment, we focus on a particular realization similar to the one in Ref.[98], which we will use throughout the remainder of the letter. We consider ^{87}Rb atoms in an optical lattice with $\lambda = 700\text{nm}$, and hence a recoil energy of $E_R = 2\pi^2\hbar^2/(m\lambda^2) \approx h \times 4.685\text{kHz}$. We choose the laser beam intensity such that the potential is $4E_R$ (per beam, in the beam center) which ensures that the lattice is sufficiently deep to make the tight binding model applicable but sufficiently shallow that the hopping timescales are acceptably fast [$t_{ij}/h \approx 868\text{Hz}$]. Finally, we focus on the case $R_0 = 23\mu\text{m}$, which corresponds to a hexagonal sample with $15,000$ sites. For this setup, the maximum uniform pseudo-magnetic field of $B = 0.17\mu m^{-2}$ [Fig. 37d] is obtained by setting $w_0 = 150\mu m$ and $d = 45\mu m$.

6.2.4 Landau levels in a harmonic trap

The effective trapping frequency ω_{eff} must be large enough to ensure that the atoms are confined, but not so large as to smear out the discrete Landau levels. Without a trapping potential, we expect to see 'relativistic' Landau levels at energies $E_n = \text{sign}(n)\hbar v_F\sqrt{2|n|B}$, where $v_F = \lambda t_{ij}/(\sqrt{3}\hbar)$ and n is an integer[103;104]. The corresponding Landau level wave functions have a length scale set by the cyclotron radius $r_c = \sqrt{(2n+1)/B}$. The length scale for the ground state of the trapped lattice system is $\lambda_{\text{SHO}} = [2t_{ij}\lambda^2/(9m_{\text{Rb}}\omega_{\text{eff}}^2)]^{1/4}$, hence the ground state wave function will be confined if $\lambda_{\text{SHO}} \lesssim R_0$, which sets a lower bound on ω_{trap}. On the other hand, a Landau level will avoid being smeared out if the shift of the trap potential on the scale of r_c is small compared to the spacing to the next Landau level $\frac{1}{2}m_{\text{Rb}}\omega_{\text{eff}}^2 r_c^2 \lesssim E_{|n|+1} - E_{|n|}$, which sets an upper bound on ω_{eff}. Putting these considerations together, we find a window for observing Landau Levels where in the last expression we have

$$\frac{2\lambda^2 t_{ij}}{9m_{\text{Rb}}R_0^4} \lesssim \omega_{\text{eff}}^2 \lesssim \frac{7.2t_{ij}}{m_{\text{Rb}}R_0^{3/2}\lambda^{1/2}}\left(\frac{\sqrt{|n+1|}-\sqrt{|n|}}{2|n|+1}\right),$$

used the relation between R_0 and B. For our realization $0.2\text{Hz} \lesssim \omega_{\text{eff}}/2\pi \lesssim \{91\text{Hz}, 12\text{Hz}\}$ for $n = 0, \pm 1$.

To visualize the Landau Levels in a trapped system we plot $\rho(E, r)$, the local density of states (LDOS), as a function of position and energy [Fig. 38a]. In the absence of a trap, we expect to see sharp peaks in the LDOS as a function of energy that are independent of position. For $|\nabla V(r)| \ll |E_n - E_{n-1}|/r_c$, the LDOS is simply shifted $\rho(E, r) \approx \rho(E - V(r), 0)$ while for large $|\nabla V(r)|$, this picture breaks down and the peaks in $\rho(E, r)$ become smeared.

6.2.5 Experimental signatures

One of the defining characteristics of the quantum Hall effect is the formation of incompressible plateaus associated with the Landau levels. We propose that these plateaus can

be observed with ultra cold fermionic atoms by measuring the atom density as a function of distance away from the center of the trap [Fig. 38b]. In principle, it should be possible to observe multiple plateaus in a "wedding cake" structure. Due to the limitations on experimentally accessible optical lattice sizes we expect to see only one or two plateaus.

Another important limitation of the present generation of experiments with fermions in optical lattices is that the lowest temperatures that one can achieve $T \sim 0.5t_{ij}$ [105;106] are similar to the spacing of the Landau levels that we predict for the smallest samples. An attractive alternative is to use bosonic atoms that can be Bose-Einstein condensed (BEC) in the lattice.

To detect the pseudo-magnetic field we propose observing cyclotron motion of a cloud of condensed atoms. Starting with the cloud in the ground state in the center of the trap, we remove the trap (set $\omega_{\text{eff}} = 0$) and accelerate the cloud towards one of the Dirac points by applying a tilt $H_{\text{tilt}} = -\alpha\, \hat{q} \cdot \vec{r}$ ($\hat{q}$ is a unit vector indicating tilt direction, and α is the tilt 'force'). When the momenta of the atoms approaches the Dirac point, we remove the tilt and observe the evolution of the cloud in situ. As the atom cloud is moving with a momentum close to the Dirac momentum, it is well described by the Dirac equation, and hence its trajectory is curved by the pseudo-magnetic field [Fig. 39a]. The effective Lorentz force changes sign if the cloud is accelerated towards a non-equivalent Dirac point.

In order to directly observe the Landau levels, we propose to use Bragg spectroscopy. In this setup, a BEC that is originally prepared in the ground state ψ_0 is transferred to excited states ψ_i using a Bragg spectroscopy setup [107] described by the perturbation potential $V(r,t) = V_1 \cos(\vec{k} \cdot \vec{r}) \cos(\omega t)$. In Fig. 39(b), (c) we plot the transition rate for a range of $\vec{k}$ and ω. As a function of ω, we see clear maxima that correspond to the various Landau levels. Moreover, we can extract the momentum structure of the Landau level wave functions by varying $\vec{k}$ (i.e. performing momentum resolved Bragg spectroscopy). Without the complexity of a Bragg spectroscopy setup, Bloch-Zener spectroscopy [108] offers an alternative that can detect the separation between the $n = 0$ and $n = \pm 1$ Landau levels.

6.2.6 Observing interaction effects

Pseudo-Landau levels are particularly susceptible to the effects of interactions as the kinetic energy of the atoms within a single pseudo-Landau level is quenched. Previous theoretical investigations showed that the interplay of short and long range interactions in strained hexagonal lattices can drive the formation of a number of exotic phases[76;77;91–96]. Specifically, at 1/2-filling of the zeroth Landau level, long range interactions prefer the formation of the quantum anomalous Hall effect (that spontaneously breaks time reversal symmetry)[91;92;94–96] while short range interactions prefer the formation of charge-density-wave phases[93;96]. Detailed numerical analysis of the 1/2 filling case with on-site interactions alone suggests the formation of an exotic mixture of ferro- and anti-ferromagnetism[77]. At 2/3 filling of the zeroth Landau level, tuning the ratio of long and short range interactions is predicted to drive the formation of a triplet superfluid, a fractional topological insulator and the 2/3 fractional quantum Hall effect[76]. In comparison to natural graphene, our proposal gives the advantages of (1) better control over the strain patterns and (2) control over both short[75] and long-rang interactions (using methods based on Rydberg atoms[109], dipolar atoms[110], or dipolar molecules[111]) and (3) control over filling factors and (4) the availability of low disorder potentials, making it particularly promising for realizing these exotic phases.

6.2.7 Outlook

We have proposed a scheme for generating a pseudo-magnetic field in ultra cold atom systems that relies on spatial variations of the hopping matrix in analogy to the case of strained graphene. The typical timescales for conventional synthetic gauge field experiments in optical lattices is several tens of milliseconds mostly limited by drive induced heating. Our approach could extend this to several hundreds of milliseconds as typical in static lattices[2], thus improving timescales for investigating the interplay of pseudo-magnetic fields and interactions. Generally, our work could establish a new, very explicit link between solid state physics and ultracold quantum gases connecting ongoing experimental work in strained graphene and novel, strained optical lattices.

6.2.8 acknowledgments

It is our pleasure to thank Chandra Varma for his suggestion to consider 'strained graphene' optical lattices. We also thank Ulrich Schneider, Tracy Li, and Immanuel Bloch for useful discussions, especially in regards to experimental realizations. D. P. acknowledges support from the Pittsburgh Quantum Institute, M. E. acknowledges support from the Harvard Quantum Optics Center and the Caltech Institute for Quantum Information and Matter.

6.3 supplement

This supplement is organized as follows: (1) we summarize timescales reported in conventional synthetic gauge field experiments on a lattice; (2) we summarize the intensity profile that we used for Gaussian beams; (3) we present the details of our tight binding model and its relation to the light intensity in the lattice beams; (4) we tabulate optimal beam parameters for a range of sample sizes; (5) we show explicit details for the constraints on trap frequency presented in the main manuscript; (6) we define the local density of states; (7) we write out the transition rate for Bragg spectroscopy and (8) we present additional data on Bloch-Zener spectroscopy.

6.3.1 Timescales in experiments with optical lattices and synthetic gauge fields

To compare conventional synthetic gauge field in lattice experiments to the proposed setup we would like to compare the heating rates in the two cases. Unfortunately (with the exception of Ref.[81]) heating rates are not typically reported. Hence, we use the longest reported experimental timescale as a proxy for how long the atoms remain cold within the lattice (see Table. 2). We expect our proposed setup to extend the timescales to several hundreds of milliseconds, which is the typical timescale for experiments in static lattices[2].

Experiment	Method	Timescale [ms]
Aidelsburger et al.[79]	Raman	13
Atala et al.[86]	Raman	2
Aidelsburger et al.[112]	Raman	50
Jotzu et al.[81]	Shaking	10
Struck et al.[113]	Shaking	50
Kennedy et al.[114]	Raman	71

Table 2: Timescales in conventional synthetic gauge field experiments on a lattice, typical timescale for static optical lattice experiments are several hundreds of milliseconds[2].

6.3.2 Gaussian beams

In modeling the Gaussian lattice beams we use the following intensity profile: where $z_R =$

$$I_{\text{gaussian}}(r,z) = I_0 \left(1 + z^2/z_R^2\right)^{-1} e^{-\frac{2r^2}{w_0^2\left(1+z^2/z_R^2\right)}} \tag{6.5}$$

$\pi w_0^2/\lambda$, w_0 is the beam waist, $r = |(\vec{r} - \vec{r}_0) \times \vec{v}_0|$ is the radial distance from the beam axis, $z = |(\vec{r} - \vec{r}_0) \cdot \vec{v}_0|$ is the axial distance to the beam focal point $\vec{r}_0$, and $\vec{v}_0$ is a unit vector along the beam axis.

6.3.3 Model relating laser intensity to the tight binding parameters

To relate the intensities of the three lattice beams $I_1(\vec{r})$, $I_2(\vec{r})$, and $I_3(\vec{r})$ to the tight binding parameters $t_1(\vec{r})$, $t_2(\vec{r})$, $t_3(\vec{r})$, and $V(\vec{r})$ at a given point in space $\vec{r}$, we make two assumptions: (1) the beam intensities vary slowly in space on the length-scale of a unit cell and (2) the beam intensities are close to uniform $I_1(\vec{r}) \simeq I_2(\vec{r}) \simeq I_3(\vec{r})$.

For the case of the hopping matrix elements $t_u(\vec{r})$, the assumptions allow us to use the

a_0	1.13	b_0	2.21	b_1	-4.64	b_2	5.01	c_2	-0.17
d_1	0.002	e_1	3.13	f_1	-1.18	g_1	0.71	h_1	-0.17

Table 3: Fitting parameters for Eq. (6.6) and (6.7).

model

$$t_u = a_0 I_{\text{avg}}^{3/4} e^{-\sqrt{I_{\text{avg}}(b_0 + b_1\delta_u + b_2\delta_u^2 + c_2 \sum_{v\neq u}\delta_v^2)}}, \tag{6.6}$$

where we have dropped the index $\vec{r}$ for clarity, $I_{\text{avg}} = \frac{1}{3}\sum_{u=1}^{3} I_u$, $\delta_u = (I_u/I_{\text{avg}} - 1)$, and $\{a_0, b_0, b_1, b_2, c_2\}$ are the fitting parameters. To obtain values for $\{a_0, b_0, b_1, b_2, c_2\}$, we numerically computed t_u's for a series of spatially uniform but anisotropic lattices and then fitted the resulting data set [see Table 3]. The numerical computations were performed using the Wannier function method[102] with a sufficiently large basis to ensure convergence. As for the data set, we used various values of I_u's ranging from $2.2E_R$ to $3.6E_R$ and keeping $|\delta_u| < 0.3$ – which is the appropriate range of light intensities for the proposed setup with displaced $4E_R$ beams. We find good agreement between our model and the numerically computed hopping matrix elements as long as the beams have approximately the same intensity $|\delta_u| < 0.3$. In Fig. 40 we show this comparison along a particular slice through the data set, in which we set $I_2 = I_3 = 3E_R$ while varying I_1. The maximal logarithmic error over our dataset was $\left|\log \frac{t_{u,\text{numerical}}}{t_{u,\text{fitted}}}\right| = 0.016$.

Using the two assumptions on $I_1(\vec{r})$, $I_2(\vec{r})$, and $I_3(\vec{r})$, we can model the onsite potential due to the optical lattice using the expression

$$V = d_1 I_{\text{avg}} + e_1\sqrt{I_{\text{avg}}} + f_1 + \frac{g_1}{\sqrt{I_{\text{avg}}}} + h_1 I_{\text{avg}} \sum_v \delta_v^2, \tag{6.7}$$

where $\{d_1, e_1, f_1, g_1, h_1\}$ are the fitting parameters. Fitting the same data set as the one we used for the hopping matrix elements, results in values for the fitting parameters listed in Table 3. The maximal error over the dataset was $|V_{\text{numerical}} - V_{\text{fitted}}|/V_{\text{numerical}} = 0.004$.

6.3.4 Optimal beam parameters

In order to achieve a uniform pseudo-magnetic field over the sample area we can tune two parameters – Gaussian beam waist ω_0 and beam axis displacement d. We tabulate these

parameters for a range of sample sizes in Table 4]. The parameters were chosen to ensure that the pseudo-magnetic field varies by less than 20% over the sample area. The corresponding gap between $n = 0$ and $n = 1$ Landau levels is listed for ^{87}Rb atoms in a 700 nm, 4 E_R lattice with $t_{ij}/h \approx 870$ Hz. While the pseudo-magnetic field strength is determined by the geometry [see main text], the Landau level gap scales with the hopping strength $E_1 - E_0 = \lambda t_{ij}\sqrt{2B/3}$.

6.3.5 Constraints on trap frequency

In order to observe the Landau levels in the presence of a trap potential, we want $\omega_{\text{eff}} = \sqrt{\omega_{\text{trap}}^2 - \omega_{\text{anti-trap}}^2}$ to be large enough to confine the atoms but not so large as to smear out the Landau levels. These two constraints provide us the upper and lower bound for ω_{eff}.

For the lower bound, we begin with the lengthscale of the simple harmonic oscillator λ_{SHO}. First, we find the band mass to be:

$$m_{\text{band}} = \frac{9\hbar^2}{2t_0\lambda^2}, \tag{6.8}$$

where $t_0 = \langle t_{ij} \rangle$ represents the average value of the nearest neighbor hopping matrix element. Using the band mass, we can write down the continuum Hamiltonian for low energy states of our trapped system: Defining $\tilde{\omega} = \sqrt{\frac{m_{\text{Rb}}}{m_{\text{band}}}}\omega_{\text{eff}}$, we find that the radius of the lowest

$$\begin{aligned} H &= \frac{p^2}{2m_{\text{band}}} + \frac{1}{2}m_{\text{Rb}}\omega_{\text{eff}}^2 x^2 \\ &= \frac{p^2}{2m_{\text{band}}} + \frac{1}{2}m_{\text{band}}\left(\sqrt{\frac{m_{\text{Rb}}}{m_{\text{band}}}}\omega_{\text{eff}}\right)^2 x^2. \end{aligned} \tag{6.9}$$

energy state of the harmonic the system is approximately In order to ensure that at least the ground state is trapped, we require that $\lambda_{\text{SHO}} \leq R_0$ where R_0 is the characteristic radius of our lattice system – i.e. the radius over which the pseudo magnetic field is uniform. Thus we obtain the lower bound for ω_{eff}: For sample size $R_0 = 23.1\mu m$, $\omega_{\text{eff}} \geq 0.211 \times 2\pi$Hz.

To find the upper bound on ω_{eff}, we first evaluate the Landau level energy To avoid

$$\lambda_{\mathrm{SHO}} = \sqrt{\frac{\hbar}{m_{\mathrm{band}}\tilde{\omega}}}. \tag{6.10}$$

$$\omega_{\mathrm{eff}}^2 \gtrsim \frac{2t_0\lambda^2}{9m_{\mathrm{Rb}}R_0^4} \tag{6.11}$$

$$\begin{aligned} E_n &= \hbar v_F \sqrt{2|n|B} \\ &= \frac{\lambda t_0}{\sqrt{3}}\sqrt{2|n|B}. \end{aligned} \tag{6.12}$$

smearing the n^{th} Landau level, we want $\frac{1}{2}m_{\mathrm{Rb}}\omega_{\mathrm{eff}}^2 r_n^2 \lesssim E_{|n|+1} - E_{|n|}$, where $r_n = (2n+1)/B$ is the typical radius of n^{th} Landau level. Using the relation $B = 2.7/\lambda R_0$ obtained from Table I of the main text, we find For $R_0 = 23.1\mu m$, $\omega_{\mathrm{eff}} \lesssim 91 \times 2\pi\mathrm{Hz}$ for $n = 0$ and $\omega_{\mathrm{eff}} \lesssim 12 \times 2\pi\mathrm{Hz}$

$$\omega_{\mathrm{eff}}^2 \lesssim \frac{7.2t_{ij}}{m_{\mathrm{Rb}}R_0^{3/2}\lambda^{1/2}} \left(\frac{\sqrt{|n+1|} - \sqrt{|n|}}{2|n|+1} \right). \tag{6.13}$$

for $n = \pm 1$.

6.3.6 Local Density of States

We define the local density of states $\rho(E, r)$ as as a function of position and energy, where

$$\rho(E,r) = N \sum_{i,|E_\mu - E|<\delta} |\psi(\vec{r}_i, E_\mu)|^2 e^{-|\vec{r}_i - r|^2/(2r_0^2)}, \tag{6.14}$$

$\{E_j\}$ and $\{\psi(\vec{r}_i, E_j)\}$ are the single-particle eigenvalues and eigenfunctions of Eq. 3 in the main text, $N^{-1} = \delta \sum_i e^{-|\vec{r}_i - r|^2/(2r_0^2)}$ is a normalization factor, and r_0 specifies the range over which we measure the local density of states.

6.3.7 Bragg spectroscopy

For Bragg spectroscopy setup[107] described by the perturbation potential $V(r,t) = V_1 \cos(\vec{k} \cdot \vec{r}) \cos(\omega t)$, the transition rate is given by Here, ψ_0 is the initial state with energy E_0 and ψ_i

$$\sum_i |\langle \psi_i(\vec{r})| \cos(\vec{k} \cdot \vec{r}) \, |\psi_0(\vec{r})\rangle|^2 \delta(E_i - E_0 - \omega). \tag{6.15}$$

is the excited states with energy E_i.

6.3.8 Bloch-Zener spectroscopy

Bloch-Zener spectroscopy[108] offers an alternative to Bragg spectroscopy that can detect the separation between the $n = 0$ and $n = \pm 1$ Landau levels without the complexity of the Bragg setup. We begin with a BEC in the ground state of the trap and then apply a tilt in the direction of one of the Dirac cones in order to induce Bloch oscillations [2]. The character of the Bloch oscillations strongly depends on the lattice tilt α [see Fig. 41]. The change in character is controlled by the Landau-Zener process across the largest gap in the system –

[2] In contrast to cyclotron motion experiment, we do not stop at the Dirac point but pass through it.

the separation between $n = 0$ and $n = 1$ Landau levels – allowing us to measure this gap. If $(E_1 - E_0)/\alpha\lambda \gg 0.5\,[\ll 0.5]$ the atoms remain on the lower branch [jump to the upper branch]. The change in character can be observed directly in the in-situ motion of the atom cloud via a change of the direction of the group velocity: If the tilt angle is small, atoms will be reflected back by the gap. On the other hand, if the tilt angle is large the atoms will jump across the gap to the upper band. The presence/absence of reflection can be detected by monitoring the motion of the center of mass of the atoms along the direction of the tilt, as depicted in Fig. 42. We identify the critical tilt by a plateau in the motion of the center of mass (half the atoms stay at the lower band and half go to the upper band) as depicted in Fig. 42b.

To verify the ability of Bloch-Zener spectroscopy to measure the gap, we calculate the critical tilt for various values of the pseudo-magnetic field and hence gap. We plot the relation between the gap and the critical tilt in Fig. 43. We observe a linear relation between the critical tilt and the largest energy gap $E_1 - E_0$

$$\frac{E_1 - E_0}{\alpha_{\text{crit}}\lambda} \approx 0.5. \tag{6.16}$$

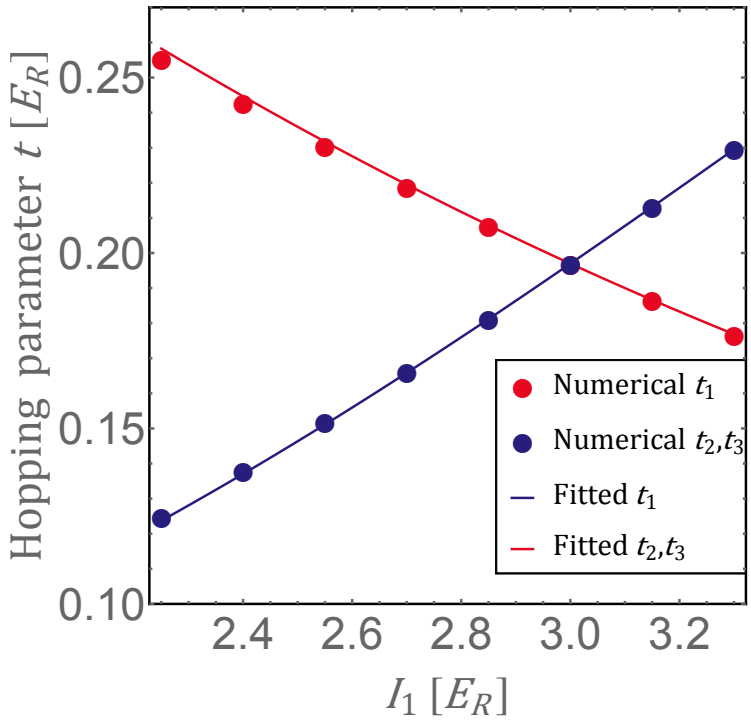

Figure 40: Comparison of (exact) hopping matrix elements obtained numerically and fitted matrix elements obtained using Eq. (6.6). For this plot, we fixed $I_2 = I_3 = 3E_R$.

R_0 $[\mu m]$	w_0 $[\mu m]$	d $[\mu m]$	B field $[\mu m^{-2}]$	LL gap $[h \cdot \text{Hz}]$
5.6	40	13	0.68	410
11	75	22.5	0.34	290
17	112	35	0.24	240
23	150	45	0.17	210
28	185	58	0.15	190
33	220	72	0.13	180

Table 4: Optimal beam waist w_0 and displacement d for different sample sizes R_0.

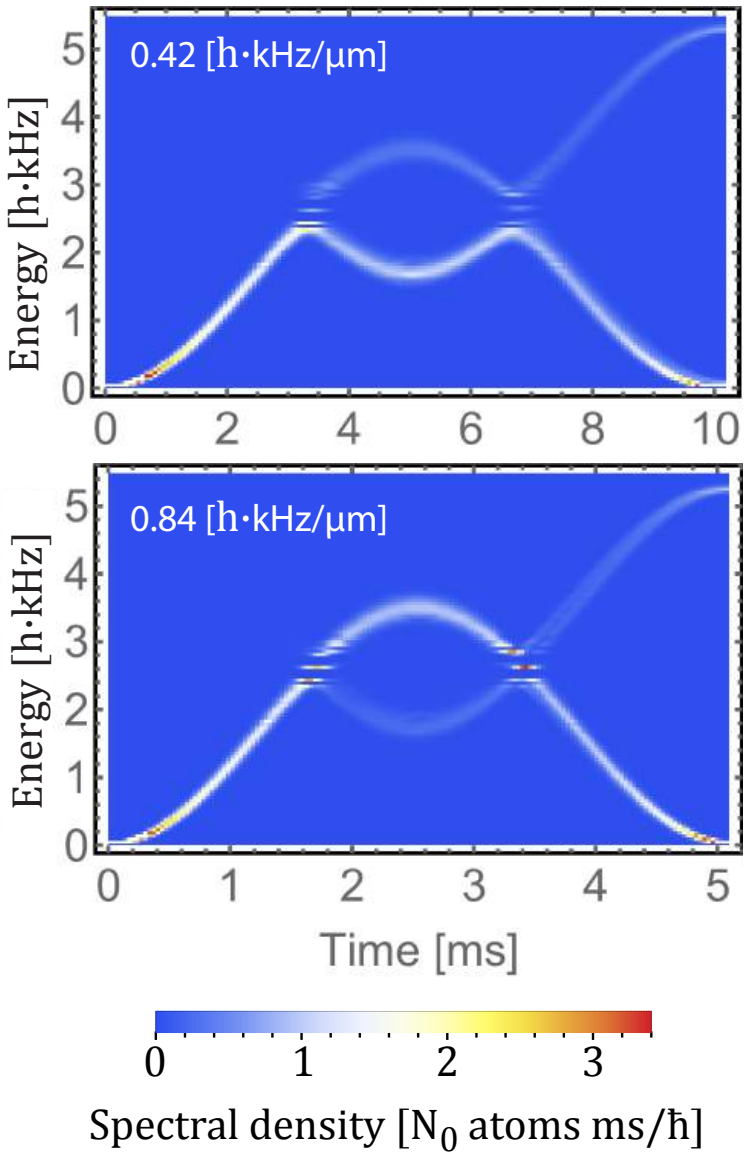

Figure 41: Bloch-Zener spectroscopy: spectral density of the atom cloud as a function of time for small tilt (top) and large tilt (bottom).

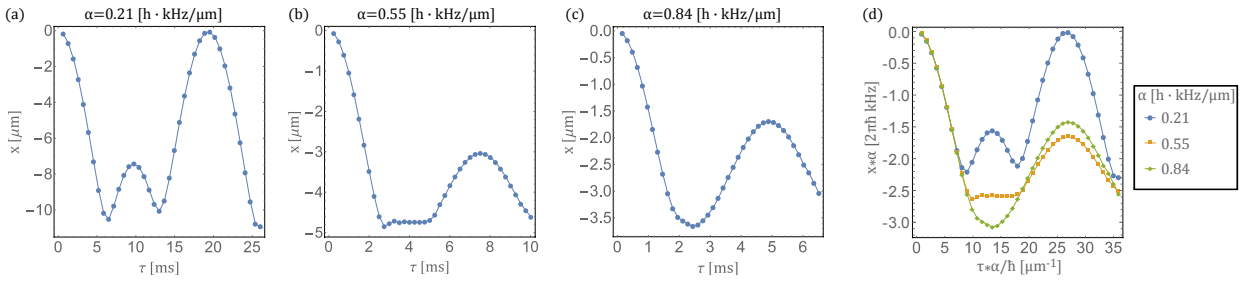

Figure 42: Tilt spectroscopy: (a-c) Center of mass position of an atom cloud as a function of time for three different values of tilt α. (d) Same data as (a-c) with both axis rescaled by α.

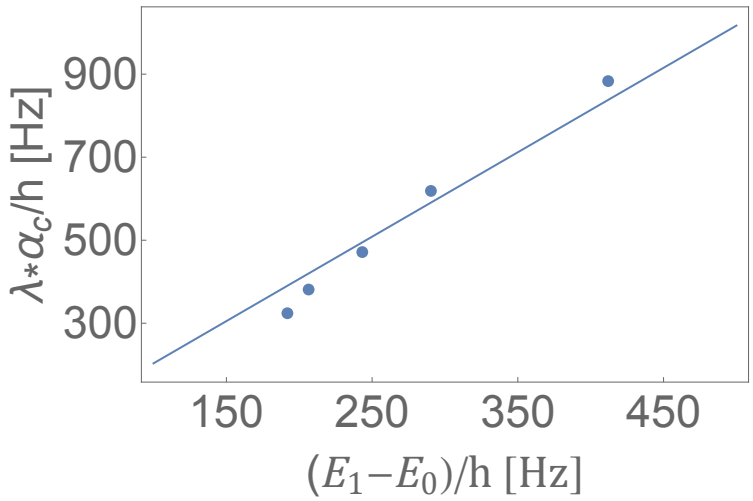

Figure 43: Relation between the critical tilt α_c (rescaled by the wavelength of optical lattice light λ) and the gap between the $n = 0$ and $n = 1$ Landau levels for various values of the pseudo-magnetic field. The line represents best fit to the linear law $E_1 - E_0 = c\,\lambda\,\alpha_c$ where c is the constant of proportionality.

BIBLIOGRAPHY

[1] J. Ruhman and E. Altman, "Topological degeneracy and pairing in a one-dimensional gas of spinless fermions," *Phys. Rev. B*, vol. 96, p. 085133, Aug 2017.

[2] I. Bloch, J. Dalibard, and W. Zwerger, "Many-body physics with ultracold gases," *Rev. Mod. Phys.*, vol. 80, no. 3, p. 885, 2008.

[3] M. Bockrath, D. H. Cobden, J. Lu, A. G. Rinzler, R. E. Smalley, L. Balents, and P. L. McEuen, "Luttinger-liquid behaviour in carbon nanotubes," *Nature*, vol. 397, no. 6720, p. 598, 1999.

[4] V. V. Deshpande, M. Bockrath, L. I. Glazman, and A. Yacoby, "Electron liquids and solids in one dimension," *Nature*, vol. 464, no. 7286, p. 209, 2010.

[5] T. Kinoshita, T. Wenger, and D. S. Weiss, "Observation of a one-dimensional tonks-girardeau gas," *Science*, vol. 305, no. 5687, pp. 1125–1128, 2004.

[6] S. Capponi, G. Roux, P. Lecheminant, P. Azaria, E. Boulat, and S. White, "Molecular superfluid phase in systems of one-dimensional multicomponent fermionic cold atoms," *Physical Review A*, vol. 77, no. 1, p. 013624, 2008.

[7] M. Gring, M. Kuhnert, T. Langen, T. Kitagawa, B. Rauer, M. Schreitl, I. Mazets, D. A. Smith, E. Demler, and J. Schmiedmayer, "Relaxation and prethermalization in an isolated quantum system," *Science*, vol. 337, no. 6100, pp. 1318–1322, 2012.

[8] T. L. Yang, P. Grišins, Y. T. Chang, Z. H. Zhao, C. Y. Shih, T. Giamarchi, and R. G. Hulet, "Measurement of the dynamical structure factor of a 1d interacting fermi gas," *Phys. Rev. Lett.*, vol. 121, p. 103001, Sep 2018.

[9] G. Salomon, J. Koepsell, J. Vijayan, T. Hilker, J. Nespolo, L. Pollet, I. Bloch, and C. Gross, "Direct observation of incommensurate magnetism in hubbard chains," *Nature*, vol. 565, 03 2018.

[10] X.-G. Wen, "Topological orders and edge excitations in fractional quantum hall states," *Advances in Physics*, vol. 44, no. 5, pp. 405–473, 1995.

[11] C. L. Kane, R. Mukhopadhyay, and T. C. Lubensky, "Fractional quantum hall effect in an array of quantum wires," *Phys. Rev. Lett.*, vol. 88, p. 036401, Jan 2002.

[12] M. Cazalilla, A. Ho, and T. Giamarchi, "Interacting bose gases in quasi-one-dimensional optical lattices," *New Journal of Physics*, vol. 8, no. 8, p. 158, 2006.

[13] D. F. Mross, J. Alicea, and O. I. Motrunich, "Explicit derivation of duality between a free dirac cone and quantum electrodynamics in $(2 + 1)$ dimensions," *Phys. Rev. Lett.*, vol. 117, p. 016802, Jun 2016.

[14] A. Imambekov and L. I. Glazman, "Universal theory of nonlinear luttinger liquids," *Science*, vol. 323, no. 5911, pp. 228–231, 2009.

[15] A. Imambekov, T. L. Schmidt, and L. I. Glazman, "One-dimensional quantum liquids: Beyond the luttinger liquid paradigm," *Reviews of Modern Physics*, vol. 84, no. 3, p. 1253, 2012.

[16] M. Mattioli, M. Dalmonte, W. Lechner, and G. Pupillo, "Cluster luttinger liquids of rydberg-dressed atoms in optical lattices," *Physical review letters*, vol. 111, no. 16, p. 165302, 2013.

[17] M. Dalmonte, W. Lechner, Z. Cai, M. Mattioli, A. Läuchli, and G. Pupillo, "Cluster luttinger liquids and emergent supersymmetric conformal critical points in the one-dimensional soft-shoulder hubbard model," *Physical Review B*, vol. 92, no. 4, p. 045106, 2015.

[18] S. Rossotti, M. Teruzzi, D. Pini, D. E. Galli, and G. Bertaina, "Quantum critical behavior of one-dimensional soft bosons in the continuum," *Phys. Rev. Lett.*, vol. 119, p. 215301, Nov 2017.

[19] T. Scaffidi, D. E. Parker, and R. Vasseur, "Gapless symmetry-protected topological order," *Phys. Rev. X*, vol. 7, p. 041048, Nov 2017.

[20] H.-C. Jiang, Z.-X. Li, A. Seidel, and D.-H. Lee, "Symmetry protected topological luttinger liquids and the phase transition between them," *Science Bulletin*, vol. 63, no. 12, pp. 753 – 758, 2018.

[21] A. Luther and V. J. Emery, "Backward scattering in the one-dimensional electron gas," *Phys. Rev. Lett.*, vol. 33, pp. 589–592, Sep 1974.

[22] T. Giamarchi and H. Schulz, "Theory of spin-anisotropic electron-electron interactions in quasi-one-dimensional metals," *Journal de Physique*, vol. 49, no. 5, pp. 819–835, 1988.

[23] I. Affleck, "Critical behaviour of su (n) quantum chains and topological non-linear σ-models," *Nuclear Physics B*, vol. 305, no. 4, pp. 582–596, 1988.

[24] K. Penc and F. Mila, "Phase diagram of the one-dimensional extended hubbard model with attractive and/or repulsive interactions at quarter filling," *Physical Review B*, vol. 49, no. 14, p. 9670, 1994.

[25] P. Lecheminant, E. Boulat, and P. Azaria, "Confinement and superfluidity in one-dimensional degenerate fermionic cold atoms," *Phys. Rev. Lett.*, vol. 95, p. 240402, Dec 2005.

[26] E. Burovski, G. Orso, and T. Jolicoeur, "Multiparticle composites in density-imbalanced quantum fluids," *Phys. Rev. Lett.*, vol. 103, p. 215301, Nov 2009.

[27] G. Orso, E. Burovski, and T. Jolicoeur, "Luttinger liquid of trimers in fermi gases with unequal masses," *Phys. Rev. Lett.*, vol. 104, p. 065301, Feb 2010.

[28] G. Roux, E. Burovski, and T. Jolicoeur, "Multimer formation in one-dimensional two-component gases and trimer phase in the asymmetric attractive hubbard model," *Physical Review A*, vol. 83, no. 5, p. 053618, 2011.

[29] B. Tian, M. Endres, and D. Pekker, "Landau levels in strained optical lattices," *Physical review letters*, vol. 115, no. 23, p. 236803, 2015.

[30] Y. He, B. Tian, D. Pekker, and R. S. Mong, "Emergent mode and bound states in single-component one-dimensional lattice fermionic systems," *arXiv preprint arXiv:1811.06066*, 2018.

[31] D. P. R. S. M. Binbin Tian, Yuchi he, "Phases and transport in spin- and mass-imbalanced fermi mixtures in one dimension." unpublished.

[32] B. T. e. a. Megan Briggeman, Michelle Tomczyk, "Pascal-liquid phases in ballistic one-dimensional laalo3/srtio3 channels.." under review at Science.

[33] U. Schollwöck, "The density-matrix renormalization group in the age of matrix product states," *Annals of Physics*, vol. 326, no. 1, pp. 96–192, 2011.

[34] S. R. White, "Density matrix formulation for quantum renormalization groups," *Phys. Rev. Lett.*, vol. 69, pp. 2863–2866, Nov 1992.

[35] I. Affleck, T. Kennedy, E. H. Lieb, and H. Tasaki, "Rigorous results on valence-bond ground states in antiferromagnets," in *Condensed Matter Physics and Exactly Soluble Models*, pp. 249–252, Springer, 2004.

[36] S. Östlund and S. Rommer, "Thermodynamic limit of density matrix renormalization," *Physical review letters*, vol. 75, no. 19, p. 3537, 1995.

[37] J. Dukelsky, M. A. Martín-Delgado, T. Nishino, and G. Sierra, "Equivalence of the variational matrix product method and the density matrix renormalization group applied to spin chains," *EPL (Europhysics Letters)*, vol. 43, no. 4, p. 457, 1998.

[38] J. Eisert, M. Cramer, and M. B. Plenio, "Colloquium: Area laws for the entanglement entropy," *Reviews of Modern Physics*, vol. 82, no. 1, p. 277, 2010.

[39] F. Pollmann, S. Mukerjee, A. M. Turner, and J. E. Moore, "Theory of finite-entanglement scaling at one-dimensional quantum critical points," *Physical review letters*, vol. 102, no. 25, p. 255701, 2009.

[40] T. Giamarchi, *Quantum physics in one dimension*, vol. 121. Clarendon press, 2003.

[41] S.-i. Tomonaga, "Remarks on bloch's method of sound waves applied to many-fermion problems," in *Bosonization*, pp. 63–88, World Scientific, 1994.

[42] J. Luttinger, "An exactly soluble model of a many-fermion system," in *Luttinger Model: The First 50 Years and Some New Directions*, pp. 3–11, World Scientific, 2014.

[43] D. C. Mattis and E. H. Lieb, "Exact solution of a many-fermion system and its associated boson field," in *Bosonization*, pp. 98–106, World Scientific, 1994.

[44] Y.-Y. Pai, A. Tylan-Tyler, P. Irvin, and J. Levy, "Physics of srtio3-based heterostructures and nanostructures: a review," *Reports on Progress in Physics*, vol. 81, no. 3, p. 036503, 2018.

[45] D. L. Maslov and M. Stone, "Landauer conductance of luttinger liquids with leads," *Physical Review B*, vol. 52, no. 8, p. R5539, 1995.

[46] V. Ponomarenko, "Frequency dependences in transport through a tomonaga-luttinger liquid wire," *Physical Review B*, vol. 54, no. 15, p. 10328, 1996.

[47] T. Roscilde, C. D. E. Boschi, and M. Dalmonte, "Pairing, crystallization and string correlations of mass-imbalanced atomic mixtures in one-dimensional optical lattices," *EPL (Europhysics Letters)*, vol. 97, no. 2, p. 23002, 2012.

[48] C. L. Kane, A. Stern, and B. I. Halperin, "Pairing in luttinger liquids and quantum hall states," *Phys. Rev. X*, vol. 7, p. 031009, Jul 2017.

[49] J. A. Kjäll, M. P. Zaletel, R. S. Mong, J. H. Bardarson, and F. Pollmann, "Phase diagram of the anisotropic spin-2 xxz model: Infinite-system density matrix renormalization group study," *Physical Review B*, vol. 87, no. 23, p. 235106, 2013.

[50] M. P. Zaletel, R. S. Mong, C. Karrasch, J. E. Moore, and F. Pollmann, "Time-evolving a matrix product state with long-ranged interactions," *Physical Review B*, vol. 91, no. 16, p. 165112, 2015.

[51] I. P. McCulloch, "Infinite size density matrix renormalization group, revisited," *arXiv preprint arXiv:0804.2509*, 2008.

[52] J. A. Kjäll, M. P. Zaletel, R. S. K. Mong, J. H. Bardarson, and F. Pollmann, "Phase diagram of the anisotropic spin-2 xxz model: Infinite-system density matrix renormalization group study," *Phys. Rev. B*, vol. 87, p. 235106, Jun 2013.

[53] P. Calabrese and J. Cardy, "Entanglement entropy and quantum field theory," *Journal of Statistical Mechanics: Theory and Experiment*, vol. 2004, no. 06, p. P06002, 2004.

[54] A. O. Gogolin, A. A. Nersesyan, and A. M. Tsvelik, *Bosonization and strongly correlated systems*. Cambridge university press, 2004.

[55] F. Haldane, "Effective harmonic-fluid approach to low-energy properties of one-dimensional quantum fluids," *Physical Review Letters*, vol. 47, no. 25, p. 1840, 1981.

[56] P. Lecheminant, A. O. Gogolin, and A. A. Nersesyan, "Criticality in self-dual sine-gordon models," *Nuclear Physics B*, vol. 639, no. 3, pp. 502–523, 2002.

[57] M. Sitte, A. Rosch, J. Meyer, K. Matveev, and M. Garst, "Emergent lorentz symmetry with vanishing velocity in a critical two-subband quantum wire," *Physical review letters*, vol. 102, no. 17, p. 176404, 2009.

[58] O. Alberton, J. Ruhman, E. Berg, and E. Altman, "Fate of the one-dimensional ising quantum critical point coupled to a gapless boson," *Physical Review B*, vol. 95, no. 7, p. 075132, 2017.

[59] V. Mourik, K. Zuo, S. M. Frolov, S. Plissard, E. P. Bakkers, and L. P. Kouwenhoven, "Signatures of majorana fermions in hybrid superconductor-semiconductor nanowire devices," *Science*, vol. 336, no. 6084, pp. 1003–1007, 2012.

[60] J. Chen and P. Yu, "J. chen, p. yu, j. stenger, m. hocevar, d. car, sr plissard, epam bakkers, td stanescu, and sm frolov, sci. adv. 3, e1701476 (2017).," *Sci. Adv.*, vol. 3, p. e1701476, 2017.

[61] M. Deng, S. Vaitiekėnas, E. B. Hansen, J. Danon, M. Leijnse, K. Flensberg, J. Nygård, P. Krogstrup, and C. M. Marcus, "Majorana bound state in a coupled quantum-dot hybrid-nanowire system," *Science*, vol. 354, no. 6319, pp. 1557–1562, 2016.

[62] A. Annadi, G. Cheng, H. Lee, J.-W. Lee, S. Lu, A. Tylan-Tyler, M. Briggeman, M. Tomczyk, M. Huang, D. Pekker, C.-B. Eom, P. Irvin, and J. Levy, "Quantized ballistic transport of electrons and electron pairs in laalo3/srtio3 nanowires," *Nano Letters*, vol. 18, no. 7, pp. 4473–4481, 2018.

[63] G. Cheng, M. Tomczyk, S. Lu, J. P. Veazey, M. Huang, P. Irvin, S. Ryu, H. Lee, C.-B. Eom, C. S. Hellberg, *et al.*, "Electron pairing without superconductivity," *Nature*, vol. 521, no. 7551, p. 196, 2015.

[64] G. Cheng, M. Tomczyk, A. B. Tacla, H. Lee, S. Lu, J. P. Veazey, M. Huang, P. Irvin, S. Ryu, C.-B. Eom, *et al.*, "Tunable electron-electron interactions in laalo 3/srtio 3 nanostructures," *Physical Review X*, vol. 6, no. 4, p. 041042, 2016.

[65] I. Bloch, "I. bloch, j. dalibard, and w. zwerger, rev. mod. phys. 80, 885 (2008).," *Rev. Mod. Phys.*, vol. 80, p. 885, 2008.

[66] M. A. Baranov, M. Dalmonte, G. Pupillo, and P. Zoller, "Condensed matter theory of dipolar quantum gases," *Chemical Reviews*, vol. 112, no. 9, pp. 5012–5061, 2012.

[67] C. Gross and I. Bloch, "Quantum simulations with ultracold atoms in optical lattices," *Science*, vol. 357, no. 6355, pp. 995–1001, 2017.

[68] J. Zeiher, J.-y. Choi, A. Rubio-Abadal, T. Pohl, R. van Bijnen, I. Bloch, and C. Gross, "Coherent many-body spin dynamics in a long-range interacting ising chain," *Physical Review X*, vol. 7, no. 4, p. 041063, 2017.

[69] J. C. Y. Teo and C. L. Kane, "From luttinger liquid to non-abelian quantum hall states," *Phys. Rev. B*, vol. 89, p. 085101, Feb 2014.

[70] R. S. Mong, D. J. Clarke, J. Alicea, N. H. Lindner, P. Fendley, C. Nayak, Y. Oreg, A. Stern, E. Berg, K. Shtengel, *et al.*, "Universal topological quantum computation from a superconductor-abelian quantum hall heterostructure," *Physical Review X*, vol. 4, no. 1, p. 011036, 2014.

[71] B. Douçot, B. Duplantier, V. Pasquier, and V. Rivasseau, eds., *The Quantum Hall Effect: Poincaré Seminar*. Birkhäuser Verlag, Basel, 2005.

[72] G. Moore and N. Read, "Nonabelions in the fractional quantum hall effect," *Nucl. Phys. B*, vol. 360, no. 2–3, pp. 362 – 396, 1991.

[73] Z. Papić, B. A. Bernevig, and N. Regnault, "Topological entanglement in abelian and non-abelian excitation eigenstates," *Phys. Rev. Lett.*, vol. 106, p. 056801, Feb 2011.

[74] M. P. Zaletel, R. S. K. Mong, and F. Pollmann, "Topological characterization of fractional quantum hall ground states from microscopic hamiltonians," *Phys. Rev. Lett.*, vol. 110, p. 236801, Jun 2013.

[75] D. Jaksch and P. Zoller, "The cold atom hubbard toolbox," *Ann. Phys.*, vol. 315, no. 1, pp. 52 – 79, 2005.

[76] P. Ghaemi, J. Cayssol, D. N. Sheng, and A. Vishwanath, "Fractional topological phases and broken time-reversal symmetry in strained graphene," *Phys. Rev. Lett.*, vol. 108, no. 26, p. 266801, 2012.

[77] B. Roy, F. F. Assaad, and I. F. Herbut, "Zero modes and global antiferromagnetism in strained graphene," *Phys. Rev. X*, vol. 4, p. 021042, May 2014.

[78] Y.-J. Lin, R. L. Compton, K. Jimenez-Garcia, J. V. Porto, and I. B. Spielman, "Synthetic magnetic fields for ultracold neutral atoms," *Nature*, vol. 462, no. 7273, pp. 628–632, 2009.

[79] M. Aidelsburger, M. Atala, S. Nascimbène, S. Trotzky, Y.-A. Chen, and I. Bloch, "Experimental realization of strong effective magnetic fields in an optical lattice," *Phys. Rev. Lett.*, vol. 107, p. 255301, Dec 2011.

[80] H. Miyake, G. A. Siviloglou, C. J. Kennedy, W. C. Burton, and W. Ketterle, "Realizing the harper hamiltonian with laser-assisted tunneling in optical lattices," *Phys. Rev. Lett.*, vol. 111, no. 18, p. 185302, 2013.

[81] G. Jotzu, M. Messer, R. Desbuquois, M. Lebrat, T. Uehlinger, D. Greif, and T. Esslinger, "Experimental realization of the topological haldane model with ultracold fermions," *Nature*, vol. 515, pp. 237–240, 11 2014.

[82] N. Goldman, G. Juzeliūnas, P. Öhberg, and I. B. Spielman, "Light-induced gauge fields for ultracold atoms," *Rep. Prog. Phys.*, vol. 77, no. 12, p. 126401, 2014.

[83] Y.-J. Lin, R. L. Compton, A. R. Perry, W. D. Phillips, J. V. Porto, and I. B. Spielman, "Bose-einstein condensate in a uniform light-induced vector potential," *Phys. Rev. Lett.*, vol. 102, no. 13, p. 130401, 2009.

[84] L. J. LeBlanc, K. Jiménez-García, R. A. Williams, M. C. Beeler, A. R. Perry, W. D. Phillips, and I. B. Spielman, "Observation of a superfluid hall effect," *Proc. Natl. Acad. Sci. USA*, vol. 109, no. 27, pp. 10811–10814, 2012.

[85] M. Aidelsburger, M. Lohse, C. Schweizer, M. Atala, J. T. Barreiro, S. Nascimbene, N. R. Cooper, I. Bloch, and N. Goldman, "Measuring the chern number of hofstadter bands with ultracold bosonic atoms," *Nature Phys.*, vol. 11, pp. 162–166, 12 2015.

[86] M. Atala, M. Aidelsburger, M. Lohse, J. T. Barreiro, B. Paredes, and I. Bloch, "Observation of chiral currents with ultracold atoms in bosonic ladders," *Nature Phys.*, vol. 10, pp. 588–593, 08 2014.

[87] F. Guinea, M. I. Katsnelson, and A. K. Geim, "Energy gaps and a zero-field quantum hall effect in graphene by strain engineering," *Nature Phys.*, vol. 6, pp. 30–33, 01 2010.

[88] N. Levy, S. Burke, K. Meaker, M. Panlasigui, A. Zettl, F. Guinea, A. C. Neto, and M. Crommie, "Strain-induced pseudo–magnetic fields greater than 300 tesla in graphene nanobubbles," *Science*, vol. 329, no. 5991, pp. 544–547, 2010.

[89] K. K. Gomes, W. Mar, W. Ko, F. Guinea, and H. C. Manoharan, "Designer dirac fermions and topological phases in molecular graphene," *Nature*, vol. 483, pp. 306–310, 03 2012.

[90] M. C. Rechtsman, J. M. Zeuner, A. Tunnermann, S. Nolte, M. Segev, and A. Szameit, "Strain-induced pseudomagnetic field and photonic landau levels in dielectric structures," *Nature Photon.*, vol. 7, pp. 153–158, 02 2013.

[91] I. F. Herbut, "Pseudomagnetic catalysis of the time-reversal symmetry breaking in graphene," *Phys. Rev. B*, vol. 78, p. 205433, Nov 2008.

[92] D. A. Abanin and D. A. Pesin, "Interaction-induced topological insulator states in strained graphene," *Phys. Rev. Lett.*, vol. 109, p. 066802, Aug 2012.

[93] S. Gopalakrishnan, P. Ghaemi, and S. Ryu, "Non-abelian $su(2)$ gauge fields through density wave order and strain in graphene," *Phys. Rev. B*, vol. 86, p. 081403, Aug 2012.

[94] B. Roy and I. F. Herbut, "Topological insulators in strained graphene at weak interaction," *Phys. Rev. B*, vol. 88, p. 045425, Jul 2013.

[95] B. Roy, F. F. Assaad, and I. F. Herbut, "Zero modes and global antiferromagnetism in strained graphene," *Phys. Rev. X*, vol. 4, p. 021042, May 2014.

[96] B. Roy and J. D. Sau, "Competing charge-density wave, magnetic, and topological ground states at and near dirac points in graphene in axial magnetic fields," *Phys. Rev. B*, vol. 90, p. 075427, Aug 2014.

[97] P. Soltan-Panahi, J. Struck, P. Hauke, A. Bick, W. Plenkers, G. Meineke, C. Becker, P. Windpassinger, M. Lewenstein, and K. Sengstock, "Multi-component quantum gases in spin-dependent hexagonal lattices," *Nature Phys.*, vol. 7, no. 5, pp. 434–440, 2011.

[98] L. Duca, T. Li, M. Reitter, I. Bloch, M. Schleier-Smith, and U. Schneider, "An aharonov-bohm interferometer for determining bloch band topology," *Science*, vol. 347, no. 6219, pp. 288–292, 2015.

[99] E. Alba, X. Fernandez-Gonzalvo, J. Mur-Petit, J. J. Garcia-Ripoll, and J. K. Pachos, "Simulating dirac fermions with abelian and non-abelian gauge fields in optical lattices," *Annals of Physics*, vol. 328, pp. 64–82, 2013.

[100] H. Suzuura and T. Ando, "Phonons and electron-phonon scattering in carbon nanotubes," *Phys. Rev. B*, vol. 65, p. 235412, May 2002.

[101] J. L. Mañes, "Symmetry-based approach to electron-phonon interactions in graphene," *Phys. Rev. B*, vol. 76, p. 045430, Jul 2007.

[102] R. Walters, G. Cotugno, T. H. Johnson, S. R. Clark, and D. Jaksch, "Ab initio derivation of hubbard models for cold atoms in optical lattices," *Phys. Rev. A*, vol. 87, no. 4, p. 043613, 2013.

[103] V. B. Berestetskii, E. M. Lifshitz, and L. P. Pitaevskii, *Relativistic Quantum Theory*. Pergamon, Oxford, 1971.

[104] K. S. Novoselov, A. K. Geim, S. V. Morozov, D. Jiang, M. I. Katsnelson, I. V. Grigorieva, S. V. Dubonos, and A. A. Firsov, "Two-dimensional gas of massless dirac fermions in graphene," *Nature*, vol. 438, pp. 197–200, 11 2005.

[105] D. Greif, T. Uehlinger, G. Jotzu, L. Tarruell, and T. Esslinger, "Short-range quantum magnetism of ultracold fermions in an optical lattice," *Science*, vol. 340, no. 6138, pp. 1307–1310, 2013.

[106] R. A. Hart, P. M. Duarte, T.-L. Yang, X. Liu, T. Paiva, E. Khatami, R. T. Scalettar, N. Trivedi, D. A. Huse, and R. G. Hulet, "Observation of antiferromagnetic correlations in the hubbard model with ultracold atoms," *Nature*, vol. 519, pp. 211–214, 03 2015.

[107] P. T. Ernst, S. Gotze, J. S. Krauser, K. Pyka, D.-S. Luhmann, D. Pfannkuche, and K. Sengstock, "Probing superfluids in optical lattices by momentum-resolved bragg spectroscopy," *Nature Phys.*, vol. 6, pp. 56–61, 01 2010.

[108] S. Kling, T. Salger, C. Grossert, and M. Weitz, "Atomic bloch-zener oscillations and stückelberg interferometry in optical lattices," *Phys. Rev. Lett.*, vol. 105, p. 215301, Nov 2010.

[109] T. Macri and T. Pohl, "Rydberg dressing of atoms in optical lattices," *Phys. Rev. A*, vol. 89, no. 1, p. 011402, 2014.

[110] A. De Paz, A. Sharma, A. Chotia, E. Marechal, J. Huckans, P. Pedri, L. Santos, O. Gorceix, L. Vernac, and B. Laburthe-Tolra, "Nonequilibrium quantum magnetism in a dipolar lattice gas," *Phys. Rev. Lett.*, vol. 111, no. 18, p. 185305, 2013.

[111] K. R. Hazzard, B. Gadway, M. Foss-Feig, B. Yan, S. A. Moses, J. P. Covey, N. Y. Yao, M. D. Lukin, J. Ye, D. S. Jin, and A. M. Rey, "Many-body dynamics of dipolar molecules in an optical lattice," *Phys. Rev. Lett.*, vol. 113, no. 19, p. 195302, 2014.

[112] M. Aidelsburger, M. Lohse, C. Schweizer, M. Atala, J. T. Barreiro, S. Nascimbene, N. Cooper, I. Bloch, and N. Goldman, "Measuring the chern number of hofstadter bands with ultracold bosonic atoms," *Nature Phys.*, vol. 11, no. 2, pp. 162–166, 2015.

[113] J. Struck, M. Weinberg, C. Ölschläger, P. Windpassinger, J. Simonet, K. Sengstock, R. Höppner, P. Hauke, A. Eckardt, M. Lewenstein, *et al.*, "Engineering ising-xy spin-models in a triangular lattice using tunable artificial gauge fields," *Nature Phys.*, vol. 9, no. 11, pp. 738–743, 2013.

[114] C. J. Kennedy, W. C. Burton, W. C. Chung, and W. Ketterle, "Observation of bose-einstein condensation in a strong synthetic magnetic field," *Nature Phys.*, 2015.